ISB

Invest to Save Budget

Improved Air Quality Forecasting
Invest to Save Report ISB52-11

Final report for the ISB-52 project.

by

K Bozier, CG Collier, F Davies, AR Holt, DR Middleton, GN Pearson, S Siemen, G Upton, DV Willetts & RI Young.

November 2004

University of Essex   THE UNIVERSITY OF SALFORD   Met Office   QinetiQ

Authorisation

Prepared by   Dr RI Young

        Title   Team Leader Remote Sensing

        Signature

        Date   Nov 2004

        Location   QinetiQ Malvern

Principal authors   Dr GN Pearson

        Appointment   QinetiQ Fellow, Remote Sensing

        Location   QinetiQ

Principal authors   Professor DV Willetts

        Appointment   QinetiQ Senior Fellow, Remote Sensing

                          QinetiQ

Principal authors   Dr DR Middleton

        Appointment   Air Quality Scientist

        Location   Met Ofice, Exeter

Principal authors   Dr F Davies

        Appointment   Research Fellow, ISB-52

        Location   Salford University

Principal authors   Professor A Holt

        Appointment   Propagation and Remote Sensing Research group.

        Location   Essex University

Principal authors   Dr K Bozier

        Appointment   Research Fellow, UFAM Instrumentation Specialist

        Location   Salford University

Principal authors   Professor CG Collier

        Appointment   Dean, Faculty of Science, Engineering and Environment

        Location   Salford University

Principal authors   Professor G Upton

        Appointment   Propagation and Remote Sensing Research group.

        Location   Essex University

Record of changes

Issue	Date	Detail of Changes
1.0	November 2004	First Release

EXECUTIVE SUMMARY

This report, ISB52-11, was produced under Project 52 of the Invest to Save Budget scheme. The project aim was to advance atmospheric pollution dispersion models with the goal of improving air quality forecasting. Potential users of improved air quality information include members of the public with respiratory problems, managers of health resources deployed to care for them, and people working in the planning cycle to regulate existing and proposed sources of air pollutants.

Air quality Forecasts (i.e. a few days ahead) and Projections (i.e. for local air quality management, some years into the future) are essential in informing the public about poor imminent air quality, and in managing air quality. Dispersion models are one of the key tools for this, in conjunction with emissions inventories, meteorological data and pollutant monitoring. Air quality forecasting relies upon semi-empirical parameterisations within numerical models for the description of turbulent dispersion. Air quality projections use the same models, together with information on future emission control policies. There is scope to improve air quality forecasting through improved information about turbulence measured in an urban atmosphere. For example, turbulence is sensitive to the local stability and surface drag, yet current models of turbulence have very limited descriptors of urban effects on turbulence. Urban episodes of air pollution can occur when wind speeds are light and mixing heights are shallow, but measurements of these above a big city such as London are rarely made, despite their importance for urban air quality. This project applied novel remote sensing technology to address this lack of urban measurements.

During the project life, the team developed a better understanding of airflow near the Earth's surface, focussing especially on urban meteorology. This was achieved through the gathering of three dimensional wind flow data using laser radars, also called lidars, and by incorporating that new knowledge into the dispersion models.

A lidar is similar to conventional radar but uses an invisible, eye-safe, laser beam as its source of radiation. The great advantage of lidars for monitoring wind flow is that they can make more precise measurements than conventional radars and can probe to greater heights than most tall masts. In addition, lidars can make measurements in regions of the lower atmosphere above a city, which would be inaccessible to either aircraft or tethered balloons.

The lidars work by measuring the Doppler shift of light back-scattered from fine aerosol particles (water droplets, dust, etc) suspended within the atmosphere. The line of sight velocity component of the wind is then calculated. By sampling at different angles, and combining results from the two lidars, a picture of the three dimensional airflow in a scanned region can be assembled. Typically the scanned volume will be a few cubic km with the probes separated by up to 10 km.

Two 10μm pulsed Doppler lidar systems have been developed by QinetiQ, Malvern. The development of the first lidar system (the Salford University lidar) was conducted under a previous contract, but the development of an identical second lidar system (the QinetiQ lidar) was conducted under the first phase of this project. The two systems have then been deployed on a summer and winter trial.

Dual Doppler lidar is a new technique developed for this project in order to exploit laser technology to obtain atmospheric measurements that a single instrument cannot make. A single lidar returns the Doppler velocity along the line of sight of the laser pulses. A dual lidar allows velocity components to be estimated by solving for the flow where the beams intersect. This is the first time that two identical lidar systems have been used to make simultaneous measurements of the wind field. This necessitates careful siting and alignment of the two lidars. In addition, the data also facilitates the estimation of a number of important parameters that are used or calculated in atmospheric dispersion models.

Computer software was developed at Essex University to visualise the flow and aid in the interpretation of the collected data.

A complementary set of dispersion model data was collected from the UK Met Office NAME model, and the ADMS model, and compared to the lidar data. Both models are much used in the United Kingdom. The NAME model is used for air quality forecasting, source apportionment, accident and emergency simulations, episode analysis, and long range transport of pollutants and volcanic ash. The ADMS model is used in statutory local air quality management by local authorities involved in air quality reviews and assessments under the Environment Act 1995. This can include mapping of current air quality, and forecasts of projected air quality for several years ahead, based upon various planning or traffic management scenarios. ADMS is also used for environmental impact assessment and applications to the Environment Agency for large developments, such as power stations and industrial sources. Other dispersion models are also used in such work, and so the full set of processed data are being published upon the British Atmospheric Data Centre web site. The data-set will be useful to developers of other dispersion models.

In this, the final ISB-52 report, the performance of the lidars is assessed through the quality of the data collected and its impact upon improving the accuracy of dispersion model predictions. A key result of the lidar observations during the experiments in summer 2003 was to reveal significant differences in observed and modelled values of the mixing height, especially noticeable across the urban-rural boundary. It was concluded that there is consequently scope and need for refinement of the existing models of urban mixing height. The observed differences helped explain why the urban pollution concentrations were underestimated using current models, though this observation was dependent upon the prevailing conditions.

The Project represented a unique opportunity to gain mixing heights, flow and turbulence data using lidar remote sensing over a city for the improvement of dispersion models that are used in air quality forecasting. Current experience in the Met Office shows that the required measurement heights and spatial sampling over a conurbation can only be achieved through these lidar remote sensing techniques.

List of contents

1. INTRODUCTION

1.1 Background to the ISB-52 project

The Environment Act of 1995 requires Local Authorities to provide local air quality forecasts. DETR Air Quality Regulations 1997 prescribe air quality objectives to be achieved by 2005 and where, in the Local Authority's judgement, they will not be achieved, a local authority must designate the relevant areas as Air Quality Management Areas (AQMA).

Human health is affected by air quality, according to one estimate the NHS currently spends nearly £500m pa on treating asthma sufferers alone and the affliction is believed to cost the nation over £400m pa in lost productivity. Improved forecasts will provide vulnerable sections of the community with advance warnings of high pollution levels, permitting preventative or palliative actions to be taken. Additionally, better models will inform local authorities on the pollution impact of road closures and the optimal siting of boundaries to restricted traffic zones.

Much of the research currently being undertaken aims to investigate the dispersion of atmospheric pollutants derived from industry and transport in urban areas. NERC has funded a major research programme known as URGENT (Urban regeneration and the environment) but this has concentrated on atmospheric **chemistry**. The Met. Office is devoting much effort to the development of operational **physical** models of atmospheric dispersion.

The eye safe Doppler lidars at Malvern and Salford offer a unique opportunity to measure turbulence in and around urban areas, and thus to validate these dispersion models. Whilst a single system can achieve much, two systems could, if carefully sited, measure three dimensional air flows, and hence pollution pathways, in a way that has not been done before. The preparation of a combined dataset offers the modellers a basis for more complex parameterisations of the way pollution moves in and around urban street canyons.

Local air quality management uses dispersion models to forecast poor air quality events. Whilst there are a number of models in use they all consider similar parameters principally the mixing height, stability, and turbulence. Measurements of these parameters over urban areas are not routinely available. This is because to ensure good exposure, synoptic stations are often located at airports. When data is collected from instruments placed upon city centre buildings careful evaluation is necessary to mitigate any local effects. Validation of urban models is thus hampered by a lack of observational data sets. Given these limitations the ISB-52 project has been investigating the application of remote sensing using scanning pulsed Doppler lidar for urban dispersion studies [1-11].

A lidar is similar to conventional radar but uses in this application an invisible, eye-safe, laser beam as the radiation source. The great advantage of lidars for monitoring wind flow is that they can make more precise measurements than conventional radars and can probe to heights greater than most tall masts. In addition, lidars can make measurements in regions of the lower atmosphere above a city, which would be inaccessible to aircraft or tethered balloons.

A lidar system measures the Doppler shift of light back-scattered from fine aerosol particles (water droplets, dust, etc) suspended within the atmosphere. The line of sight velocity component of the wind is then calculated. By sampling at different angles, and combining results from the two lidars, a picture of the three dimensional airflow in a scanned region can be assembled. Typically the scanned volume will be a few cubic km with the probes separated by up to 10 km.

Two lidar systems have been developed and built by QinetiQ, Malvern [2,3,12,13]. The development of the first (the Salford University lidar) was conducted under a previous contract, but the development of an identical second system (the QinetiQ lidar) was conducted under the first phase of this project. The two systems have then been deployed on summer and winter trials. This is the first time that two identical lidar systems have been used to make simultaneous measurements of the wind field. The use of two lidar systems has enabled the independent measurement of two components of the wind flow simultaneously on a second by second basis. A complementary set of dispersion model data has been collected and a comparison the lidar data to numerical predictions made.

This Project explored the deployment of lidar systems in an urban environment. It also investigated the requirements of the data processing software in order to meet the needs of the dispersion modelling community. Dispersion modellers and lidar operators have very different conceptual approaches to the same flow; a primary task in this project was to bring these conceptual models to a convergent view. For example modellers tend to concentrate upon data collected as point measurements. However a fast response on a sonic anemometer is very slow for lidar optics; spatial averaging along the lidar sample volume is quite different to temporal averaging applied to a sonic's time series record. This work was an essential first step in the Project. It defined the foundations for building consistency between lidar measurements and dispersion model met pre-processing. Software was then developed to process the lidar signals for use with the dispersion modelling work.

1.2 Dispersion model variables
The aim of this Project is the improvement of air quality forecasting through the use of lidar data. To achieve this goal it was necessary to test and improve the way dispersion models describe the atmospheric stability and mixing depth. It was also necessary to test some of the equipment and ideas in single mode operation as a first step. This means considerable attention must be paid to the flow field as represented in dispersion models i.e. the descriptions of mean flow and turbulent fluctuations. The mean flow advects material away from the source; the fluctuations ensure the spreading and dilution of the pollutant.

Meteorological pre-processors in dispersion models have to represent the complexity of the dispersing atmosphere in simplified form; this Project sought to improve these descriptions where indicated by lidar field data. In improving the modelling of the underlying physics, the lidar data will thus be potentially improving any relevant dispersion model, and will not be inherently biased towards any one model. This wider usefulness of the lidar data will meet a contractual requirement.

The Project represents a unique opportunity to obtain flow and turbulence data using lidar remote sensing over a city for the improvement of dispersion models that are

used in air quality forecasting. Current experience in the Met Office shows that the required measurement heights and spatial sampling over a conurbation can only be achieved through these lidar remote sensing techniques.

1.2.1 NAME Lagrangian Model

The UK Met Office NAME model was developed as a long-range model for radio-nuclides. It has been extended to the dispersion and chemistry of sulphur and nitrogen compounds, leading to aerosol formation via heterogeneous reactions. Currently its application to model the production of ozone is under development. Another version is being upgraded to handle dispersion at small scales, such as near buildings. An important application of NAME has been its use for air quality forecasting under the National Air Quality Bulletin System. Forecasts of air quality are released to public via the media such as the BBC.

The NAME model was described by two Met Office reports, by Ryall and Maryon [14] and Maryon et al. [15]. Recently the plume rise scheme has been improved, as described in Webster and Thomson [16] and is a Lagrangian particle model. The particles are dispersed by advection and a random velocity calculated according to the numerical weather prediction velocity field and the stability-dependent turbulence statistics respectively.

The key dispersion parameters are as follows:

Wind profile $u(p,t)$, $v(p,t)$, $w(p,t)$
Potential temperature profile $\theta(p,t)$
Standard deviations of wind fluctuations $\sigma_u(p,t)$, $\sigma_v(p,t)$, $\sigma_w(p,t)$
Turbulent kinetic energy dissipation rate $\varepsilon(p,t)$
Lagrangian integral time-scale $\tau_L(p,t)$

Where each variable is a field of values at the grid-point p and time-step t.

The components u, v, and w may be defined in terms of the co-ordinate grid directions within the numerical weather prediction model, travelling east, north and vertically (earth's radius) respectively. The co-ordinates may be latitude, longitude, and a height co-ordinate. The last can be terrain following and/or combining pressure relative to mean sea level pressure or surface pressure. Thus *eta* co-ordinates may be found, as well as the more conventional metres. See the NAME documentation (above).
(NB: These co-ordinates might change with the New Dynamics Unified Model.)

Within the model it is worth noting that the turbulent quantities near to a large point source are changed by a buoyant, momentum plume, and could be the subject of another lidar study, once the techniques are proven in the field.

NAME requires a full three-dimensional field of meteorological variables, whereas plume models such as ADMS, AERMOD, ISC, AEOLIUS, BOXURB etc. require meteorological data from a single point.

1.2.2 ADMS Plume Model

The key dispersion parameters are as follows (for further details see the ADMS Model Documentation from the CERC web site, or from D J Thomson at the Met Office):

Wind profile $u(p,t)$, $v(p,t)$, $w(p,t)$

Potential temperature profile $\theta(p,t)$: when not available the model assumes an overlying stable profile into which the convective layer grows as a function of solar heating of the ground during the day. Measurement of this growth of the convection would thus be valuable.

Standard deviations of wind fluctuations $\sigma_u(p,t)$, $\sigma_v(p,t)$, $\sigma_w(p,t)$ are calculated from the diagnosed parameters including Monin Obukhov stability in the surface layer.

Turbulent kinetic energy dissipation rate $\varepsilon(p,t)$

Lagrangian integral time-scale $\tau_L(p,t)$.

Since the model can calculate a wind profile according to local stability and local surface roughness length, any measurements of differences in wind profile or turbulence profiles between smooth and rough sub-strates would be valuable.

The ADMS met pre-processor software was developed by Dr D J Thomson in the Met Office.

ADMS is described by:
Carruthers D. J., McHugh C. A., Robins A. G., Davies B. M., Thomson D. J. and Montgomery M. (1994)
The UK Atmospheric Dispersion Modelling System: Comparison with data from Kincaid, Lillestrom and Copenhagen
Proceedings of the Workshop on Harmonisation within Atmospheric Dispersion Modelling for Regulatory Purposes, Manno, Switzerland, published by the European Commission.
See also web site www.cerc.co.uk

1.2.3 AERMOD Plume Model

The key dispersion parameters are as follows:
> Wind profile $u(p,t)$, $v(p,t)$, $w(p,t)$
> Potential temperature profile $\theta(p,t)$
> Standard deviations of wind fluctuations $\sigma_u(p,t)$, $\sigma_v(p,t)$, $\sigma_w(p,t)$
> Turbulent kinetic energy dissipation rate $\varepsilon(p,t)$
> Lagrangian integral time-scale $\tau_L(p,t)$

AERMOD requires these inputs: date & time, sensible heat flux, friction velocity, convective velocity scale, temperature profile above mixing layer (potential temperature gradient), mixing heights for convection & mechanical motions, Lonin Obukhov length, surface roughness length, Bowen ratio, albedo, wind speed and direction at given height, ambient dry bulb temperature and its measured height. Upper air data are: date & time, height, direction, speed and temperature.

AERMOD is described under:
Cimorelli A. J., Perry S. G., Venkatram A., Weil J. C., Paine R. J., Wilson R. B., Lee R. F. and Peters W. D. (1998)

AERMOD: Description of model formulation
US EPA web site http://www.epa.gov/scram001/

1.2.4 US EPA Gaussian Models

The key dispersion parameters in these older models are as follows (for further details see the user manual for PCRAMMET available from the US EPA web site):

Wind profile $u(p,t)$, $v(p,t)$, $w(p,t)$ but expressed as mean velocity and direction measured at a well exposed anemometer at 10 m above level open ground (rather than as three orthogonal components over a range of heights). In the RAM model, a power law wind profile is calculated, with power selected by stability. Other variables in RAM are invariant with height.

Potential temperature profile $\theta(p,t)$ is only used within the model (using values set by stability class) for the Briggs' plume rise scheme.

Stability Class, according to Pasquill-Gifford-Turner approaches, diagnosed using latitude, time and date, sunrise/sunset, solar radiation or cloud cover, and mean 10m wind speed. Then plume standard deviations are calculated according to stability class and distance downwind. The scheme in urban areas follows the Briggs' urban dispersion parameter curves, as described by Turner (1994).

Standard deviations of wind fluctuations $\sigma_u(p,t)$, $\sigma_v(p,t)$, $\sigma_w(p,t)$ are not computed in these models, but could be used to check stability class diagnosis via derived standard deviations of elevation and azimuth angles.

Turbulent kinetic energy dissipation rate $\varepsilon(p,t)$ is not used. Lagrangian integral time-scale $\tau_L(p,t)$ is not used.

PCRAMMET

Using as inputs: date, time, lowest cloud ceiling height (hundreds of feet), wind direction (tens of degrees), wind speed (both at 10 m), dry bulb temperature (nearest °F), and cloud cover (tenths), precipitation (type & mm). Upper air data needed are local minimum mixing height (morning) and maximum (afternoon) mixing height.

Giving as outputs: date, time, wind speed (m s^{-1}), temperature (K), Pasquill Gifford stability, and mixing height (m) for rural/urban cases; friction velocity, (m s^{-1}), Monin Obukhov length, roughness length, precipitation.

US EPA models are downloadable and described on:
US EPA web site http://www.epa.gov/scram001/

1.2.5 VDI Puff Lagrangian Model

The key dispersion parameters are as follows:
Wind profile $u(p,t)$, $v(p,t)$, $w(p,t)$
Potential temperature profile $\theta(p,t)$
Standard deviations of wind fluctuations $\sigma_u(p,t)$, $\sigma_v(p,t)$, $\sigma_w(p,t)$
Turbulent kinetic energy dissipation rate $\varepsilon(p,t)$
Lagrangian integral time-scale $\tau_L(p,t)$

1.2.6 Boxurb Model

The model uses a stability scheme after F B Smith, requiring:
>Mean 10 m wind speed and direction.
>Low, medium, high, and total cloud cover (oktas).
>Sunrise/sunset, time and date.

It estimates an urban heat store, the urban sensible heat flux and diagnoses friction velocity and Monin Obukhov length. It also requires the urban mixing depth, or boundary layer, whichever is lower.

1.2.7 Aeolius Model
Model inputs are wind speed, wind direction, temperature and pressure.

The model assumes a neutral logarithmic wind profile to extrapolate 10 m well exposed wind speed and direction to the nominal roof height, and down to street level. Data to define better the wind speed profile near and amongst buildings are needed.

The model also uses a simple horizontal vortex flow within the street aligned along the street axis; this also requires study.

AEOLIUS is documented and downloadable from the Met Office web site: www.metoffice.com/environment

1.3. Urban lidar principles
Doppler lidar systems have been used to measure the characteristics of the atmospheric boundary layer over the last twenty years or so. However, a range of practical difficulties (including the cost associated with this technology) have limited its deployment for comprehensive research. While pulsed Doppler lidar systems are now available commercially, there are only a limited number of such instruments available for use in atmospheric field measurement campaigns.

The potential of Doppler lidar to measure the characteristics of boundary layer turbulence has been reported by a number of authors [17-19]. In this section we introduce the principles of urban lidar.

The data products produced from pulsed lidars and the specification of typical lidar outputs are now reviewed. Back-scatter signals are obtained from naturally occurring atmospheric aerosols whose particle size distribution (up to a few microns) is such that they faithfully follow the local flow-field. The systems produce sight-line Doppler, and back-scatter strength with a range resolution determined by the laser pulse-length. In the TEA laser upgraded system this sight-line range gate will be of order 100-200m in length. The equivalent transverse dimension is much smaller, typically less than a metre, since the system is designed to emit a diffraction-limited collimated beam from a 15cm aperture. The laser pulse repetition frequency will be some tens of Hz, possibly as high as 100Hz, and it will be necessary to integrate the signal over tens to one hundred pulses, dependent on the atmosphere. Thus observation rates are likely to be about 1Hz. It is possible in principle to measure spectral width of the signal as well as the peak velocity; this is a measure of variability of sight-line velocity within the range gate and thus of turbulence on the gate scale. Such a width requires a higher signal to noise ratio than velocity estimation so is more limited in range and will not be a data product available initially. The

maximum range capability is highly dependent on atmospheric transmission, which at this wavelength of 10 microns is strongly humidity dependent, as well as on the back-scatter strength. For the upgraded system under optimal conditions this maximum range is expected to be about 10km. There is also a minimum range of a few range gates caused by the finite detector recovery time after saturation by instrumental narcissus. Various scanning patterns can be applied to the emission as appropriate to the specific investigation.

1.4 Identification of key parameters to be measured for use in the dispersion models.

The philosophy in this project was to develop two novel lidars to allow the monitoring of wind flow with unprecedented accuracy. It was not the intention of ISB52 to develop two fully autonomous systems that can be left in-situ. Hence there was no ability developed to achieve more accurate pollution dispersal forecasts through continuous monitoring. Instead the aim of the project was to improve pollution dispersal forecasts through a new more sophisticated understanding of the dynamics of the wind field in the urban environment obtained from the lidar measurements made during the trial periods.

Air quality forecasts (i.e. a few days ahead) and Projections (i.e. for local air quality management, some years into the future) are essential tools in informing the public about poor imminent air quality, and in managing air quality. Air quality forecasting relies upon semi-empirical parameterisations within numerical models for the description of turbulent dispersion. Air quality projections use the same models, together with information on future emission control policies. There is scope to improve air quality forecasting through improved information about turbulence measured in an urban atmosphere. For example, turbulence is sensitive to the local stability and surface drag, yet current schemes for turbulence have very limited descriptors of urban effects on turbulence.

The variables identified as being of particular importance to improve air quality forecasting included:

- Mixing height (possibly multiple layers),
- Day/Night transition in stability and turbulence variables,
- Mean wind profiles & heat flux,
- Existence & properties of urban roughness sub layer (height z_*), which affects wind and turbulence profiles, and the rural-urban transition,
- Measurements in summer anticyclonic conditions are needed to study the contrast between strong daytime convection and night time conditions,
- Measurements in winter anticyclonic conditions are needed to study the effects of temperature inversions.

Of these meteorological parameters the most important to observe are the shape of the planetary boundary layer (PBL) or mixing layer, and turbulence. The key flow parameters are mean flow, and turbulence. All dispersion models need these parameters described accurately. The currently existing models are well proven for the rural environment but would benefit from further adaptation for use in the urban. In particular this implies a better description of the more complicated turbulence in the urban environment that is driven by the greater roughness scales that occur there.

The aim of the trials was to investigate how these quantities vary over the course of a day in both the rural and urban environments. In particular it was important to observe the diurnal changes in turbulence and structure and depth of the mixing layer.

Possible ways to exploit this new knowledge within the models include:

- identification of the appropriate update intervals for defining the properties of the mixing layer during the forecast calculation.
- providing a more appropriate description of the spatial variation across the mixing layer, including a more accurate description of the change in the height of the PBL at the rural urban interface.
- from an understanding of the differences in evolution of the mixing layer in the urban and rural environments, use separate models to reflect the differing temporal changes within the different environments.
- modelling of the turbulence to reflect more accurately the vertical thermal structure.

1.5 Review of the rest of the document

In section 2 the recent upgrades of the Salford and QinetiQ pulsed 10 μm lidars are discussed. It was these upgrades that allowed the lidars to make the observations necessary to meet the objectives of ISB-52. In section 3 the principles of using lidar data to derive mean flow and turbulence quantities are considered. Although a full literature review of lidar remote sensing is not attempted, this review demonstrates lidar has the ability to measure the relevant wind flow parameters with sufficient accuracy to meet the requirements of ISB-52. Section 4 details the two dual Doppler lidar trials conducted during ISB-52. Besides describing trial geometry and meteorological conditions section 4 summarises the data gathered, how scan strategies were developed depending upon ambient conditions and reviews the trial experience.

A major part of the project was to develop a software package written to analysis and display the dual lidar data in 3d using a Silicon Graphics workstation. This software was known as DAViS. (A more limited version of which was also developed to allow a similar display ability on a PC). Section 5 is describes the development and ability of DAViS.

Key results from the data analysis are presented in section 6. This section gives examples of the major analysis techniques employed on the lidar data, including how the lidar observations were matched to model parameters and undertaken a comparison of observations to predictions.

Finally in section 7 the findings of ISB-52 are summarised from which conclusions are drawn and recommendations made.

2. LIDAR DEVELOPMENT

2.1 Characteristics of the system

To derive an understanding of the atmosphere at the rural urban interface requires observations of the flow phenomena occurring there. In particular the derivation of atmospheric PBL depends upon the accurate estimation of wind velocity, momentum fluxes and distance. Pulsed Doppler lidar offers an unique ability to make these observations, however it is only recently that this lidar technology has reached a sufficient level of maturity to allow this. In ISB-52 such observations have been made using two Doppler lidar infrared (10 microns) systems operated by the University of Salford and QinetiQ (formerly DERA, Malvern). These two systems are the only two Doppler lidars of their type in the UK. The use of dual Doppler lidar facilitates for the first time the unambiguous derivation of all components of the wind flow field.

Pulsed Doppler lidar can monitor the wind by detecting back-scattered light from naturally occurring aerosol particles which act as tracers embedded in the atmosphere. The lidar measures the Doppler shift between the outgoing and return radiation and consequently determines the line-of-sight component of the wind velocity. Range resolution is ultimately determined by the pulse length but factors such as the length of the time series taken for each range-gate and the processing algorithms employed also affect the range resolution. The heterodyne receiver configuration, when operated in the shot noise limit, gives essentially quantum-limited performance in the IR where background light and detector noise would otherwise limit the sensitivity.

The pulsed lidar systems used in ISB-52 is based around the system described in reference 12 with signal processing as proposed in reference 21 although it has now been upgraded to use a Transverse Excitation Atmospheric (TEA) pressure laser. The characteristics of the original and current systems are given in Table 2.1.

Parameters	Values	
	Old	New
Transmitter	CO_2 laser	CO_2 laser
Operating wavelength	10.6 μm	10.6 μm
Energy per pulse	0.7 mJ	70 mJ
Pulse repetition frequency (PRF)	120 Hz	upto 50Hz
Wind velocity accuracy	0.5 ms^{-1}	0.7 ms^{-1}
Range resolution	112 m	112 m
Maximum Range	4.6 km	10 km
Minimum Range	400 m	700 m

Table 2.1 Summary of the Salford lidar system parameters.

2.2 Equipment description

A major part of the work being undertaken in this project is the upgrade to the existing Q-switched lidar system. The upgrade involves new transmitter technology, allowing the output power to be increased by two orders of magnitude. A somewhat similar upgrade has now been completed (using quite separate funding) on the sister

equipment which will be used to provide the second lidar system for the trials in this project. Figure 2.1 shows a schematic drawing of the optical layout and figures (2.2-2.3) show photographs of the lidar. The transmitter and local oscillator lasers are housed within a common invar frame structure to ensure a high degree of passive stability. The transmitter is a hybrid design where a high energy pulsed gain module is combined with a cw discharge section in the same resonator. We have employed a "U-fold" configuration for compactness. The local oscillator (LO) and transmitter resonators both use a Littrow-mounted diffraction grating for line selection and were set to operate on the P(2O) transition at a wavelength of 10.591μm. A dedicated computer monitors the outputs of both these lasers (via detectors D1 and D2) and controls their operation. The same computer also controls the pulse repetition rate and the triggering. This is done with custom hardware and software. The software user interface is shown in figure 2.4 and the custom hardware board is shown in figure 2.5.

The basic principle for the computer control of the lasers is as follows. A dither is applied to the Piezoelectric tube (PZT) upon which the transmitter laser output coupling mirror is mounted. This dither is 170mV in amplitude and is at a frequency of 673Hz. This results in a displacement dither on the laser mirror of approximately ± 9nm. The optical frequency dither induced by this motion is approximately ± 250kHz. Since the gain bandwidth in continuous wave mode is only ~100MHz, this frequency dither gives rise to a small amplitude dither on the laser output and this is detected by D1. The signal is then filtered and fed to a phase sensitive amplifier (PSA) referenced to the original dither voltage. The phase of the PSA output is then used in a feedback loop to hold the laser at peak power which is approximately line centre. D1 also receives radiation from the CW LO and this beats with the transmitter output. This beat frequency is amplified and then passed through an electronic discriminator which has an output centred at 12MHz and a response of -0.5 V MHz^{-1}. The output of this device is then used as the error signal in a second servo loop which holds the LO laser 12MHz away from the transmitter, thus defining the receiver IF as 12MHz.

The back-scattered radiation is detected by D3. This signal is amplified and sent to the data acquisition (DA) computer. A reference signal for each laser shot is detected by D2 and this signal is also sent to the DA computer.

The signal is then processed in real-time by this computer in contrast to the previous system where the raw data was stored for off-line processing. The range-gate length, maximum range, number of shots to average and number of accumulation sets are entered into the programme. Once a noise file has been taken the acquisition button is pressed and data set is taken. The size of the files is reduced with respect to the raw data storage mode used previously. Half an hour's worth of data out to 9km range with 8 seconds of averaging per set occupies ~ 350 kbytes.
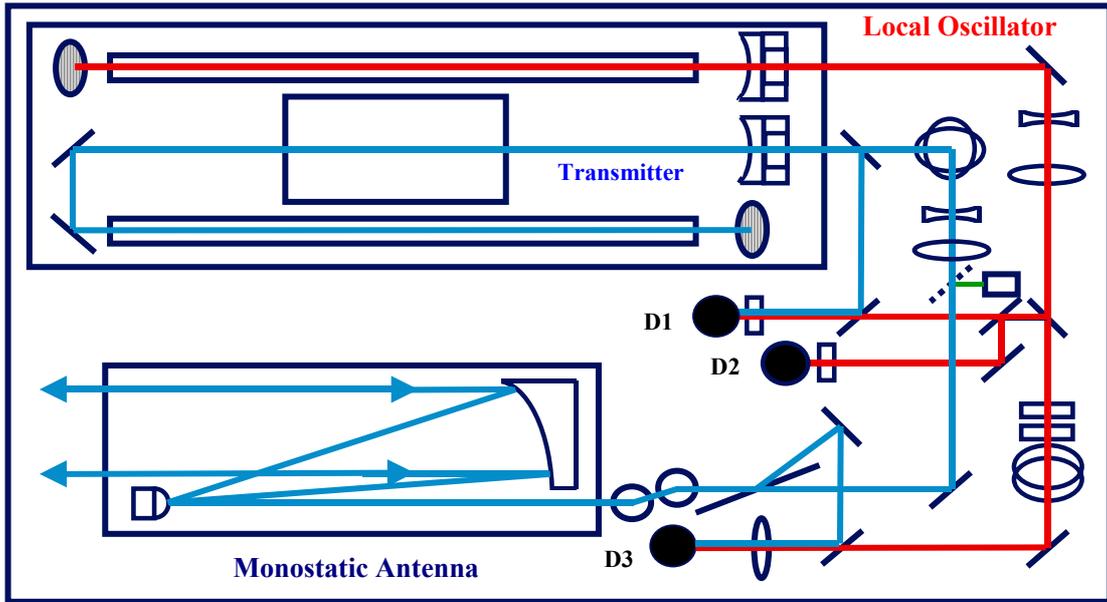
Figure 2.1 A schematic diagram of the optical layout of the lidar
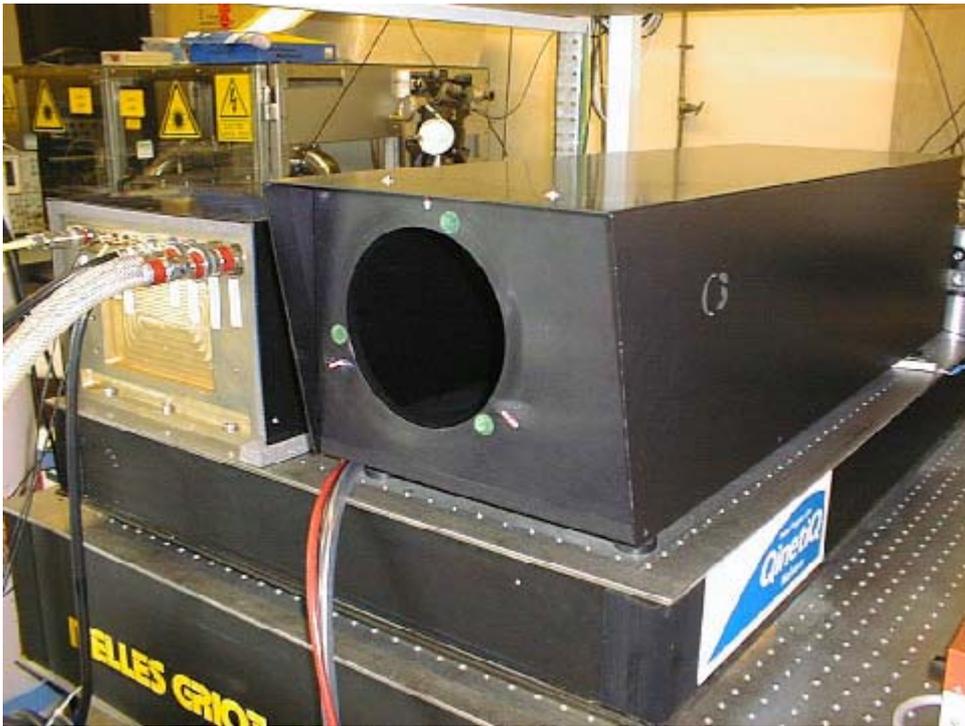
Figure 2.2 A photograph of the lidar showing the output aperture and the laser power/coolant connections**.**

Figure 2.3 A photograph of the lidar showing the laser enclosure, the optical mounts, the detectors and the telescope.
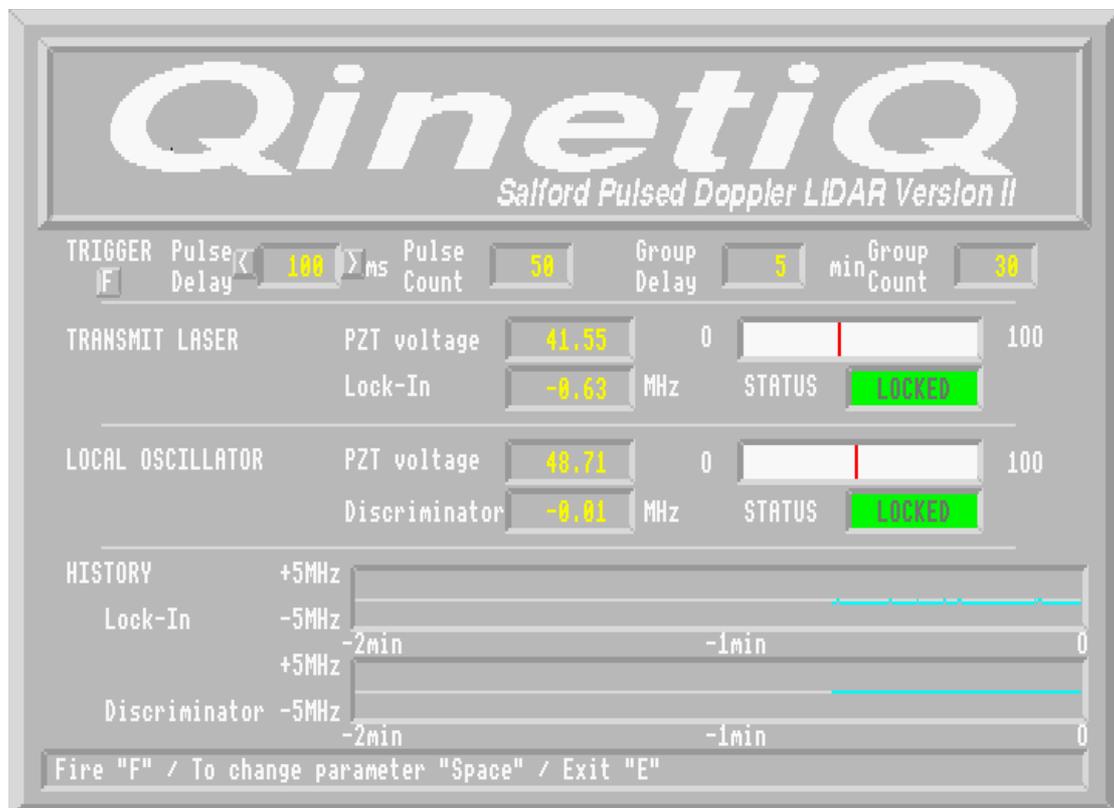
Figure 2.4 The user interface of the control software

Figure 2.5 A photograph of the custom-made control board

2.3 Lidar system performance

The derivation of turbulence variables depends upon the accurate estimation of wind velocity, momentum fluxes and distance. The lidar utilises back-scattered power returns from distributed aerosols which de-correlate the return time series on time scales of the order of micro-seconds, although the returns from successive range-gates and pulses are uncorrelated. However, due to the larger Doppler shift at these wavelengths (at a wavelength of 10 μm the Doppler shift is approximately 200 KHz ms^{-1}), the return time series from a single pulse is sufficient for the Doppler analysis. The accumulation of the returns from multiple pulses is not a prerequisite for the Doppler analysis, but is a technique for performing speckle averaging and increasing the number of signal photo electrons per estimate, thereby obtaining improved Doppler and return power measurements. In the present system 50 pulses are usually averaged every second averaging less pulses reduces the maximum range.

The minimum ranges of the systems are determined by the back reflections of the individual optical components within the lidar. The maximum ranges are dependent upon the alignment of components within the system and the aerosol loading of the atmosphere. The two lidar systems consequently show slightly different minimum and maximum ranges, due to their different alignments. These maxima and minima vary under different atmospheric conditions. The minimum and maximum ranges are approximately 700 m and 9000 m.

The range resolution is determined by the pulse length and the number of points in the digitised time series used for each range gate in the signal processing. Using a high PRF, where the returns from multiple pulses can be incoherently accumulated over time scales in which atmospheric motion can be assumed to be constant (~ 1 s), is one

way of achieving a compromise between range and Doppler resolution. Reducing the pulse length degrades the Doppler performance, which can be offset by the accumulation process. The error in line-of-sight velocity measurements using the new lidar system are estimated as in Table 2.2. For these calculations the signal was integrated over 80 pulses.

Range gate	SNR (db)	Error (m sec^{-1})
10 (1120 m)	10	0.7
40 (4480 m)	-5	1.0
60 (6720 m)	-14	1.1

Table 2.2 Errors in line-of-sight velocity estimates made using the new lidar

The QinetiQ system has a slightly better overall performance than the Salford system as it has a higher SNR within the coverage range. Both systems have scanning mirror assemblies which can scan in the horizontal at fixed elevation (PPI) and in the vertical at fixed Azimuth (RHI). However, the Salford system can only scan horizontally 0-295° and vertically 0-45° whereas the QinetiQ system can scan horizontally 0-360° and vertically 0-180°. The Salford system can, however, point vertically using a special mirror to deflect the lidar beam. The new scanning system proposed as part of this project for the Salford lidar should improve the overall system performance through improved SNR and scanning geometry making it compatible with the QinetiQ system. Both lidars are mounted in vehicles.

The system characteristics thus determine the rate at which data can be taken. In the data discussed in the following sections the old lidar system, which had a p.r.f. of 120 Hz and accumulated data over 120 pulses, recorded data at 1 Hz, while the new system, which had a p.r.f. set at 10 Hz and accumulated data over 50 pulses, recorded data at 0.2 Hz. The data record rate determines how fast the lidar beam can be scanned if good spatial resolution is required. With the new system a full azimuth scan (295°) took approximately 10 minutes while a full elevation scan (42°) took approximately 3 minutes. This performance is sufficient for the requirements of ISB-52. Examples of lidar observations are presented in section 6.

3. 3. DISPERSION MODEL PARAMETERS FOR THE BOUNDARY LAYER

3.1 Dispersion models

A dispersion model uses the state of the atmosphere to calculate the downwind travel (advection) and the turbulent dispersion (mixing) of the plumes emitted from chimneys and other emissions sources. Deposition processes and chemical reactions, in gas and aqueous phase can also be simulated.

Generally for an urban air quality forecast in the UK, the NAME model is used, though other dispersion models are used for environmental impact studies when large developments are planned. An important feature consistent to all of these models is that the plume rise and turbulent mixing has to be calculated or estimated.

Hence whilst the Project focused upon using the NAME model forecasts for comparative purposes with the lidar data, the key findings should be readily extendable to all other air quality models.

3.2 The Met Office operational dispersion modeling system

3.2.1. Unified Model

The Unified Model, or UM, is the Met Office's operational weather forecasting and climate research model [22]. The current version 5 incorporates the so-called 'New Dynamics', to distinguish it from earlier versions [23,24]. The aim in developing the model was to use more up-to-date numerical methods to avoid some of the compromises seen in other models. Since the model is used for climate research, additional constraints on the dynamics are needed to ensure conservation of species over long climate runs. The model can be run in several configurations according to application while using a common code. The global model has a grid 432×325 (0.8333°longitude, 0.5555°latitude) and the mesoscale model (initialised from global runs) has a grid 146×182 (0.11°longitude, 0.11°latitude); in mid-latitudes the grids have ~60 km and ~11 km resolution respectively. The model has height based co-ordinates, with terrain following near the ground, constant levels above and with 38 levels in the vertical direction. It is non-hydrostatic so that vertical accelerations are treated explicitly within the dynamics. A number of improvements have been made to the physical processes in the model, such as radiation, microphysics, convection and cloud. The surface tiling scheme 'MOSES' was developed (*Best et al., 2000*) to incorporate 'tiles' of different surface properties (sea, forest, urban etc.).

3.2.2 NAME Model

The numerical model data generated by the Met Offices UM are archived in a form that can be used in the atmospheric dispersion model called NAME. It follows then that improvements in the modelling of urban affects in the UM, should improve the NAME model accordingly. NAME was developed as a long range Lagrangian particle model. Validation trials of the long range version were reported by Ryall and Maryon [14]. In NAME large numbers of imaginary particles are released from emission sources and are advected by the mean flow. Plume rise is solved using, effluent temperature and velocity, along with profiles of wind and temperature from the UM [16]. Random walk techniques represent the level of turbulence in the atmosphere thereby causing the particles to gradually diverge or disperse. Particles carry pollutant mass, which gradually changes as loss processes or chemical reactions occur. Secondary pollutant (e.g. sulphate, nitrate aerosols) formation is modelled. NAME is

used for many applications, including nuclear accidents, pollutant episode studies, source attributions, and air quality forecasting. It is the basis for the UK's national air quality forecasts.

3.3 Matching lidar data to dispersion Model Parameters
An important goal of this project was to measure urban values of dispersion parameters with the aim of improving forecasts of urban air quality. The new data are being exploited within name in the following ways:

- Provide more accurate description of the spatial variations in the mixing layer above changing surface types e.g. change in the height of the PBL and other parameters at the rural-urban interface,
- Improve parameterization schemes for the mixing layer in the urban and rural environments, responding to the differing temporal changes within these environments,
- Model the turbulence and heat flux to more accurately reflect the vertical thermal structure.

Table 3.1 lists the variables used in turbulent dispersion and plume rise schemes of the Met Office NAME model with an emphasis here upon the parameters that are measurable by Doppler lidar. In table 3.1 the Unified Model, which is the Met Office operational weather forecasting model, is denoted by UM NWP. Since NAME is a Lagrangian model in table 3.1 variables from more traditional types of environmental impact 'plume models, such as ADMS (UK) or AERMOD (USA) are also identigfied. These models replace earlier Gaussian formulations with non-Gaussian descriptions of dispersion in the convective boundary layer. Modern understanding considers the asymmetrical effects upon dispersion; of faster updrafts and slower downdrafts. They also replace stability classifications by a more quantitative measure, the Monin Obukhov Length [1].

Dispersion parameters describe the turbulent conditions in the atmosphere and are used to calculate the rate of advection and turbulent spread. Table 3.1 presents the parameters (with references) that, after much discussion of lidar characteristics, appeared most amenable to measurement in the field by this technique. Summarising:

- *Mixing height* from visual inspection of RHI scans, or analysis of profiles of SNR, back-scatter signal intensity, or curve-fit to back-scatter coefficient
- Profiles of *mean wind speed and direction* from sine curve fit to VAD data.
- Turbulence *velocity variances* from multiple RHI scans or dual lidar sampling.
- *Friction velocity* via Reynolds' stresses using fluctuating velocity components.
- *Eddy dissipation rate* from spectral slope, and *Lagrangian integral time-scale* and *length-scale* from spectrum.
- *Sensible heat flux* and *convective velocity scale* obtained indirectly.

The most important of the variables listed in table 3.1 for observing and understanding dispersion mechanisms are profiles of wind and turbulence and the height of the planetary boundary layer (PBL), or mixed layer. Of particular importance is a better description of the possible enhanced turbulence in the urban PBL that is driven by the greater roughness scales of the surface. Also the affects of the increased heat flux attributable to urban thermal properties as well as

anthropogenic heat production. Hence it is important to observe the diurnal changes in turbulence and the structure and depth of the mixing layer. Differences in urban and rural atmospheres have been documented by Oke [25] and are under detailed review by the European action COST 715 [26] which studies urban meteorology and air pollution problems.

Variable	Symbol	NAME Perspective	Lidar Perspective
Boundary Layer Depth	h	Rural h value via UM NWP profiles. City has internal layer(s).	Strength of back-scatter signal identifies aerosol layer(s). (Mok and Rudowicz, 2004)
Mean flow velocity (space or time average)	$\bar{u}, \bar{v}, \bar{w}$	NAME uses 3-D fields (UM NWP) of $\bar{u}, \bar{v}, \bar{w}$ updated each time-step.	VAD data yields mean $\bar{u}$ and $\bar{v}$. $\bar{w}$ from vertical beam.
Turbulence	$\sigma_u, \sigma_v, \sigma_w$	NAME uses standard deviations of wind velocity component fluctuations $\sigma_u, \sigma_v, \sigma_w$.	Dual lidar data can provide fluctuations u', v', w' to obtain $\sigma_u, \sigma_v, \sigma_w$.
Local friction velocity derived from local Reynolds stress	u_* $\overline{u'w'}, \overline{v'w'}$	NAME calculates u_* or uses UM NWP output for $\sigma_u, \sigma_v, \sigma_w$.	Dual lidar processing can yield Reynolds stress $\overline{u'w'}, \overline{v'w'}$ and friction velocity u_*
Log law for surface layer mean wind speed in neutral conditions	$\bar{u} = \dfrac{u_*}{k}\ln\left(\dfrac{z-d}{z_0}\right)$ Notation: Use d or z_d	NAME follows UM NWP log law. NAME has surface momentum roughness length $z_0(x,y)$ from database.	Dual lidar data for $\overline{u(z)}$ to verify profiles and check u_*, k, z_0, d .
Urban roughness sub-scale height	z_* z_* is height to which roughness affects turbulence statistics or	Name may be extended to use z_* if urban roughness sub-layer confirmed.	Dual lidar data for Reynolds stress and friction velocity may shed light on the existence an urban roughness sub-layer
Eddy dissipation rate	ε	NAME calculates ε for turbulence and plume rise schemes.	Lidar fluctuations processed to generate spectrum and estimate ε
Lagrangian integral timescale and Integral length scale	$\tau_L = \displaystyle\int_0^\infty R(\tau)d\tau$ $L_i = \displaystyle\int_0^\infty R(s)ds$	NAME uses τ_L in plume rise and turbulence schemes.	Decay time scales for auto correlation coefficient $R(\tau) = \dfrac{\overline{u'(t)u'(t+\tau)}}{\sigma_u^2}$ for lag τ, $R(s) = \dfrac{\overline{u'(x)u'(x+s)}}{\sigma_u^2}$ for lag s.

Sensible heat flux	H or Q $H = Q_H$ $= \rho C_p \overline{w'\theta'}$	Correct sign of H (and time transition) is very important for NAME.	Indirectly from lidar third moment $\overline{w'}^3$. (Gal-Chen et al 1992)
Flux of temperature fluctuation	$\overline{w'\theta'}$		Or from w_* as below.
Convective velocity scaling . Associated with speed of convection (unstable).	$w_* = \left[hg \frac{\left(\overline{w'\theta'}\right)}{\theta} \right]^{\frac{1}{3}}$	Used in NAME for calculating turbulence, as $w_* = u_* \left[\frac{z_i}{k\|L\|} \right]^{\frac{1}{3}}$	From $\sigma_w^2 \approx \beta w_*^2$ (Angevine et al 1994) where $\beta \approx 0.52$ within $0.2 < z/h < 0.5$

Table 3.1 List of variables used in the Met Office NAME dispersion model with emphasis upon those that are measured by lidar or closely related to lidar quantities.

While many of the parameters listed in table 3.1 can be measured using a single Doppler lidar, obtaining one velocity component along the beam, significant improvements in accuracy and coverage are possible using two Doppler lidars simultaneously. Use of a single lidar to derive boundary layer parameters necessitates making certain assumptions on flow continuity over inhomogeneous surfaces. This assumption is not valid over heterogeneous areas such as cities. Dual-lidar operation relaxes this constraint, by measuring two velocity components, at the same point in space. The use of two lidars allows measurements to be made for a localised target area, and both measured components then come from the same point viewed from different directions.

So far as the Project Team is aware, no group has previously tried compile such a list of dispersion model variables that are in principle amenable to lidar observation prior to a measurement campaign. Examples of observations, measured flow field phenomena and the derivation of additional parameters are presented sections 5 and 6. In section 6 of this report the Project Team compare the parameters from our lidar results with the mesoscale/NAME data sets.

4 TRIALS DESCRIPTION

4.1 Introduction

After a review of a number of possible trial site locations throughout the UK it was been decided to conduct the trials around the western edge of London as this areas is as representative of a typical rural urban boundary as anywhere in the UK. A survey of West London indicated RAF Northolt as a preferred location from which to conduct the trial. There were a number of advantages in working from RAF Northolt including:

- it being a near optimum location for the lidars to monitor the rural urban boundary,
- the lidars could operate from an extended baseline with clear fields of view and
- the equipment could be left in position for the duration of the trial.

The location of RAF Northolt is the western edge of London. The station is about 10 km north of Heathrow Airport and 7 km to the west of the M25. From the airfield it is possible for the lidars to probe representative rural areas around Denham and the Grand Union Canal to the north west. When the wind was blowing from the south east the area to the immediate west of Uxbridge was also considered rural. Urban environments probed included Harrow (northeast), Wembley (east) and Ealing (southeast).

4.2 Winter trial description

Prior to the formal ISB-52 trials a trial local to Malvern was initially undertaken with the intention to test the Dual Lidar systems and refine the associated experimental technique prior to deploying to RAF Northolt. The first full deployment to West London would have been for the winter trial. However world events precluded this because of the commencement of the Gulf and access to an operational RAF airbase being curtailed. Therefore an alternative location to RAF Northolt was required. Given the short notice it was decided that the winter phase trial would be continued local to Malvern.

The winter field trial was conducted in the vicinity of the QinetiQ base at Malvern, Worcestershire[6,7]. The QinetiQ lidar was based permanently at the QinetiQ site. On the 17th March, the first day of the trial, the Salford lidar was also sited at the QinetiQ site, approximately 25 m from the QinetiQ lidar. On the 18th and 19th March the Salford lidar was moved to the Three Counties Show ground, which was approximately 3 km south of the QinetiQ site. The longitude and latitude of these sites is detailed in table 4.1. The two sites (QinetiQ site and Three Counties show ground) were both approximately 1.5 km east of the ridge of the Malvern Hills.

Site Name	Location		Deployment
QinetiQ Car Park	45 1 N	78 5 W	Yes (QinetiQ Lidar)
3 Counties Car Park	42 1 N	78 9 W	Yes (Salford Lidar)
Hall Green	45 5 N	80 6 W	Not used
Malvern Common	44 3 N	77 8 W	Not used

Table 4.1 Lidar position information.

The QinetiQ site is approximately 1.5 km to the east of the ridge of the Malvern Hills. The Malvern Hills are a ridge of hills approximately 13 km long orientated in the north - south direction and approximately 300 - 360 m above the surrounding terrain (425 m above mean sea level).

The Three Counties Show ground was the second site used, this was approximately 3 km 9° east of south of the QinetiQ site. This second site was therefore also approximately 1.5 km east of the Malvern hill ridge. The crest of the hill at this latitude is approximately 250 - 280 m above the surrounding terrain.

The trial geometry is shown in figure 4.1. The QinetiQ lidar was located in a car park at the northern edge of the QinetiQ site. The Salford lidar was deployed in the southern car park of the Three Counties Show ground. Further details of these locations are given in Table 4.1 The QinetiQ team were located at ten figure grid reference SO 78472 45036, the Salford team at SO 78925 42112, and the intersections of the beams were roughly over SO 800426 (six fig reference). Two other provisional sites where prepared but in the event not used because the ambient winds where always from the East for which the QinetiQ to Three Counties baseline was optimum.
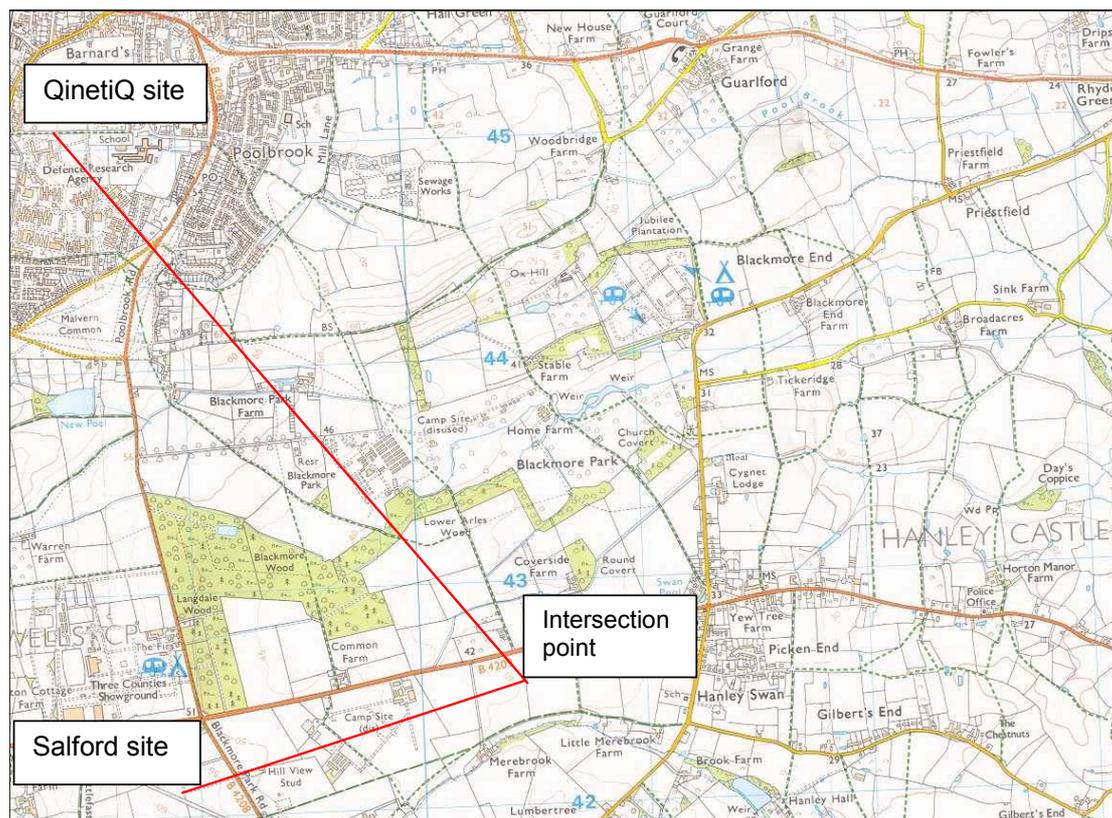
Figure 4.1 Map illustrating the trial geometry.

Dual Doppler lidar data was collected on the 18th and 19th March using three different line-of-sight configurations. Before the trial, on Tuesday 11 March 2003, high pressure was to the West of the British Isles; showery rain had passed the British Isles on the 12th. Then high pressure was centred over Scotland on Thursday 13 March 2003 (first day of measuring) with the UK being mainly dry with broken cloud. The

centre of the high was over the North Sea on Friday 14 March 2003 and the UK had a pleasant sunny day. On Saturday 15 and Sunday 16 March 2003 it was also largely dry & sunny; from Monday 17 to Wednesday 19 March 2003 to country was still under anti-cyclonic conditions, warm and dry, with fog or some frosts at night. On Thursday 20 March 2003 there was a front over the Irish Sea up to S. Scotland. During the trial, except on the Sunday (when data were not taken) the weather was anti-cyclonic, and cloud cover slight and winds speed light and variable.

4.3 Summer trial description

The summer trial was conducted at RAF Northolt [8,11] using a trial geometry as shown in figure 4.2. The QinetiQ lidar was located at the north west edge of the airfield. The Salford lidar was deployed in the south-east part, adjacent to the A40. The lidars were positioned either end of the runway with the north west-south east orientation, 127°. Further details of these locations are given in Table 4.2.

Site Name	Location	
QinetiQ Lidar	85 4 N	09 1 W
Salford Lidar	84 6 N	10 5 W

Table 4.2 Lidar position information.

At RAF Northolt the baseline separation between lidar stations was 1574 m. Depending upon the mean wind direction and the nature of the dual lidar scan pattern being used beam intersections occurred at different locations. These locations are listed in table 4.3. The key period for the observations was between the 8th and 23rd of July 2003. The weather throughout this period was variable, table 3.4 lists details of the general conditions around the Northolt area.

Pattern No	Location	Intersection point co-ordinates		Reason
1	Rectory Park, Yeading	183630	512 838	Urban vertical
2	Ickenham	186 216	506 812	Rural vertical
3	South Ruislip	186000	512000	Urban horizontal
4	Mid point of runway	184 986	509 847	Resolved vertical

Table 4.3 Evaluation of the lidar beam crossing points.

A general summary of the conditions is as follows:

From the 8th to the 15th July there was a high pressure system situated over the north sea, which gave very light surface easterlies. During this period the temperature were extremely high, as were atmospheric aerosol concentrations. Lidar data, not shown, gives a low boundary layer height during daylight hours (approximately 600 m) during this period.

From the 16th to the 19th there were scattered and heavy thunderstorms throughout the south of the country. The central London region was hit by a series of thunderstorms that was tracked moving south easterly from France. The boundary layer throughout this period was therefore highly convective.

From the 20th to the 23rd July a low pressure system moved in from the south west giving southwesterly flow across the country. There was some stratocumulus cloud cover and the atmospheric boundary layer was well mixed with near neutral condition. Due to the rainfall in the past week and the well mixed atmospheric conditions the concentrations of aerosol in the atmosphere was much lower than previously.
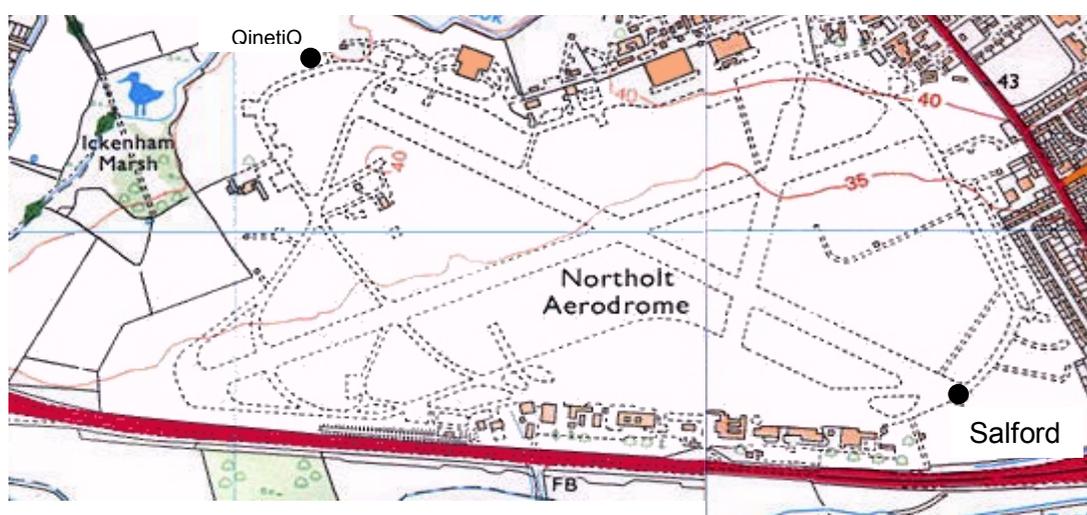
Figure 4.2 Map illustrating the trial geometry.

The general trial scheme was for both lidars to calibrate their alignment using local land marks after the vehicles had been levelled. For calibration of bearing and elevation angles it was found convenient to use the steeples of local churches, the Spire of an Ealing church for the QinetiQ lidar and the Harrow on the Hill spire for the Salford lidar. All data was time stamped from a GPS signal.

Once the lidar systems were calibrated a VAD was undertaken to determine the predominant wind direction. (The VAD data is also useful for comparing the results from the two lidars and checking system bias). Once the wind direction was identified the lidar beams were orientated to make the dual lidar observations. A number of scan patterns were employed, each designed to optimise the observation of a particular component of the wind flow field. Details of these scan patterns are given in section 4.5.

For much of the trial the lidars were operated in a real time data processing mode. This allowed the operator the ability to continually check that the lidar performance was satisfactory during a data collection base. The QinetiQ lidar sampling rate was of the order of 0.2 Hz, the Salford system was 0.12 Hz. Range gates were of 112 m

length unless otherwise noted. A limited amount of data was collected by the QinetiQ lidar operating in 'raw' mode at 50 Hz. However it was observed that operation in this mode was causing excessive arcing across the anode which it was feared would lead to damage in the TEA laser head. Due to the concerns that raw mode operation would damage the lidar the mode was only used by a single lidar once to acquire sufficient data to allow subsequent assessment.

In support of the lidar observations an automated weather station with acoustic anemometer was located besides the Salford lidar. This system was deployed to gather surface meteorological data wind speed and direction, temperature and solar radiation measurements at 2m. From this data it is intended to calculate the atmospheric stability in order to classify and quantify the level of atmospheric stability under which the lidar observations were made.

For the trials the mesoscale version of the UM was run, including the incorporated meteorological observations, for the duration of the experiment. Using the mesoscale model data as starting conditions, the NAME dispersion model was then also run for each of the days of the experiment.

4.4 Summary of data gathered and derived parameters
Section 3 of this report identified the key atmospheric phenomena to be observed. The conclusion was that the measurement of the height of the top of the planetary boundary was of top priority. Profiles of wind speed, wind direction and turbulence were also required. To achieve a set of observations representative of the statistics of pollution dispersal phenomena it was also recommended to dwell along one line of site for at least ten minutes. However dwelling along one line of site does not allow observation of large volumes of the atmosphere. Consequently a number of scan patterns were devised to unambiguously observe specific dispersion model parameters under different ambient conditions. That each of these scan patterns was optimum for observing a specific phenomena implies that the scan pattern would be limited for other observations. Recognising these limitations was a key lesson learnt during the Project, as were the strategies adopted to ameliorate these limitations during the trials.

It was also found that the limits on usable range combined with the relative slow scan speed of a lidar system became significant design constraints when planning the field scanning patterns.

Three basic types of scan techniques can be used;

- VAD (or Azimuth) scan (which sweeps out an inverted cone at fixed elevation angle),
- RHI (or Elevation) scan (which sweeps a vertical semicircle or sector of a circle for a fixed azimuth),
- Fixed Beam (Stare) (which maintains a fixed elevation and fixed azimuth for a specified sampling period, say 10-15 minutes, long enough for reliable turbulence statistics).

During the field trials these sinlge lidar observations were supported by scans that involve dual Doppler lidar observations. To achieve this a combined technique has been developed for this study:

- Dual Fixed Beam: Data from two Fixed Beams combined at their intersection point.

Table 4.4 outlines the scanning techniques and the meteorological parameters obtained from the scan and the required duration of the scan.

Scan Technique	Measured Parameter	Derived Parameter	Required length of scan (minutes)[*]
Fixed Beam	Radial wind velocity profile, v_r Radial wind velocity variance profile, v'^2_r System estimation error	Energy dissipation rate , $\ulcorner$ Integral length scale, L_I Integral time scale, T	15
Vertically pointing fixed beam	Vertical velocity profile, w Vertically velocity variance profile, w'^2	Temperature flux, w't' Sensible heat flux at the surface, H Convective velocity scaling , w*	15
Dual Fixed beam[⊗]	Profiles of the two components of horizontal wind, u and v Profile of variances, u'^2 and v'^2	Energy dissipation rate , $\ulcorner$ Integral length scale, L_I Integral time scale, T	15
VAD (azimuth scan)	Wind speed profile, u Wind direction profile Back-scatter Intensity profile System offset	Boundary layer height	15
RHI (elevation scan)	Profiles of area averaged values for u, v and w Profiles of area averaged values for u'w' and v'w'	Friction velocity, u* Roughness length scale, z_0 Roughness displacement height, d (N.B. for these parameters measurements must be within the surface layer)	30

Table 4.4 Parameters measured and derived from the various scan strategies

Using the fixed lidar beam values for the kinetic energy dissipation rate, integral length scale can be derived from the power spectra [17,31]. The integral timescale can be estimated from the velocity lag autocorrelation curve [33]. From using a vertically pointing fixed beam the convective velocity scaling can be estimated. From this an estimate of the heat flux, w't' and sensible heat flux at the surface, H, can then be calculated [17].

---

[*]time includes time needed for taking of noise files for data processing procedure

[⊗]wind direction profile needed to transpose radial winds to u & v components.

In conclusion ISB-52 developed a number of differing scan patterns, each optimised for a different observation either in terms of parameter to be derived or to reflect the stability of the ambient conditions. These different scan strategies yield differing data sets which in turn necessitates differing strategies for using the lidar data to estimate the dispersion model's parameters.

4.5 Scan strategies
The developed scan strategy was further refined depending upon the forecast meteorological situation. There are two basic strategies depending upon ambient conditions. If the situation is convective then VAD/Fixed & Dual measurements will be made. However if ambient conditions are near neutral the measurements will be VAD and scanning RHIs.

The VAD's are important for two reasons:
1) hourly boundary layer height is a priority for NAME and ADMS;
2) wind direction from VAD is needed to set the lidar beam orientations for an RHI.

4.5.1 Convective conditions
Under convective conditions the measurements would focus on deriving the wind profile and turbulence data. This would be achieved through the use of VAD and staring dual beam. Ideally this should be undertaken when conditions of strong day-time convection or strong urban nocturnal heat flux is expected. This can be further sub-divided into morning transition study from dawn until mid-afternoon maximum boundary layer turbulence and a separate evening transition study from mid-afternoon until stable/nocturnal conditions established. From this the boundary layer growth and its evening decline can be to followed. From the dual lidar information profiles of wind speed, direction and turbulence can be derived. Since convective scan pattern uses fixed beams (stand and stare) the time period of sampling (15 minutes) is designed for reliable turbulence statistics, turbulence spectra, and eddy dissipation rates.

The structure of the scanning for the convective pattern was set to be a VAD on the hour every hour with an allowed duration of 15 minutes. This would then be followed by three fixed dual beam stares with both lidars of 15 minutes each. If slippage in timing occurs due to on site practical limitations, it is important to keep VAD's on the hour to match ADMS model.

In practice VADs seldom occurred upon the hour for a number of practical reasons, however the trial team did their best to ensure that the VADs were made as close to the hour as possible. Also the practice was adopted of the QinetiQ lidar undertaken a hemispherical RHI along the mean direction of the wind whilst Salford did the VAD observation. To ensure that the lidar beams intersected the boundary layer at least once with a high SNR the experimental strategy was adjusted so that four or five heights were probed per column. To retain the hourly cycle the staring times were reduced to lengths of 10 minutes. This strategy meant that it took two hours to measure both the rural and urban columns of air. When conditions were deemed to be evolving more rapidly observations of the rural column were abandoned to allow the urban column to be monitored on an hourly cycle.

The geometry for the fixed dual measurements needed be designed to achieve the correct beam intersections. Typically angles were set to allow beam intersections at set heights in the column: typically these heights were 100, 200, 400, 800 and 1600 m. Further considerations are also necessary to determine the location of the vertical column. Such considerations needed to optimise these beam intersections to allow obtaining the flow vector and vertical fluctuations with the minimum number of assumptions.

4.5.2   Near Neutral Pattern

If the conditions are closer to near neutral then the measurements will concentrate on deriving surface layer parameters through the use of VAD plus RHI scans. This is optimum when moderate winds and cloud covers occur causing the dominant turbulence to be due to mechanical shear. Under these conditions the measurements will seek to highlight the effects of surface roughness and upwind fetch. It may also prove possible to identify spatial area averages of said parameters and detect differences in the flow field over the urban and rural environments.

Again emphasis was given to making a VAD on the hour every hour for which 15 minutes duration was allowed. (10 minutes for the scan and five to set up the VAD and analyse the results). A real time analysis of the VAD was used to determine the mean wind direction this is crucial for determining the orientation of the subsequent RHIs. As with a measurement made by conventional anemometer the turbulent flow is influenced by the upwind surface type over which the air has flown. Thus it is necessary to establish the wind directions at the edge of the rural to urban boundary and identify the type of substrate or surface type each beam is effectively observing above. Once the VAD had been analysed then two RHI scans would follow each of 30 minutes duration. The two lidars were deployed for RHI 1 & 2 as follows:

RHI 1 The Salford lidar pointed downwind over London and QinetiQ pointed upwind over the rural.

RHI 2 Salford pointed orthogonal to the wind whilst QinetiQ pointed orthogonal to wind and at 180° from the Salford direction.

For the RHI scans the maximum elevation for both lidars was set at 45° to match the design limit of the Salford instrument. A requirement for the subsequent theoretical analysis and the associated assumptions therein is that the RHIs should be made along bearings parallel and orthogonal to the mean wind direction.

4.6 Review of trials experience

This trial was the first time that the project team had endeavoured to measure the wind flow field over the rural urban interface under evolving conditions using dual Doppler lidar. Despite the considerable planning that went into preparing for the trials a number of valuable lessons were learnt during the course of the trials.

Generally it was found that the dual lidar observations were too slow to be made to observe rapidly evolving conditions. Due to this, it was decided that for periods close to sunset scanning VAD and RHIs rather than staring measurements would be made. This was adhered to even for days when most of the time was spent in a staring

configuration. For such days after the sun had set the project team would revert to making staring measurements.

After making a set of dual Doppler lidar measurements that feature observations into both the rural and the urban environments, subsequent days of dual Doppler lidar concentrated the dual observations solely on the urban. This approach was adopted to allow more observations to be made of the development of conditions in the urban environment. Under this regime conditions in the rural were tracked by the hourly VAD scan undertaken by the Salford lidar and an RHI from the urban to the rural by the QinetiQ lidar.

For the Dual Doppler lidar measurements to derive unambiguous vertical flow information initially the two intersection points were chosen in the plane of the lidars and beyond the lidars. This allowed one sampling column to be in the rural and the other in the urban. Whilst this configuration allowed vertical information to be extracted from rural and urban environments the penalty for doing this was the need to use low elevation angles, (typically 1.41°, 2.81°, 5.61° and 11.11°).

The justification for undertaking the in plane measurements at low elevation angles beyond was that the expected differences between the rural and urban environments would be more prominent in the layers closer to the surface. This is because higher in the atmosphere the turbulence due to the surface artefacts becomes increasingly mixed. The result of this mixing is that the region of the surface that is deemed to influence the turbulence structure of flow (or 'footprint') becomes increasingly large. To ensure that some measurements were made from which surface effects could be ascertained it was necessary to undertake some measurements as low as possible in the atmosphere.

The derived vertical velocity data is the line of sight velocity multiplied by the sine of the angle of elevation, which for a small angle of elevation gives a small vertical velocity component. An alternative in-plane scan strategy had to be devised to allow accurate monitoring of the vertical flow. A new experimental strategy was used where only a single column of air was sampled and the column occurred mid way between the two lidars. For such a configuration the angles of elevation become large (Typically 7.24°, 14.26°, 26.94° and 42.00°) but no comparison of the rural urban interface could be made. However given that it was felt that the observations to make these comparisons were taken too long this was not seen as a major issue.

The exceptionally hot conditions of the period of the 8th to the 15th July caused some technical difficulties. The heat caused thermal expansion in some of the optical component mounts leading to misalignments and a loss of operational performance. This was compensated for in the field by adjustment of the appropriate optics. The heat also proved problematic for the QinetiQ laser cooler. That issue was resolved by removing the cooler from inside the QinetiQ lidar van, then repositioning it to allow the maximum amount of wind to blow over it.

5 DAViS

5.1 Introduction

As part of the ISB-52 project software was developed to visualise the measured data and retrieved products from both Doppler lidars involved in the project. The main software developed was the ***Doppler Analysis and Visualisation Software***, DAViS [9,10]. This software loads and processes the lidar data in order to visualise it in various ways in 2D or 3D.

Whilst the two lidars are nominally identical small differences in the lidar and different scanner mechanisms means that they save data in different formats. Therefore the process of visualising the data required the following two steps:

- Converting the lidar data into a common data format (DML).
- Loading data in the common format and visualising the data.

DAViS was written in C++ in an object-oriented design and was developed in an Unix X11 environment. It was successfully compiled and used under SGI IRIX (version 6.5) and Linux (Kernel 2.4). To ensure and stable and fast development some third-party software packages have been used:

- SGI's *Open Inventor* with its *Motif* bindings for interactive 3D rendering.
- Trolltech's *Qt* for development of menus, File-IO-operations and 2D graphic windows.

The software was designed on a SGI graphics workstation which was specially purchased for this project. The SGI *Fuel* workstation was equipped with a 64-Bit processor for faster floating-point calculations and a V10 Graphics card which enables OpenGL accelerations and stereo graphics. The software was designed to run on other Unix platforms, but has shown slower reaction times in the interactive 3D display and the stereo graphics cannot be used.

Using the software *doxygen* an on-line documentation in HTML of the source code was produced. It enables any programmer easily to understand the code already written and to add further extensions.

The main features of DAViS are:

- Load data in the DML data format.
- Visualise lidar data in 2D as RHI and PPI.
- VAD analysis of PPI lidar data with various options.
- Interactive 3D display for lidar data (RHI and PPI) and wind information.
- Stereo graphics for the 3D display.

Three-dimensional displays are difficult to produce on a two-dimensional monitor screen. To make the impression more realistic stereo graphics can be used. Stereo graphics produces two different pictures, one for each eye to give the illusion of viewing an object in 3D. To use stereo graphics there are hardware as well as software requirements. Further details about the hardware are given at http://prswww.essex.ac.uk/lidar.

The DAViS software has been ported to Linux to enable it to be distributed more widely. This is now possible due to the technical development of graphics hardware on PCs. In the project it was successfully ported to SuSE Linux on a University of Essex PC, but it may well not port to other versions without further development.

5.2 Results of visualisation

In this section, results are presented from the visualisation of lidar data with DAViS. The data used was recorded in the winter trial in March 2003 in Malvern and in the summer trial in July 2003 at RAF Northolt.

A small selection of the results is now presented. First examples of two-dimensional plots of the data are presented before examples of the three-dimensional visualisation are shown. More detailed examples of the visualisation work are on a web page launched at the University of Essex at *http://prswww.essex.ac.uk/lidar* . The web page not only contains more snapshots of DAViS and the visualisation, but also movies from the three-dimensional display.

5.2.1 2D plots

The two-dimensional plots consist of PPIs, RHIs, VADs and time series of line of sight data.

The summer trial in July 2003 produced a number of interesting data sets. To start a series of measurements, PPI scans were measured to establish the mean wind direction. Figure 5.1 shows such a PPI of the radial Doppler velocity at 8:43 on the 23rd of July 2003. The radial velocity is in the majority positive on the bottom left (south-west) part of the PPI. On the opposite (north-east) the velocity values are mostly negative. This points to a linear wind flow which can be more closely examined with a VAD.

Figure 5.2 shows a corresponding VAD, produce out of the above described PPI scan. Based on the assumption that positive velocities are towards the lidar and negative ones are away from the lidar the wind flows from the south-west to the north-east.

To observe what happens in the vertical plane above the lidar a 180 degree RHI by the QinetiQ lidar is very useful. The intensity RHI for example, which is displayed in Figure 5.3, shows a clear layer, which could be the top of the boundary layer or clouds. The velocity RHI (Figure 5.4) at the same time shows also a clear signature at this layer's position.
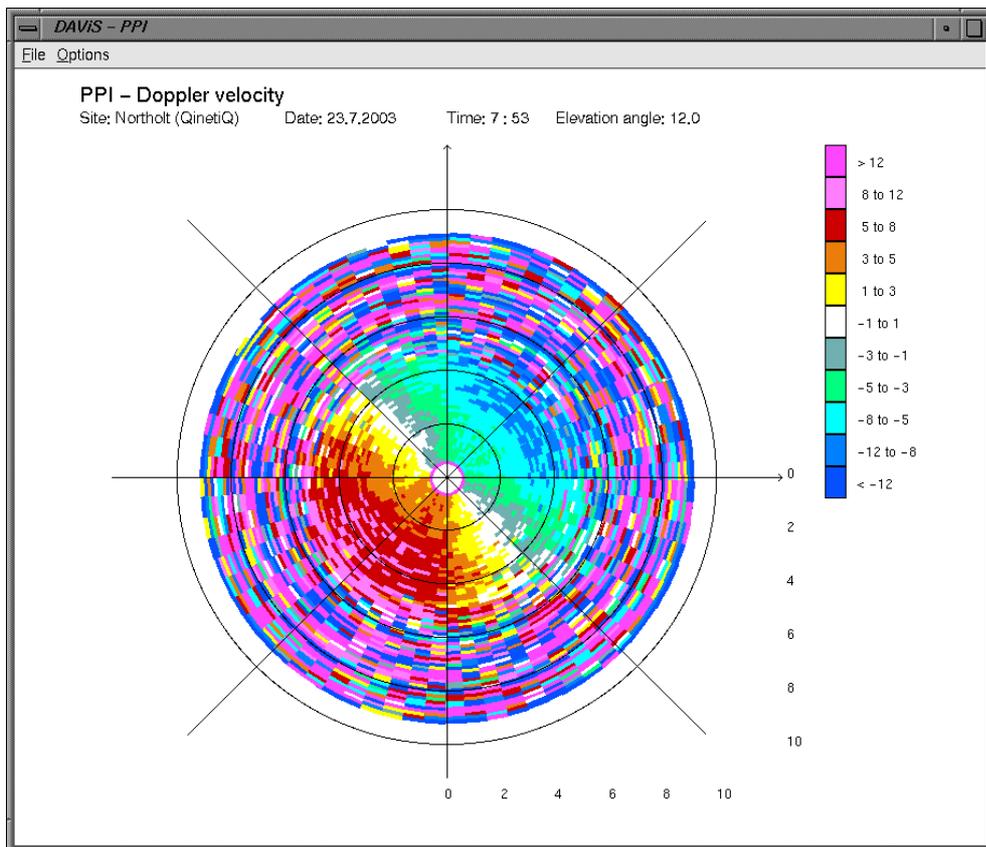
Figure 5.1 PPI of Doppler velocity recorded by the QinetiQ lidar on the 23rd July at 7:53.
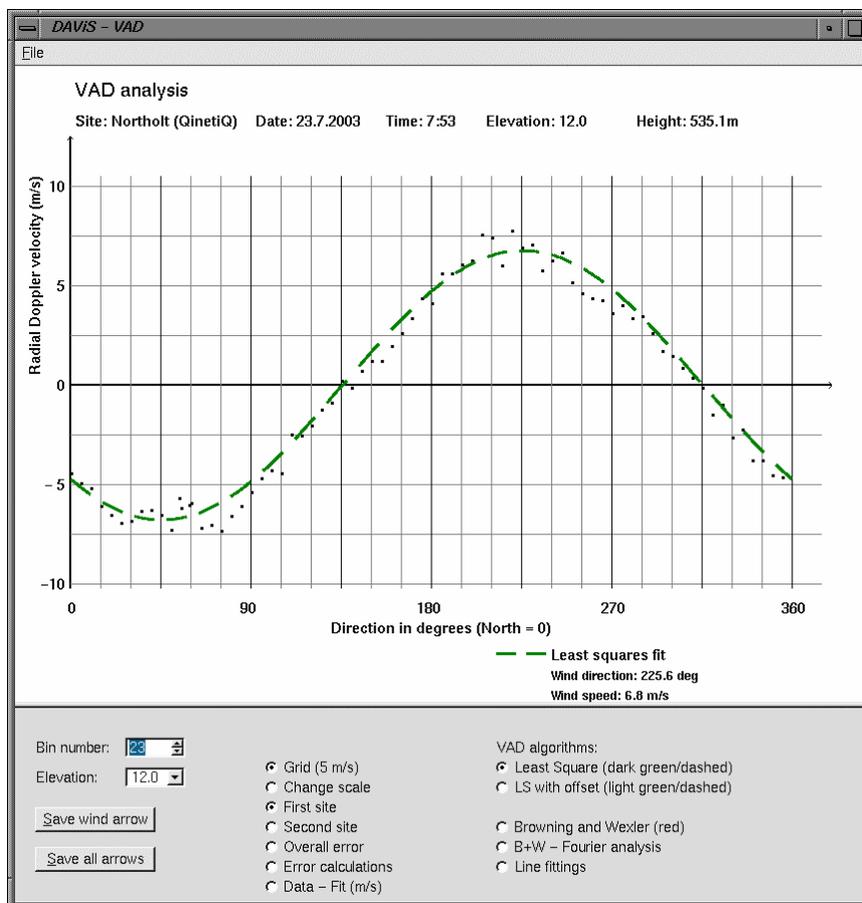
Figure 5.2 VAD analysis of PPI data shown in figure 10.
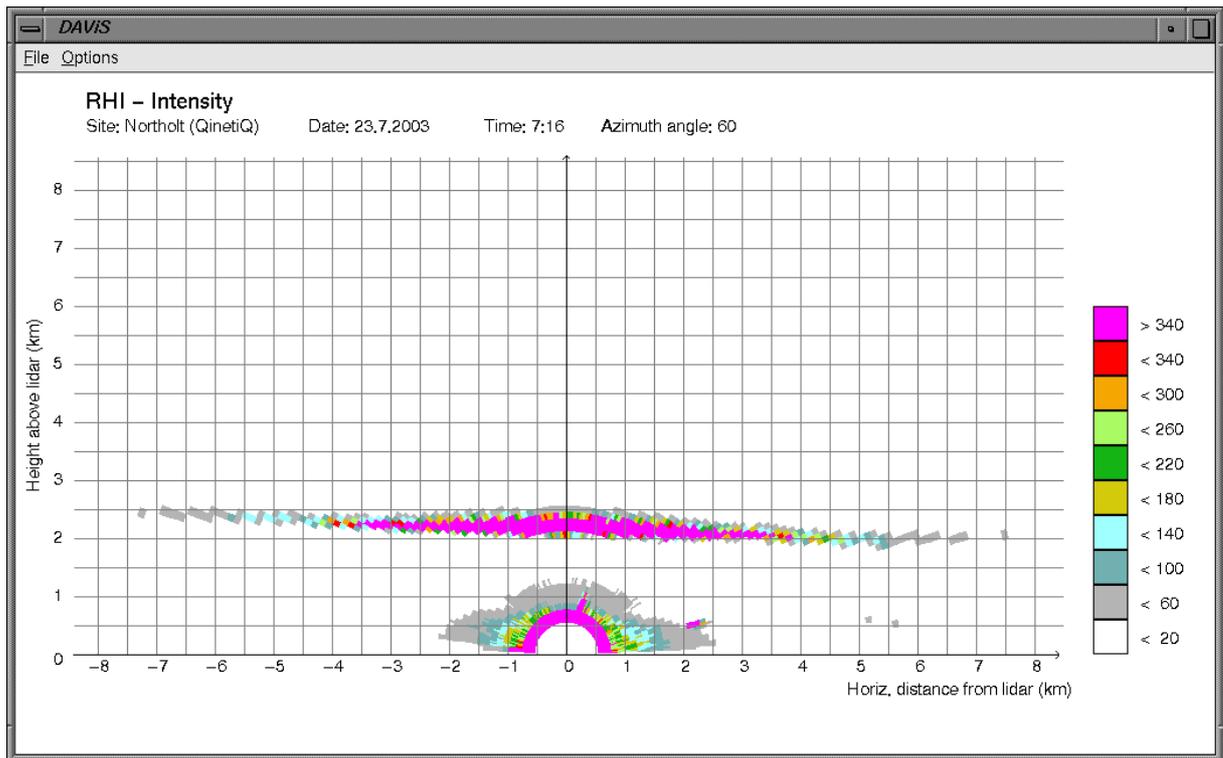
Figure 5.3 Intensity RHI plot recorded by the QinetiQ lidar on the 23rd July at Northolt. A layer can be clearly seen.
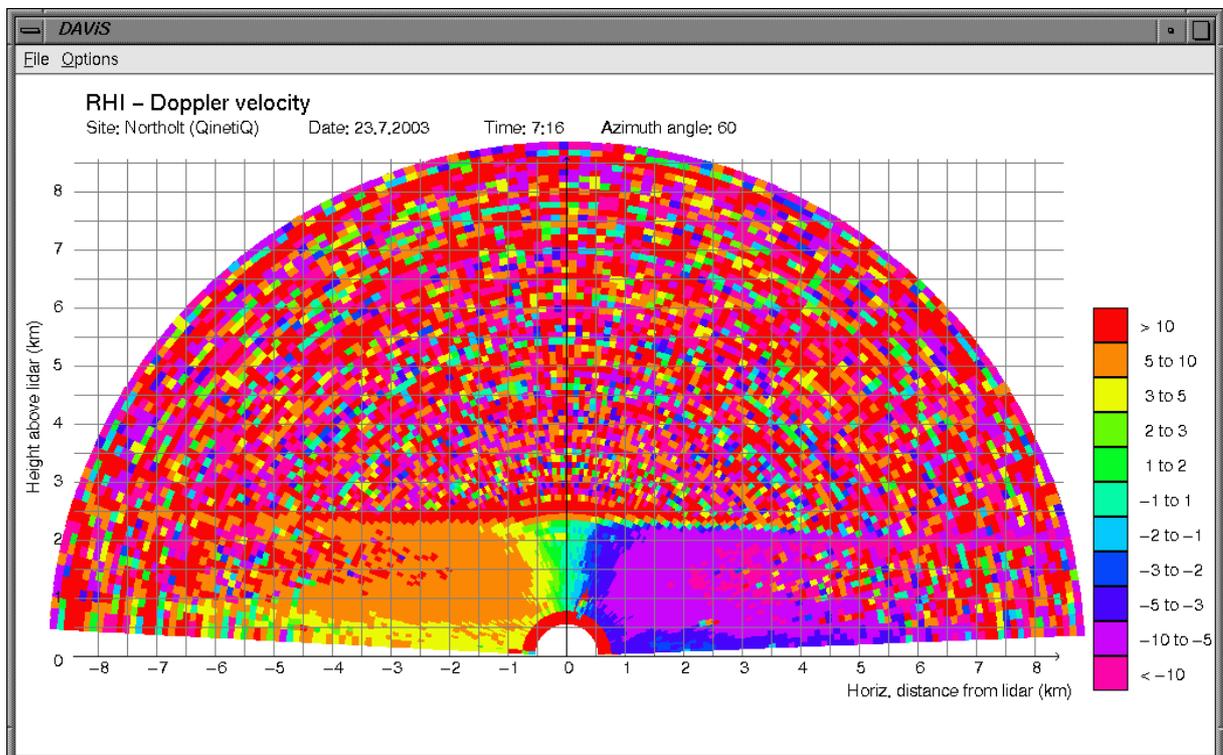
Figure 5.4 Radial velocity RHI of the same scan as in figure 5.3.

5.2.3 VAD analysis

One common method to retrieve wind information from single PPI (lidar or radar) measurements is the VAD display or method. In a VAD the radial velocities are plotted depending on the azimuth in which they are recorded. For a uniform wind flow this display should result in a sine curve, in which the maximum is related to the horizontal wind speed and the location of the maximum in azimuth gives the direction in which the horizontal wind is flowing.

Figure 5.5 shows an example of a VAD plot measured during the winter trials in Malvern on the 18th of March 2003. Two fits are shown. The first dark green fit is a standard least squares fit of a sine curve. This curve does not fit very well, because the radial velocity data has apparently an offset. That is why the second least squares fit, shown in light green and smaller dashes, of a sine with offset fits the VAD much better.
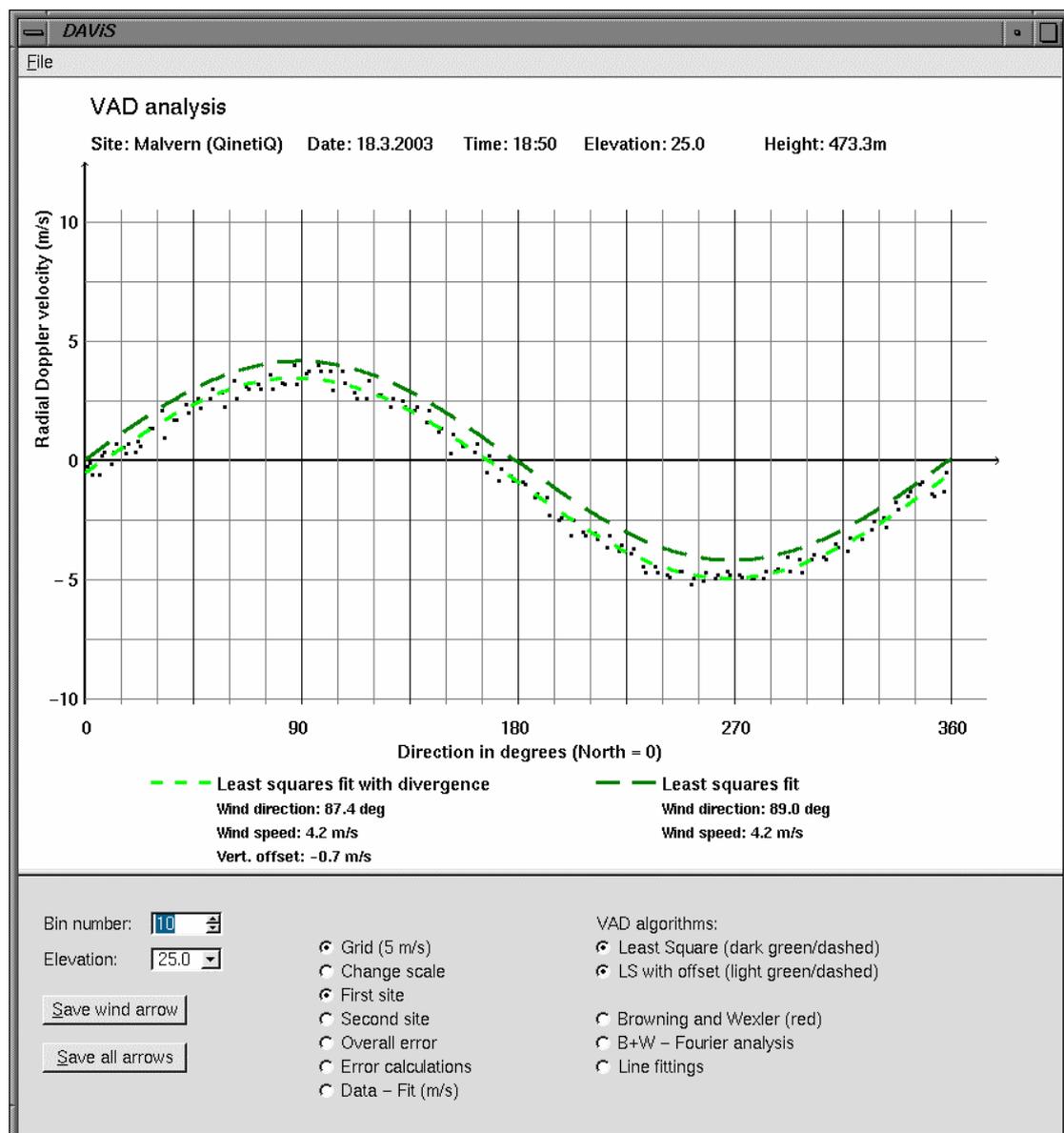
Figure 5.5 DAViS's window to display and analyse a VAD. The data shown was measured during the winter trial in Malvern on the 18th March.

5.2.3 Analysis of LOS data in the vertical plane
If the two lidars measure along the vertical plane which passes through the sites of the lidars, then the horizontal wind component along the plane and the vertical velocity component can, in principle, be determined using analysis derived during the project.

Figure 5.6 and 5.7 show two examples of the LOS plane analysis. Both cases were recorded during the summer trail in Northolt on the 23rd of July. On this day two series of scans were taken at which the lidar beams were directed towards each other at the same elevations. This meant that the beams intersected in the middle between the lidars.

The first case, shown in figure 5.6, was recorded at 17:02 and the elevation angle was 42 degrees at both lidars. That meant that the point of intersection of the beams was at about 711 metres height. On the left side the radial velocity of each lidar in bin 9 is plotted over the 10 minutes duration of the scan. On the right side the calculated vertical velocity and the horizontal wind component along the plane are plotted. Both are again plotted over the 10 minutes duration. Both calculated variables show consistency.

The second case, shown in figure 5.7, was recorded 24 minutes later at 17:26 with elevation angles of 14.2 degrees. This resulted at height of 206 metres in which the lidar rays intersected. While the horizontal component along the plane is still consistent, the vertical component has become noisy. This results from the lower elevation angle at which the measurements were taken. At low elevation angles the equations becomes ill-conditioned.
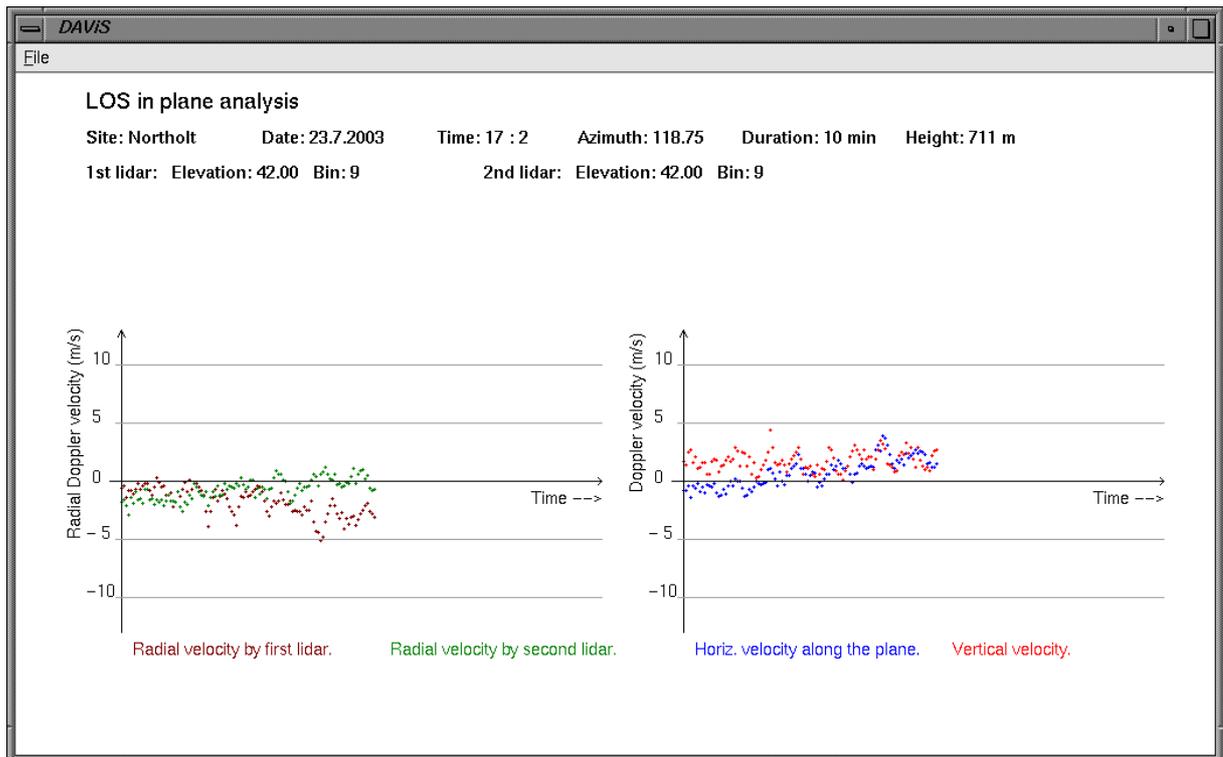
Figure 5.6 Result of the LOS analysis in the vertical plane at the summer trial in Northolt on data measured at 17:02 on the 23rd of July 2003 at a height of 711 metres.
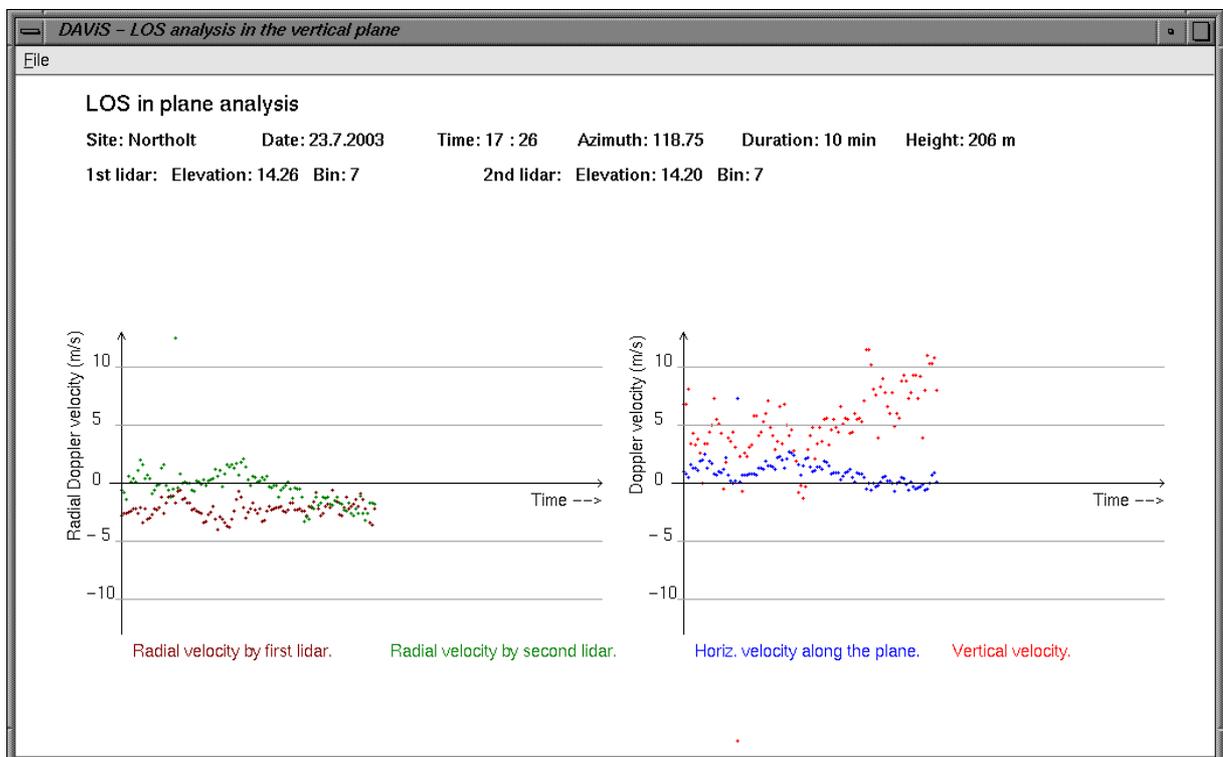
Figure 5.7 Result of the LOS analysis in the vertical plane at the summer trial in Northolt on data measured at 17:26 on the 23rd of July 2003 at a height of 206 metres.

5.2.4 3D visualisation

One of the strengths of DAViS is the three-dimensional display of data. Unfortunately it is quite difficult to present results of three-dimensional displays on flat paper or on a monitor screen. Two techniques can help to let the user see the data in 3D: movement of the scene and stereo graphics. Both techniques are implemented in DAViS.

In the following examples various combinations of lidar scans are visualised to show the visualisation ability of DAViS.

QinetiQ PPI + Salford PPI

The first example (figure 5.8) shows two PPI measurements measured by both lidars. In the figure the observer views the scene from north to south and the full cone in the front belongs to the measurement of the QinetiQ lidar. The cone, on the right, which lacks 65 degrees in azimuth, belongs to the Salford lidar.

Both PPIs were recorded at low elevations (QinetiQ lidar: 12.0^{o} ; Salford lidar: 17.1^{o}). That is why the top of the boundary layer is not visible and the scene looks shallow. This case, however, shows how both lidars agree in the measured data, with the positive velocities (yellow and red) on the right (west) and the negative velocities (green and blue) on the left (east).

Salford RHI + Salford RHI

On the 21th of July at 14:06 and 14:38 the Salford lidar measured two RHIs in different directions. Figure 5.9 shows a snapshot of the resulting display.

QinetiQ RHI + Salford PPI

The second example shows an RHI, measured by the QinetiQ lidar, and a PPI, measured by the Salford lidar, combined in 3D. The data was measured at the summer trial in Northolt on the 23rd of July at 11:17.

Figure 5.10 shows the radial velocity data measured by both lidars. Comparison of both scans indicates, as in the last case, the velocity values agree very well with each other. Especially from the intensity display of the scan (shown in figure 5.9), it can also be seen, that the PPI elevation angle is too low to intersect with the top of the boundary layer which is visible in the RHI.

The RHI seems to suggest that there is a change in the top of the boundary layer. While in the west direction (left side in figure 5.8), there appear to be two layers high above some noise, the height of the top of the boundary in the east (in the right of the RHI in figure 5.8) seems to be a constant as expected.
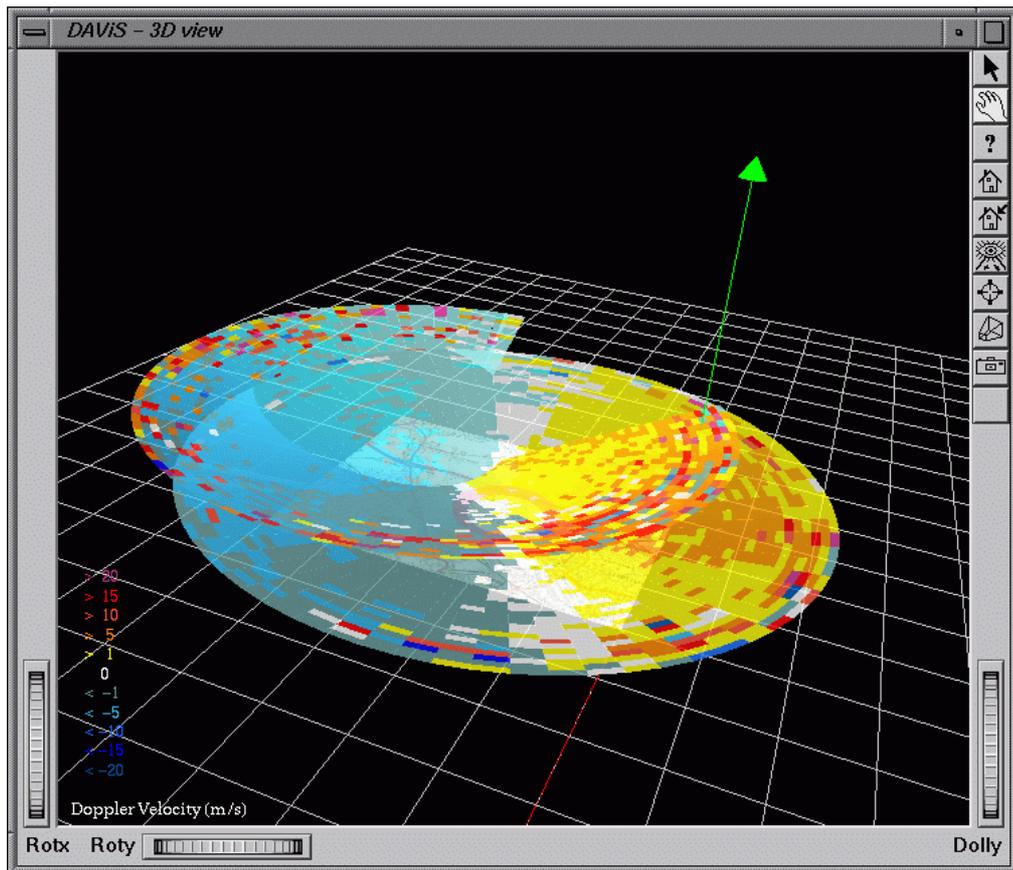
Figure 5.8 A 3D display of radial velocity measurements of by the QinetiQ lidar and by the Salford lidar at Northolt on the 23rd of July at 18:23.
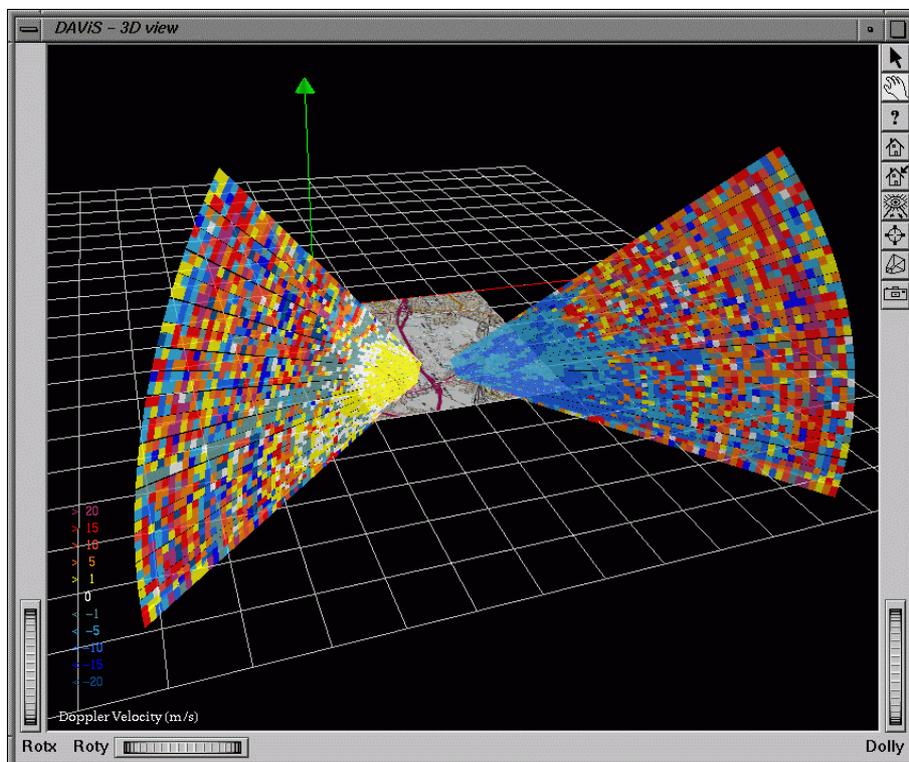
Figure 5.9 Two velocity RHI scans by the Salford lidar combined. The data was measured at 14:06 and 14:38 on the 21st of July.
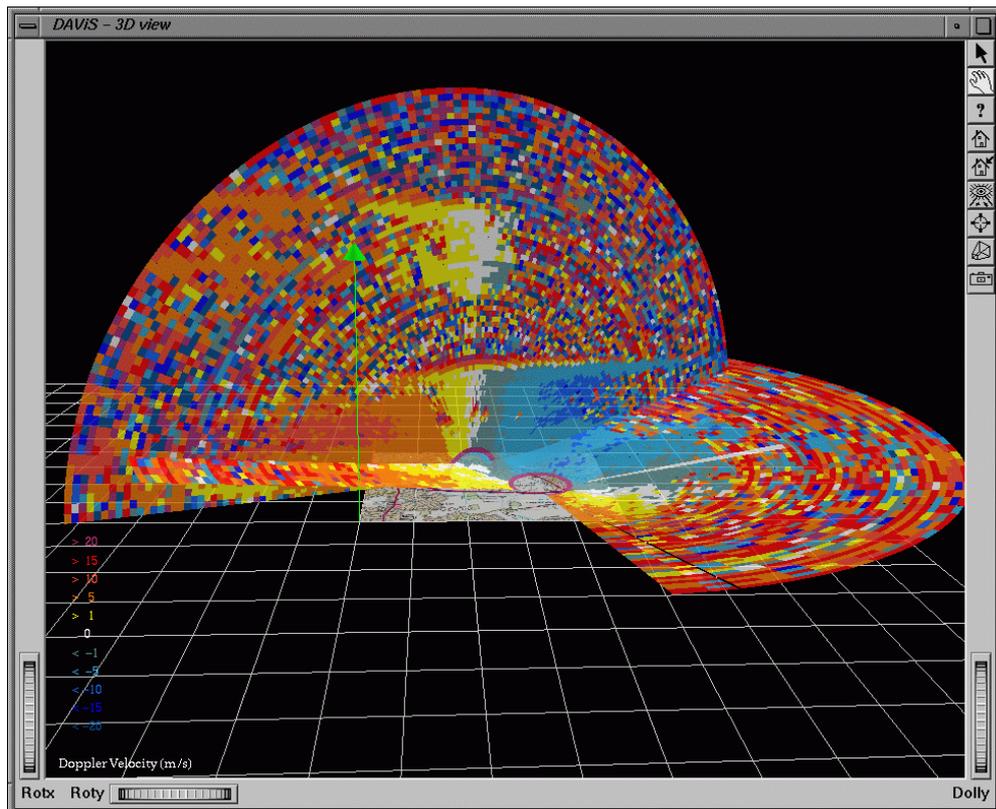
Figure 5.10 A 3D display of radial velocity measurements of by the QinetiQ lidar (RHI) and by the Salford lidar (PPI) at Northolt on the 23rd of July at 11:17.
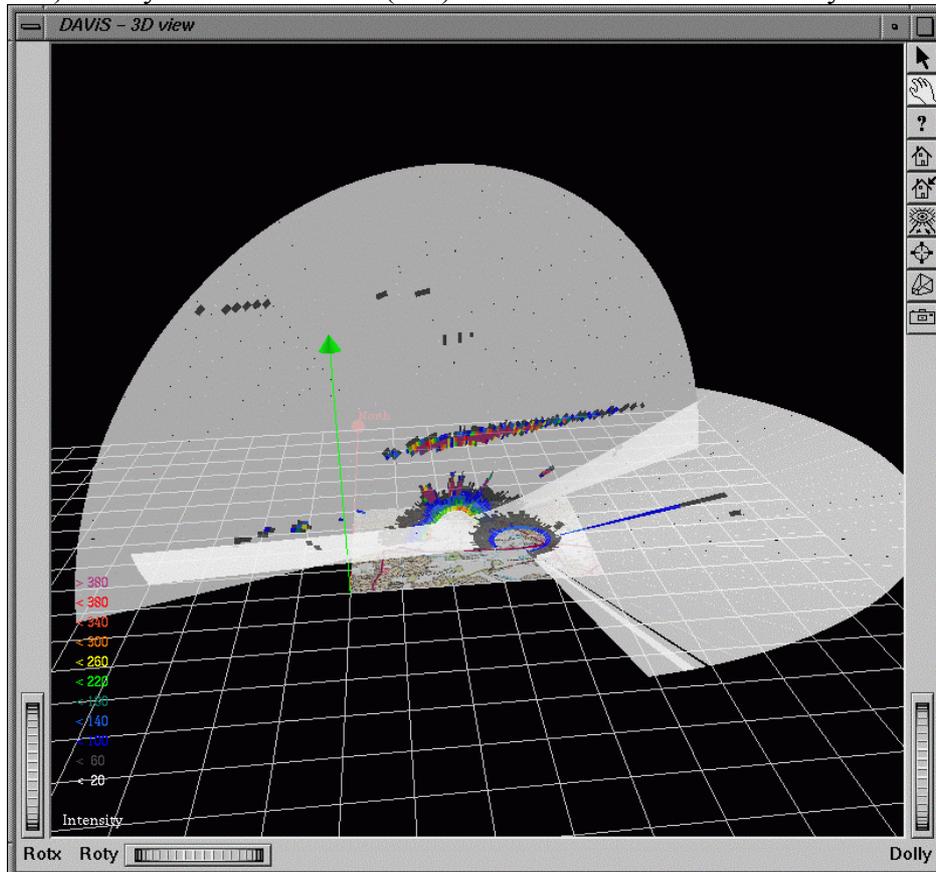
Figure 5.11 A 3D display of range-corrected intensity measurements of the QinetiQ lidar (RHI) and the Salford lidar (PPI) at Northolt on the 23rd of July at 11:17.

QinetiQ RHI + QinetiQ RHI

The ability of the QinetiQ lidar to measure RHI over a full 180° elevation is presented in the following case in which two RHI plots by the QinetiQ lidar are combined. Both measurements were made on the 22nd July at 17:15 and 17:29 respectively.

The visualisation of the intensity in figure 5.12 shows how both lidars record the same layer height, except to the south east where the layer seems to collapse in height (see right side of figure 5.12). The Doppler velocity pictures (figure 5.13) shows clearly how on one RHI (east-west) the values change from negative (blue, east) to positive (yellow-red, west), while the other RHI (north-south) shows values low in velocity near to zero (white).

QinetiQ RHI + QinetiQ PPI

The example considered is the PPI at 16:31 and the RHI at 16:47 on the 9th of July recorded by the QinetiQ lidar. The PPI was recorded at an elevation of 40 degrees while the RHI was orientated on the east to west axis.

The high elevation angle of the PPI was rarely used during the experiment, and shows combined with the RHI the boundary layer of the lower atmosphere. The intensity display is shown in figure 5.14. The height of the boundary layer is not clearly visible from the RHI but is from the PPI, where a circle of higher intensity is clearly visible.

The velocity display in figure 5.14 shows that the RHI and PPI generally agree in the direction of the velocities.

VAD data + Model output

The main aim of the project is to compare output from forecast models and retrieved information from lidar data to see if the model can be improved.

A good opportunity to compare these types of data was on the 23rd of July around lunch time, where in short period of time (30 minutes) data is available from the model and PPI scans by both lidars.

Figure 5.16 shows the resulting 3D display viewing from west to east. Three columns of wind vectors can be seen. The two columns of green vectors show the results of VAD analysis on the two PPIs measured by the lidars. The front green column was measured by the QinetiQ lidar while the back column was measured by the Salford lidar. The middle column (red) is retrieved from the model output that was provided by the Met Office.

While the wind information retrieved from the VADs agree quite well with each other, the wind information from the model only agrees with them at heights beyond 1000 metres. Nearer to the ground the model shows a wind flow which differs by about 45 degree in easterly direction.
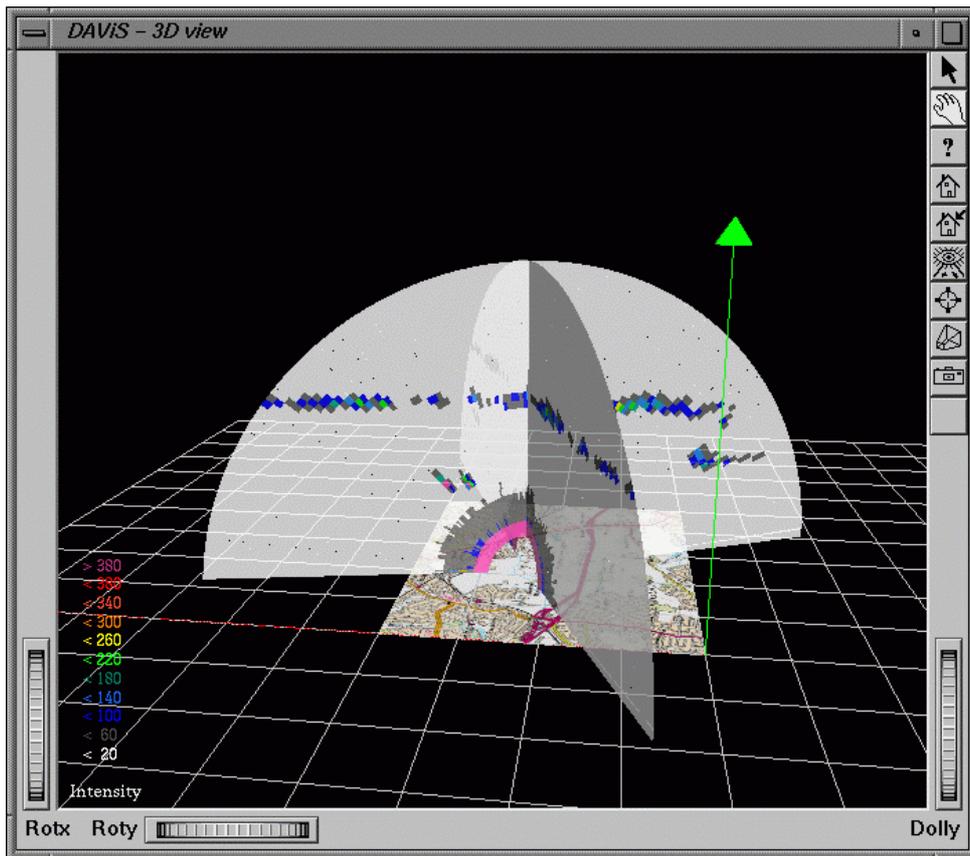
Figure 5.12 A 3D display of two RHIs, showing range-corrected intensity. This was measured by the QinetiQ lidar at Northolt on the 22nd of July at 17:15 and 17:29.
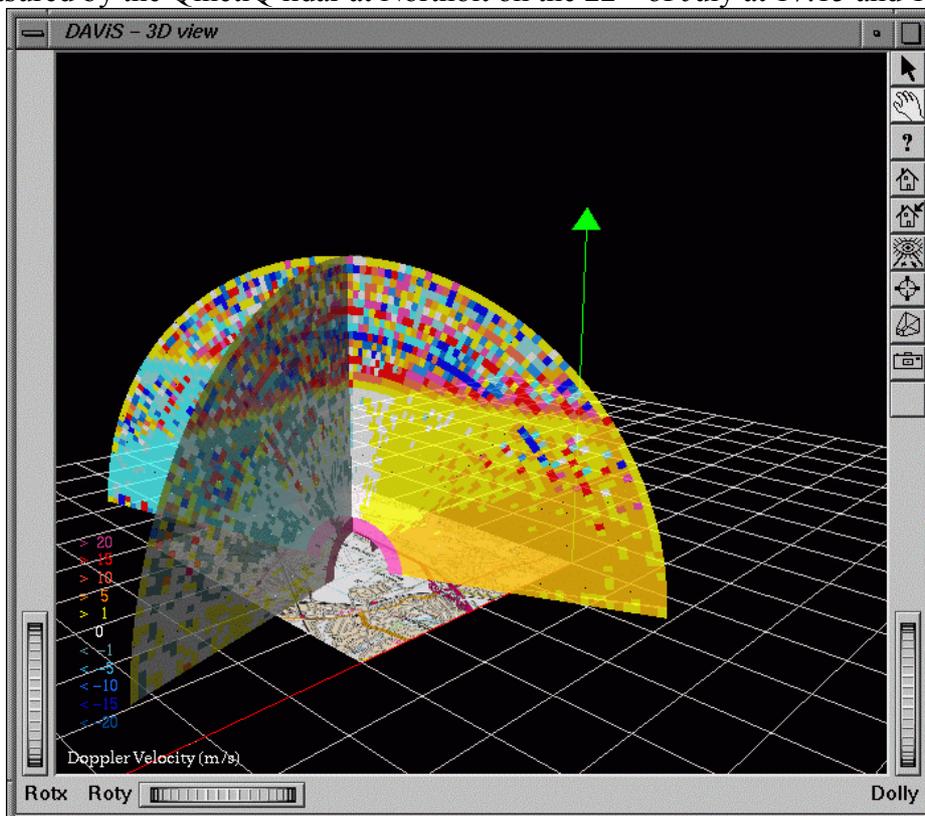
Figure 5.13 Another plot of two RHIs combined. This is the same data as in figure 5.8, but this time the radial Doppler velocity.
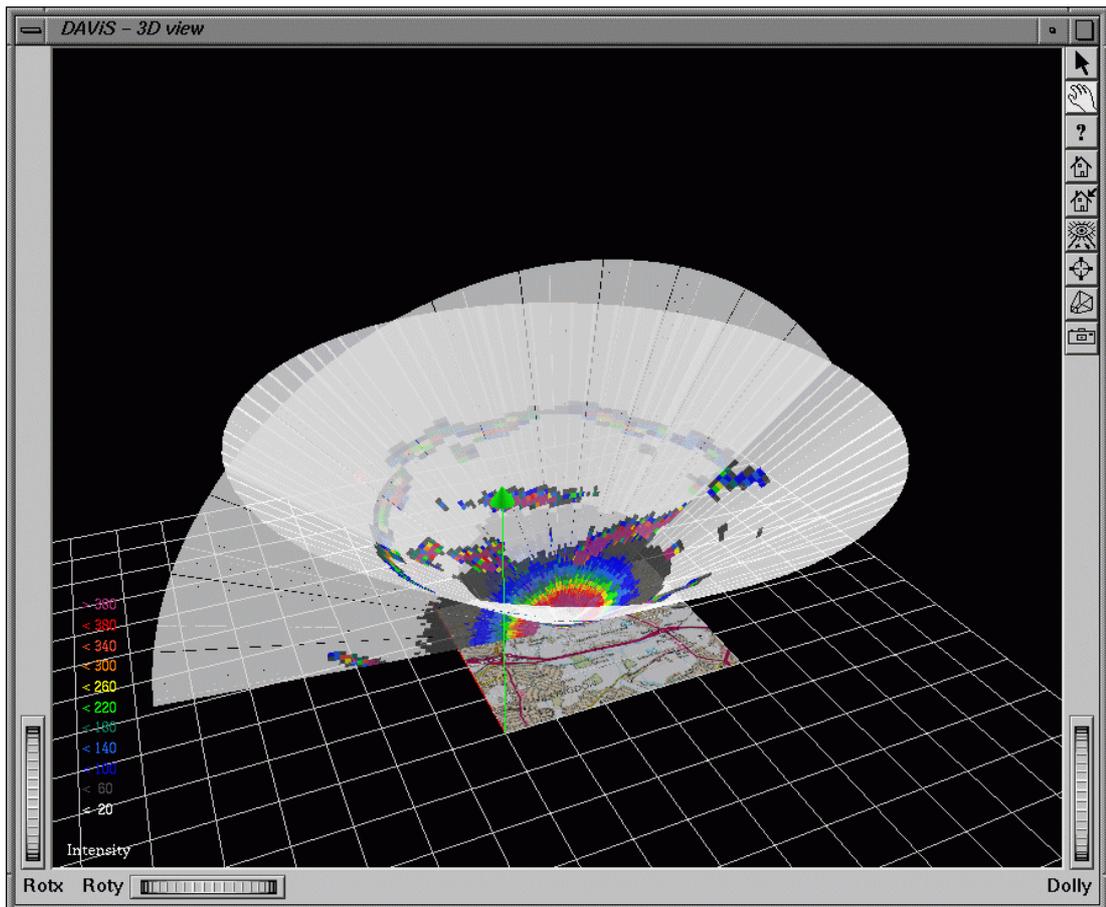
Figure 5.14 Intensity display of the QinetiQ lidar data measured on the 9th of July at 16:31 (PPI) and at 16:47 (PPI).
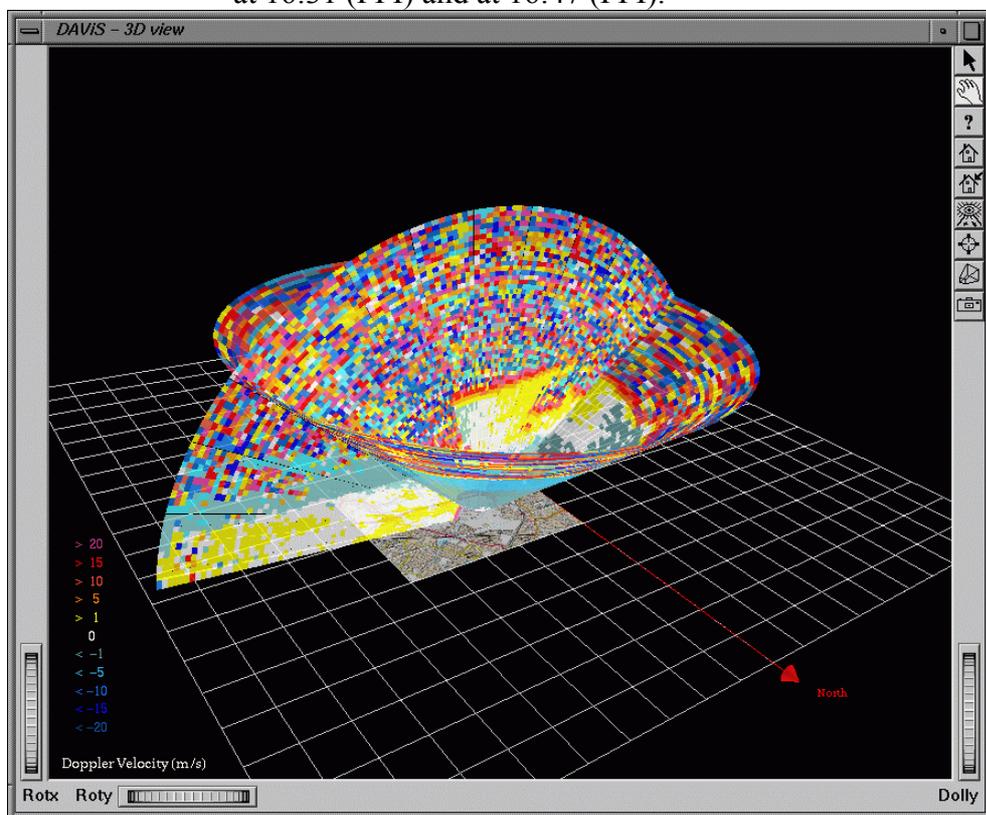
Figure 5.15 Doppler velocity plot of the same case as in Figure 5.12.
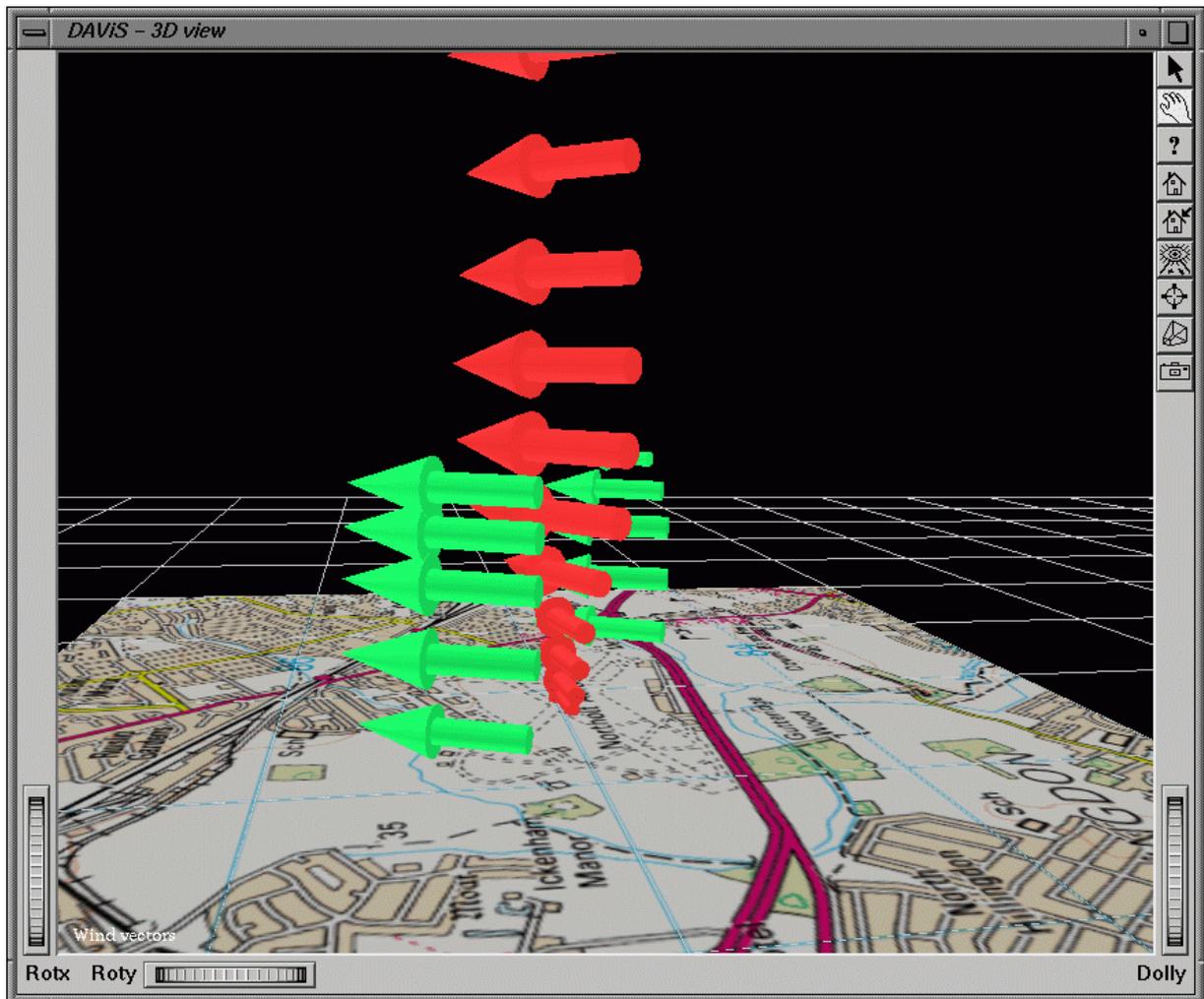
Figure 5.16 Comparison of wind information retrieved from the model (red) and from lidar data through VADs (green) on the 23rd of July. The front green column is retrieved from data from the QinetiQ lidar (12:25), while the second green (back) column is retrieved from data measured by the Salford lidar (12:28). The model data as extracted on the eve before for 12:00.

5.3 Conclusions of the visualisation work

The work undertaken by the University of Essex group has brought these conclusions:

- If the data were recorded automatically the display and analysis of lidar data can be done in real-time.
- A three-dimensional display can give vital information to the observer how data from the two lidars relate to each other in space.
- Retrieved wind information can be also easily added to a three-dimensional display.
- Stereo graphics can improve the visual impact to the user. It enables the user to obtain a clearer picture of the scene.
- The visualisation and analysis can be combined in one software package, which, combined with a fixed common data format, makes it easy to reproduce and compare results.
- The scan strategies most interesting for the visualisation are 180 degree RHIs and PPIs at higher elevation angles. These show best the structure of the boundary layer.

6 COMPARISON OF LIDAR OBSERVATIONS AND DERIVED PARAMETERS TO NWP PREDICTIONS

6.1 Factors that impact on relating Lidar Data to Dispersion Model Parameters

The parameters used in dispersion models such as NAME were tabulated and compared against the possible parameters calculated from lidar data. The key issue was how to use data from a single or a dual lidar experiment in order to calculate dispersion parameters. Several issues arose:

1. The lidar are volume average measurements. The dimensions of each volume are defined by the diameter of the beam (0.5 m at 9 km) and the range gate length (112 m).
2. Turbulence data such as a velocity variance are conventionally obtained on a sonic anemometer with three orthogonal components resolved directly at 4-20 Hz. The sonic anemometer is run for a period, means and fluctuations from the mean calculated; this requires measurements for a sustained period (say 10 minutes or more). The lidar yields a radial component along the beam at a rate of 0.2 Hz. Mean wind speed and direction are calculated from an area average azimuth (VAD) scan [27]. The VAD scan takes approximately 6 minutes.
Dual lidar operation enables the measurement of two components of the wind flow simultaneously. From the two radial wind measurements, two orthogonal wind components can be calculated. It is possible to obtain the third orthogonal component of the flow through use of the continuity equation.

Bozier et al 2004 [13] addressed the issue of different sampling rates and volumes to show that average wind profiles from sonic and lidar data compare well.

6.2 Examples of vertical profile comparisons

The mean wind speed and direction can be obtained with lidar using a VAD or azimuth scan [27]. The lidar is scanned at a particular elevation angle describing an inverted cone shape. Data at a particular range gate is then plotted and a sine curve is fitted. The phase of the curve gives the direction of the maximum wind speed and the magnitude of the curve gives the wind speed. The wind speed and direction obtained are therefore area averaged over the area described by the scan at that particular range. Figure 6.3.1 and 6.3.3 show the mean wind speed and direction from a series of VADs from 07:45 UTC to 08:48 UTC on the 16th July 2003. This data was taken as a thunderstorm was approaching and the wind field is seen to change considerably over this time period. Figures 6.3.2 and 6.3.4 show NWP model wind speed and direction profiles for 06:00 UTC and 09:00 UTC.
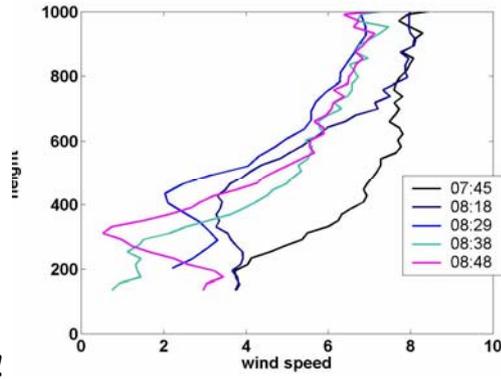
Error!

Figure 6.3.1 Mean wind speed and direction from lidar observation at 07:45
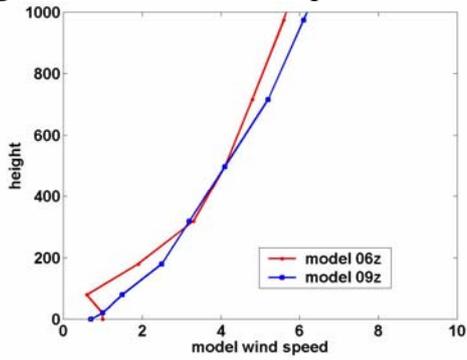
Figure 6.3.2 Mean wind speed and direction from NWP at 06:00
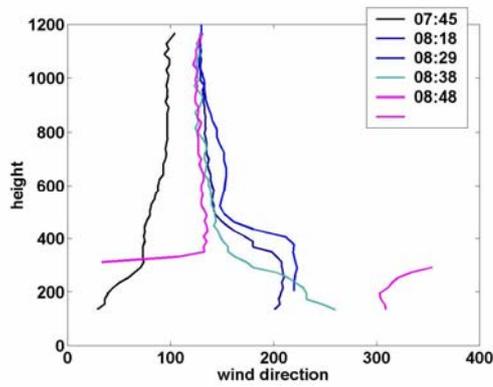
Figure 6.3.3 Mean wind speed and direction from lidar observation at 08:48

43
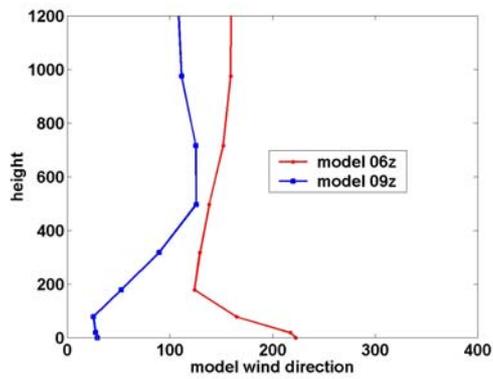
Figure 6.3.4 Mean wind speed and direction from lidar observation at 09:00

In this case the model profiles are comparable to the lidar data and correlate fairly well.

6.4 Turbulence Parameters

The aim of the dual Doppler lidar trials was to use the two lidars in a co-ordinated manner to enable the measurement of two of the velocity components independently. To this aim a series of 'stare' data were taken with the lidars looking in the plane defined by the line joining the two lidars. The set up is shown in figure 6.4.1.
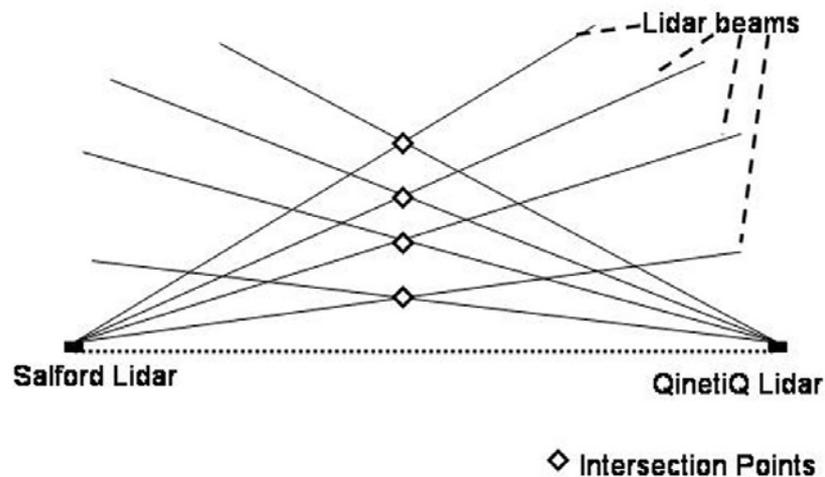
Figure 6.4.1 Schematic of dual Doppler Lidar scan

The data was taken from 11:30 to 12:30 UTC on the 23rd July 2003. The mean wind direction was nearly perpendicular to the plane containing the two lidars. The radial wind measured by the two lidars thus has a horizontal, and vertical, w, component. The data from the two beams are transposed to produce time series of horizontal and vertical winds. Since the two lidar beams are along the same horizontal axis no measure of the wind direction change with height can be made using this method. Only the horizontal (along the axis of the beam) and the vertical components can be calculated. Appendix 2 explains how wind data are derived from dual lidar modus operandi.

Mean wind speed and direction data taken from a single VAD of the QinetiQ lidar data is shown in table 6.1. The lidar data was taken from 12:25 – 12:32 UTC and is compared to NAME model data from 12:00 UTC. (The wind data from NAME is output at hourly intervals).

Height (m)	Mean Wind Speed (ms-1)		Mean Wind Direction (deg from N)	
	Lidar	model	lidar	model
100		6.7		186
200	8.94	7.4	208	190
400	9.72	8.7	207	199
709	9.85	12.0	210	219

Table 6.1 Comparison of wind speeds and bearing.

Table 6.2 compares mean winds and standard deviation of the winds as derived from the dual lidar data from the two lidar systems between 11:30 and 12:30 UTC. The horizontal winds are measured along the axis of the lidar beams i.e. at an angle of 118 degrees from North. The lidar beam axis is thus approximately 70 degrees to the mean wind. The model data in table 6.3 is all data gathered at a height of 10 m. Since the wind speed and direction can change considerably in the near surface layer there is no reason to expect there to be a good correlation between mean wind speed data at 10 m and in the boundary layer above.

Height (m)	Mean horizontal wind in direction of the lidar axis (m s^{-1})		Mean vertical wind, $\overline{w}$ (m s^{-1})		Standard deviation of wind in direction of the lidar axis (m s^{-1})		Standard deviation of w (m s^{-1})		Momentum flux (10^{-2} m^2 s^{-2})	
	lidar	model	Lidar	model	lidar	Model	lidar	model	lidar	model
100	-0.32	1.73	1.9	0.01	0.50	1.18	3.4	0.96	-0.28	-0.3
200	1.24		0.04		0.59		1.45		0.22	
400	0.47		-0.15		0.59		1.78		-0.17	
709	0.26		-0.72		1.24		1.66		-0.74	

Table 6.2 Comparison of mean winds and standard deviation of the winds.

Using the derived horizontal and vertical winds at the lowest lidar level (100 m) values for kinetic energy dissipation rate and Lagrangian time scale have been calculated. These are shown compared to NAME dispersion model values in the table below. The NAME parameters are again shown for a height of 10 m unless otherwise stated. In this comparison the boundary layer heights compare very well.

	Lidar	Model
Boundary Layer Height (m)	880	850
Kinetic energy dissipation rate (10^{-3} m^2 s^{-3})	20.5 (@100m)	7.8 (@100 m)
Lagrangian time scale for horizontal wind, (sec)	350	233
Lagrangian time scale for vertical wind, (sec)	300	150
Convective velocity scale, w_* (m^2 s^{-2})	5.38 @ 100 m 2.29 @ 200 m 2.81 @ 400 m 2.62 @ 709 m	1.51

Table 6.3 Comparison of kinetic energy dissipation rate and Lagrangian time scale

6.5 Observation of Boundary Layer Depth
The atmospheric boundary layer is a layer near the surface, exchanging heat, momentum and moisture between the earth and atmosphere. Pollutants are dispersed in this layer. Boundary layer depth or height (of the top of this layer) depends on the

wind speed, the vertical gradient of temperature, and the presence of either strong convection or surface cooling. It varies from below 100m to a few km. It is often greatest in late afternoon, say 1km, and falls in rural areas to about 100m in the evening as the ground cools. At night in urban areas, it has a larger value than the rural case. It follows a diurnal cycle.

Since pollutants can be dispersed vertically, we also speak of the mixing layer. The mixing depth represents the height reached by pollutants after release from sources at ground-level. Upward dispersion is eventually limited by an inversion above the mixing layer. Most dispersion models require an estimate of the mixing depth or boundary layer depth/height so that any effective limit on vertical spread can be modelled. The effect is most important when the depth is shallow, when low lying plumes may be trapped near to the ground, or elevated plumes might be unable to reach the ground. The depth may be input to the model, or calculated by routines within the model.

Since the boundary layer depth or inversion height effectively set an upper limit to the vertical mixing of pollutants, they are of great practical importance for dispersion models. In earlier ISB52 reports [1,4,5] the boundary layer depth was identified as the highest priority parameter to be determined during the lidar field trials, followed by the wind profile, urban-rural differences, and values of the various boundary layer parameters.

Other workers have measured boundary layer depths by several means, such as the height where turbulence diminishes, or heat flux diminishes, or there is a marked discontinuity in profiles of wind/temperature/moisture, or the height of strong back-returns in acoustic sounding, or from lidar using the aerosol back-scatter signal. However the top of the boundary layer is not easily subject to a unique definition; different methods may yield different values. In this study we are fortunate that the pulsed Doppler lidar can be used to monitor simultaneously both the turbulent fluctuations with height, and the aerosol back-scatter intensity. We may thus compare the decay in turbulent motions with the decay in (from aerosol scatters) signal intensity (from SNR). As shown in ISB52 MS6 [7] it was found that the decay in signal to noise ratio (SNR), which is strongly dependent upon availability of the aerosol particulates acting as centres for scattering, can be employed to detect the top of the boundary layer. This is because we assume the aerosol is largely concentrated in the boundary layer, and there is much less back scatter above the layer.

6.5.1 Malvern Winter Trial
The upper two graphs of figure 6.5.1 were shown in an ISB-52 technical working paper [3]. They are shown again here in conjunction with the potential temperature graph below in order to enable the issue of defining the boundary layer depth to be discussed. The parameter of interest here is the height in the lower atmosphere up to which any sources at or near the surface will be mixed. This may correlate with various features of the lidar data but the aim is to find the most robust technique for assessing this height both in the daytime and at night. Since any sources will be confined to this layer it is important to try to obtain the most representative height.

The lidar data from which the bearing, wind speed and backscatter values were derived was acquired between 18:50 and 19:03 of the 18th March 03. The potential

temperature graph shows data from the NAME model for 18:00 of the same day. The lidar data shows a reduction in the backscatter at approximately the same height as the wind field exhibits a change of direction and a change in speed. This height is about 750m. The potential temperature plot shows a change in gradient at a height of about 450m.
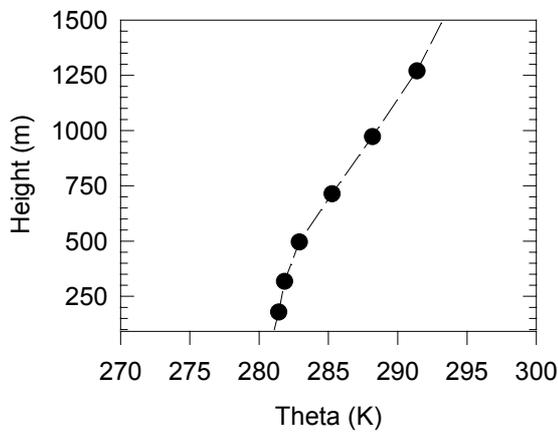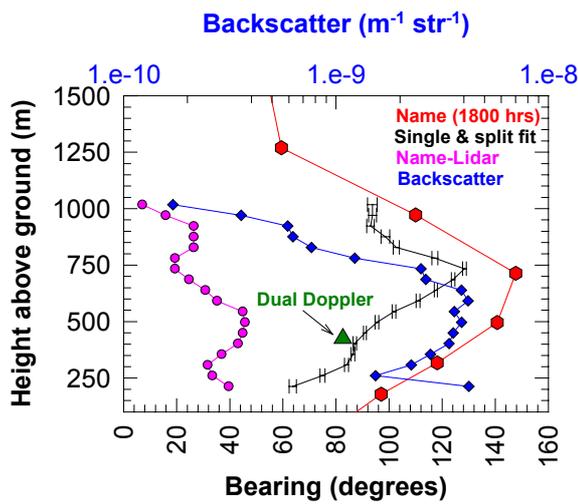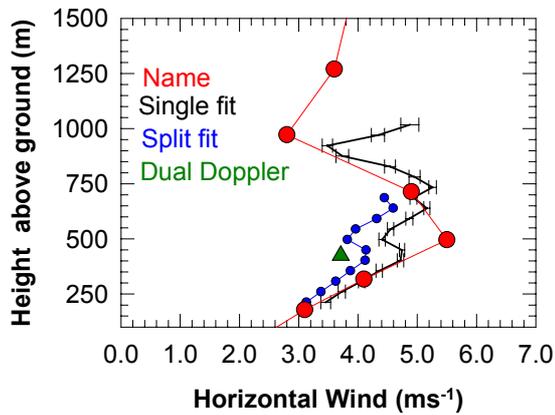
Figure 6.5.1 Top panel: The wind speed versus height as derived using two different VAD analyses (blue, black), dual Doppler (green) and the NAME model (red). Middle panel: The direction of the wind (VAD (black), dual Doppler (green) and NAME (red)) and the backscatter coefficient (blue) versus height. Bottom panel: The NAME potential temperature versus height.

The discrepancy in the bearing of the wind flow between model and observation is now ascribed to the impact of the close proximity of the Malvern Hills to the trial site. The nearest NAME grid point was several miles away and so did not account correctly for the local Malvern topology.

6.5.2 Example from the summer trial

As noted above the Boundary layer height can be inferred from lidar backscatter data. In high aerosol conditions and high pressure situations the boundary layer is usually capped by a strong inversion layer. Any aerosols within the boundary layer are effectively trapped. In such cases the height of the boundary layer can be inferred from lidar backscatter intensity data. Figure 6.4.2 shows data from 16:00 UTC on the 9th July 2003 probing the rural environment. The signal-to-noise (SNR) is plotted against height for the lidar data. A sudden decrease in the SNR is seen at approximately 1250 m above ground level.
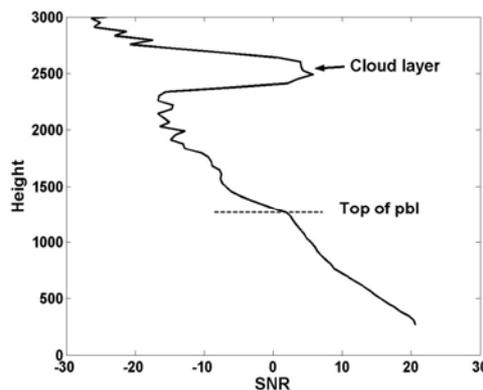
Figure 6.5.2 Lidar back scatter data from 16:00 UTC on the 9th July 2003

The sudden drop in SNR indicates the top of the boundary layer.
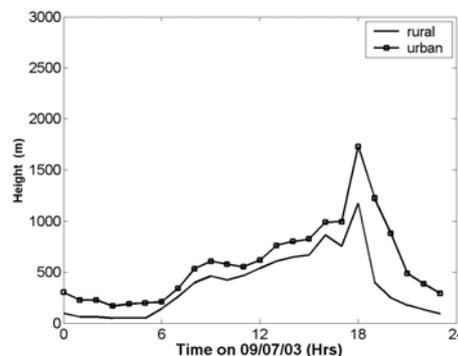
Figure 6.5.3 Boundary layer height over a 24 hour period from the ADMS dispersion model run under rural and urban conditions for the 9th July 2003.

48

Figure 6.5.3 shows model boundary layer height for urban and rural NWP model configurations. For the data on this day the boundary layer has its maximum height at 16:00 UTC. From comparison of the figures 6.5.2 and 6.5.3 it is concluded that the predicted boundary layer height is significantly lower than that observed by the lidar.

6.5.3 Horizontal and vertical variations of PBL

In this section lidar observations of the fine detail of the spatial variations of the top of the planetary boundary layer across the rural urban interface and the shape of the top of the PBL are presented.

NAME is quite sensitive to the depth of the PBL. At present there is effectively no adjustment of the PBL in the model across the rural-urban interface. The lidar data have shown large variations (up to 1000m) across this interface on some occasions. Analysis of the synoptic situations / stability has revealed when these variations are largest.

At present the NAME model assumes that the top of the convective PBL remains uniform. The lidar data show that this is not necessarily the case, and the top may exhibit undulations. It is recommended that dispersion models should be modified to allow a non-uniform boundary top and rural to urban transition region. How this might be approached depends upon the grid resolution of the model data; as the grid approaches 1 km or less, such non-uniformity will be more explicitly represented.
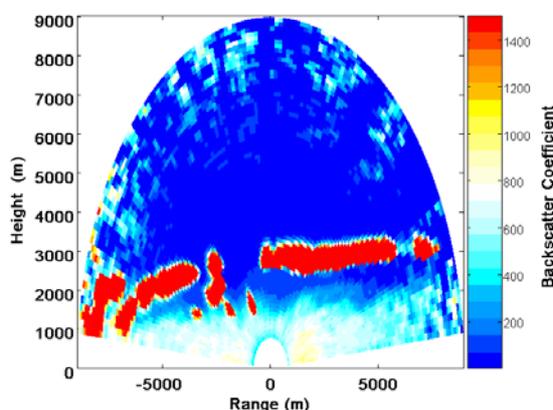
Figure 6.5.4. Elevation scan showing backscatter coefficient against height at 14:22 UTC on 9th July 2003. The scan has been carried out in an east – west plane. (i.e. positive ranges are due east of the lidar site).
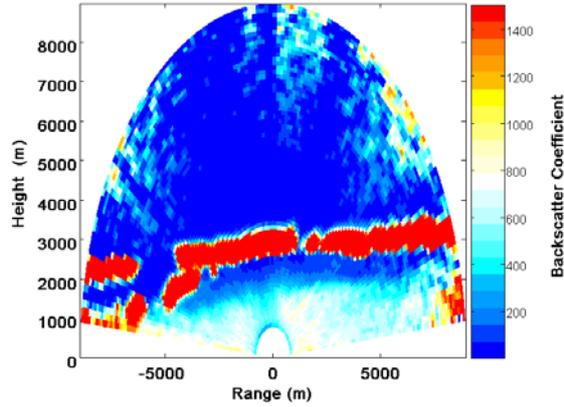
Figure 6.5.5 As figure 6.5.4, except at 14:35.
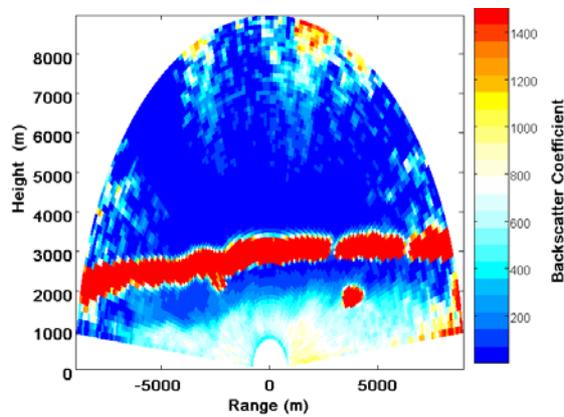
Figure 6.5.6 As figure 6.5.5, except at 15:01 UTC.
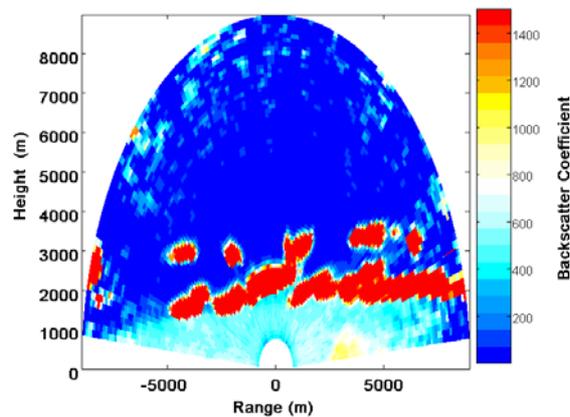
Figure 6.5.7 As figure 6.5.6, except at 16:50 UTC.

The series of figure 6.4.4 to 6.4.7 show 180 degree elevation scans from 14:22 to 16:50 UTC on the 9th July 2003. The figures show the backscatter coefficient plotted

against height. The red bands show very high backscatter values denoting cloud bands.

The scans have been taken in an east west direction, so that positive ranges denote distance east of the lidar position. The figures show there is a marked increase in the height of the cloud base above the 'urban' surface. In figure 5c an isolated cloud can however be seen lower in the atmosphere. An elevation scan, figure 6, shows that later in the day the lower cloud layer is more continuous.

It can also be seen in figures 6.5.4 to 6.5.7 that the pale blue contours of backscatter coefficient are higher over the 'urban' surface than over the more 'rural' surface. Estimation of the height of the mixing layer was carried out using the method of Mok and Rudowicz [28] and showed that at approximately 15:30 UTC on the 9th July there was a difference of approximately 450m between the height over the 'urban' surface compared to the 'rural' surface. The distance between these two points was approximately 10km. This is considerably greater than the 200m height difference at 15:30 UTC as suggested by the different urban and rural ADMS model runs shown in figure 6.5.3.

6.5.4 'Stand and stare' observation.

It is also possible with lidar to observe the temporal variation across the PBL. This is achieved using a stand and stare observation, in which the lidar beam is held stationary and the wind flows through the line of observation. In this scan temporal variations are observed at a fixed location in the atmosphere.
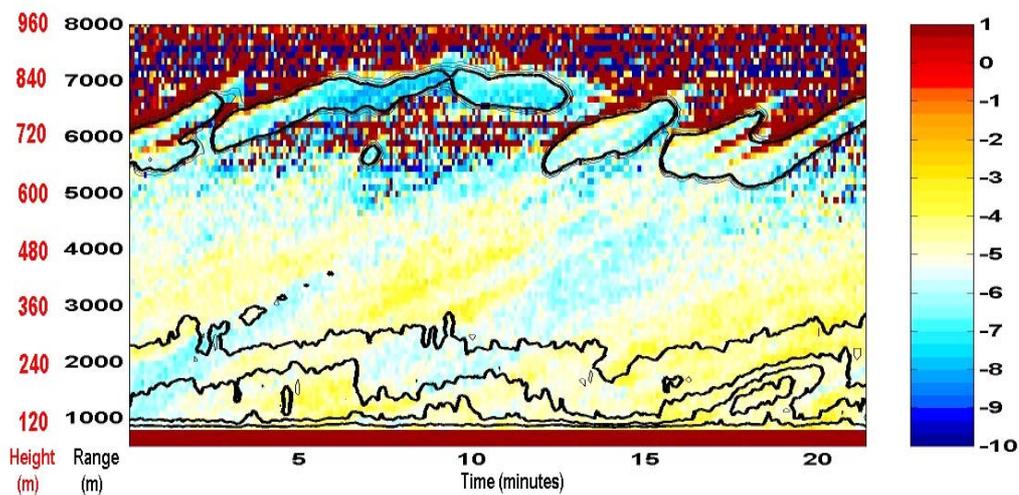
Figure 6.5.8 Result of a stand and stare observation

Figure 6.5.8 shows the results of a fixed stand and stare. This scan type enables a time dependent view of the flow field to be built up as the prevailing flow moves through the stationary inclined beam and convective cells rise through it. Colour coded radial velocity is plotted on successive inclined lines like a time series, with time on the horizontal axis and height on the vertical. Contours of intensity, or derived aerosol concentration, have been added.

51

At present the NAME model assumes that the top of the convective PBL remains flat. The lidar data shows that this is not the case, and the top often undulates. It is recommended that the NAME code should be modified to represent this temporal variability in the PBL height.

6.5.6 Relating Lidar Data to the Rural-Urban Transition

In measuring urban meteorology, long data runs are usually very hard to obtain. With complex and expensive lidar equipment, it is necessary to plan for a restricted number of trials. A striking feature of remote sensing is its ability to survey over significant distances. Here the maximum range could be up to 10-12 km, or down to 6 km, according to conditions. Having two lidars meant other scanning patterns designed to look at rural and urban conditions simultaneously could be used. Thus when running without beam intersection:

1. The beams can point in opposite directions, say into the approach flow over the rural south west, and with the urban flow to the north east.
2. The beams can be set orthogonal to each other, so one may be along the mean wind direction, the other cross wind.

Whilst this apparently negates a key advantage of having two similar instruments to measure unambiguously the flow field at a single point, it is apparent that observing over both the rural and urban surfaces simultaneously is an invaluable methodology for studying the rural-urban transition, and merits discussing at length. The ability to scan the beams and reach out several km is a clear advantage over fixed sonic anemometer measurements.

6.6 Comparison of lidar observations to dispersion model predictions.

The fourth objective was to show through comparisons of the data to forecasts any limitations in the underpinning assumptions of the current dispersion models and where the dispersion models could be improved to give a more accurate forecasting ability.

The full complement of data that is available from this field trial is extensive and only a sample was discussed in the ISB52 reports. Further analysis of the data was presented in papers to the open literature and presentations at conferences[29-32].

For the comparison the parameters that might be measurable either by single or by dual lidar operation and used in dispersion models such as NAME were tabulated and compared against the possible parameters calculated from lidar data, see tables 6.1, 6.2 and 6.3 of this document and references 1,5,7,11. Examples of this include using the fixed lidar beam values for the kinetic energy dissipation rate and integral length scale which can be derived from the power spectra [13,17]. The integral timescale can be estimated from the velocity lag autocorrelation curve [21]. From using a vertically pointing fixed beam the convective velocity scaling can be estimated [15]. From this an estimate of the heat flux, w't' and sensible heat flux at the surface, H, can then be calculated [17].

The key comparisons made between lidar data and model predictions were for:

Examples of vertical profile comparisons.
Turbulence Parameters.
Boundary Layer Depth.

Horizontal and vertical variations of PBL.

The comparison of lidar data to prediction has allowed time series to be developed. One such comparison for boundary layer height is shown below. This observation was made between 13:18-20:26 on 22/07/03 with the lidar beams crossing at a point over South Ruislip.
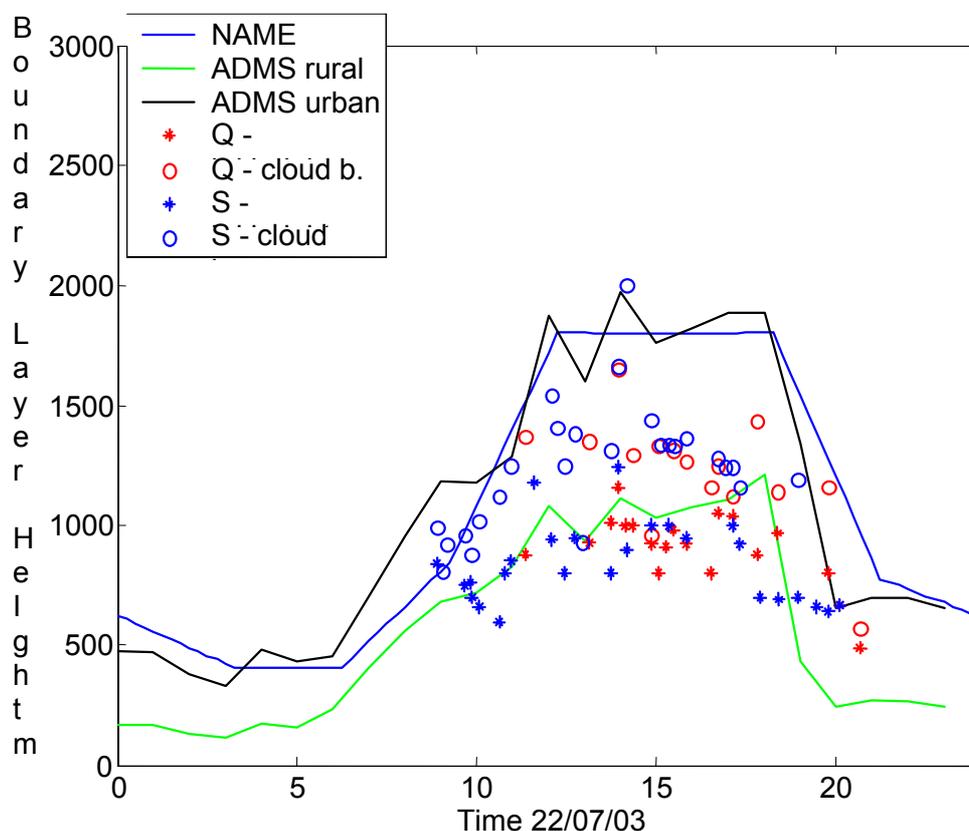
Figure 6.6.1 Example of typical results from the comparison of lidar data to dispersion model prediction.

The comparison of derived meteorological parameters between the lidar and models has shown some very interesting features. The calculation of the boundary layer height parameter carried out by both the NAME and ADMS models, as shown in figure 6.6.1, appears to show that the models overestimate the boundary layer height under urban conditions. This could be either a result of wrong 'urban' surface conditions or due to the sensitivity of the parameterisations within the model. However what this means in real terms is that urban pollution concentrations, and consequently the likely health implications, are being underestimated using these models.

Although this effect was seen for most of the days of the field trial, it was found that comparisons between the lidar and model data were highly dependent upon the prevailing conditions the variations between data sets changed. Further observational work under differing atmospheric conditions would be required before these variations could be fully understood and quantified.

7 SUMMARY

7.1 Review of aims of the ISB-52 project

Local air quality management uses dispersion models to forecast poor air quality. Whilst there are a number of models in use they all consider similar parameters principally, the mixing height, stability, and turbulence. Measurements of these parameters over urban areas are not routinely available. This is because to ensure good exposure, synoptic stations are often located at airports. When data is collected from instruments placed upon city centre buildings, careful evaluation is necessary to mitigate any local effects. Validation of urban models is thus hampered by a lack of observational data sets. Given these limitations the ISB-52 project has been investigating the application of remote sensing using scanning pulsed Doppler lidar for urban dispersion studies[1-11].

The aim of the ISB-52 project was to develop an enhanced ability to forecast periods of poor air quality from dispersion models. This was to be achieved by gaining a better understanding of the dynamics of wind flow for the urban environment rather than to feed the gathered data directly into the forecasts. In particular the project set out to:

- Use lidar data to measure dispersion model parameters used in meteorological pre-processing.
- Evaluate NAME/Unified Model, ADMS and other models using the lidar results.
- Investigate rural-urban differences.

It is recognised that it is beyond the scope of this project to quantify the likely improvements to the accuracy of future forecasting of pollution dispersal by the incorporation of new knowledge derived from the lidar observations. However, it is well known that all models contain assumptions developed for the rural environment that are invalid to describe conditions within the urban environment.

7.2 Scientific and technical progress

The programme of work contained the following main stages:

7.2.1 Develop the lidar technology to allow Dual Doppler observations across a rural urban interface.

Upgrade the lidar systems with more powerful TEA lasers, new data processing software, better SNR [2,3,20].

7.2.2 Relate lidar data to dispersion model parameters to design field trials.

The first report of ISB-52 [1] detailed the parameters within the most common dispersion models. Subsequently [5] identified the key parameters and consequently the required scan patterns needed for the validation of the dispersion models. The conclusion was that the measurement of the height of the top of the planetary boundary layer was of top priority. Profiles of wind speed, wind direction and turbulence were also required. To achieve a set of observations representative of the statistics of pollution dispersal phenomena it was also recommended to dwell along one line of sight for at least ten minutes.

The primary aim of the trial was to ascertain how lidar data could be processed to yield products that could be used to improve the forecasting of urban air quality by dispersion models. A list was therefore drawn up to compare parameters that were used within the dispersion models to those that could be obtained from a dual Doppler lidar trial. This table appears in section 3.

So far as the Project Team is aware, no group has previously tried to compile such a list of dispersion model variables that are in principle amenable to lidar observation prior to a measurement campaign. In the remainder of this report the Project Team compares the parameters from our lidar results with the mesoscale/NAME data sets.

From this work a number of scan patterns were devised to observe unambiguously specific dispersion model parameters under different ambient conditions. That each of these scan patterns was optimum for observing a specific phenomena implies that the scan pattern would be limited for other observations. Recognising these limitations was a key lesson that was learnt during the Project, as were the strategies adopted to ameliorate these limitations during the trials.

This Project has shown that there was no single scan pattern that can derive all the dispersion model parameters. These specific scan patterns did not involve the PPI scans over the large volumes of space necessary for the 3D flow visualisation displays. So whilst the developed code has an ability to display such data, little was gathered.

It was also found that the limits on usable range combined with the relative slow scan speed of a lidar system became significant design constraints when planning the field scanning patterns.

7.2.3   Deploy twin lidars to make observations

The two lidar systems were deployed simultaneously to measure multiple components of the flow field. The project investigated the suitability of a large number of potential trials sites before settling on West London as the most 'typical' and RAF Northolt as the optimum deployment site [8]. The first winter trial was conducted around QinetiQ, Malvern because of events in the Gulf at that time [6,7]. The second summer trial was at RAF Northolt [8].

The successful deployment of the two lidars demonstrated the reliability of the instrumentation and proved the dual lidar concept.

7.2.4   Compare lidar observations to dispersion model predictions

The fourth objective was to show by comparisons of data to forecasts, any limitations in the underpinning assumptions of the current dispersion models and where the dispersion models could be improved to give a more accurate forecasting ability.

The full complement of data that is available from this field trial is extensive and only a sample was discussed in the ISB52 reports. Further analysis of the data was presented in papers to the open literature and at conference presentations [29-32].

For the comparison, the potentially measurable parameters, either by single or by dual lidar operation, and which were used in dispersion models such as NAME were

tabulated and compared against the possible parameters calculated from lidar data. Examples of this include using the fixed lidar beam values for the kinetic energy dissipation rate and integral length scale which can be derived from the power spectra. The integral time-scale can be estimated from the velocity lag auto-correlation curve . From using a vertically pointing fixed beam the convective velocity scaling can be estimated. From this an estimate of the heat flux, w't' and sensible heat flux at the surface, H, can then be calculated.

The key comparisons made between lidar data and model predictions were for:

> Examples of vertical profile comparisons.
> Turbulence Parameters.
> Boundary Layer Depth.
> Horizontal and vertical variations of PBL.

A summary of the data gathered and derived parameters was given in Table 3.1.

The comparison of lidar data to prediction has allowed time series to be developed. One such comparison for boundary layer height is shown below. This observation was made between 13:18-20:26 on 22/07/03 with the lidar beams crossing at a point over South Ruislip.

The comparison of derived meteorological parameters between lidar and modelling has shown some very interesting features. The calculation of the boundary layer height parameter carried out by both the NAME and ADMS models, as depicted in figure 6.61, appears to show that the models overestimate the boundary layer height under urban conditions. This could be either a result of wrong 'urban' surface conditions or could be due to the sensitivity of the parameterisations within the model. However what this means in real terms is that urban pollution concentrations, and consequently the likely health implications, are being underestimated using these models.

Although this effect was seen for most days of the field trial, it was found that comparisons between the lidar and the model data were highly dependent upon the prevailing conditions and the variations between data sets. Further observational work under differing atmospheric conditions would be required before these variations could be fully understood and quantified.

7.2.5   Develop a software suite to visualise the dual lidar data in 3D
A data visualisation suite was developed (DAViS) to display the lidar data in other formats [9,10]. Images are a very powerful tool for interpreting atmospheric dispersion phenomena. For example, one of these formats showing the evolution of the PBL around Northolt is of significant merit in understanding the fine detail of the boundary layer turbulence over the rural urban interface.

7.3 Implications of the project
Unique observational data has been gathered of pertinent physical phenomena observed in-situ. From this, important new results have been obtained for deriving the mixing height from the lidar data and associated media displays.

A key point of the Project was that these images also instigated discussions into how to define the PBL. At present the NAME model assumes that the top of the convective PBL remains flat. The gathered lidar data shows that this is not the case, and the top often undulates [11]. It is recommended that the NAME code should be modified to allow variability in the PBL height.

NAME is quite sensitive to the depth of the PBL. At present there is effectively no adjustment of the PBL in the model across the rural-urban interface. The lidar data have shown large variations (up to 500m) across this interface on some occasions. Analysis of the synoptic situations / stability has revealed when these variations are largest. For example on the 9th July there was a difference of approximately 450m between the height over the 'urban' surface compared to the 'rural' surface. The distance between these two points was approximately 10km. This is considerably greater than the 200m height difference at 15:30 UTC as suggested by the different urban and rural ADMS model runs. This was illustrated in figures 6.5.4-6.5.7 .

At present the NAME model assumes that the top of the convective PBL remains uniform. The lidar data show that this is not necessarily the case, and the top may exhibit undulations. It is recommended that further investigation be undertaken to establish whether and how the NAME code should be modified to allow a non-uniform boundary top and rural to urban transition region. How this might be approached depends upon the grid resolution of the mesoscale model data; as the grid approaches 1 km or less, such non-uniformity will be more explicitly represented. NAME would then reflect this.

It is envisaged that these key results will impact upon air quality forecasts in two ways. Firstly, the models could be updated to reflect the observed phenomena. Secondly, consultants could use these observations to revise the magnitude of the variables that they use within the existing models. In both instances more data needs to be gathered.

7.4 Conclusions
Prior to this Project, dispersion model parameter data measured in the UK for testing NAME have been restricted to mast data at an urban site (up to 45 m) in Birmingham, or rural data (up to 1 km) at Cardington. The Dual Doppler Lidars have been tested and shown to deliver useful results especially at heights that conventional masts cannot reach and also probing the atmosphere at significant horizontal distances from the instrument site in an arbitrary direction. Consequently the deployment of the dual lidars means the findings of this report represent a significant advance in our understanding of the nature of the atmosphere across the rural urban interface.

A key result of the lidar observations was to indicate that urban pollution concentrations were frequently being underestimated using these models, though this observation was dependent upon the prevailing conditions.

Forecasting of pollution concentrations, including high pollution incidents, is entirely dependent on the efficiency of the models. If, as these results suggest, the models may have systematic errors in either their boundary conditions or the parameterisation calculations, then this has serious implications for the validity of such forecasts. Since this is the first time that this type of measurement has been made systematically over a

city, it is not unreasonable that tuning of these models needs to be carried out. Given that dispersion models have many input parameters [1], and the results are dependent on the mean meteorological conditions, it is important to have enough data to validate the models effectively.

It is concluded that within this project the observations made by dual Doppler lidar have allowed an increased understanding of the pollution dispersal mechanisms around an urban rural interface. From this understanding suggestions to improve current air quality forecasting models have been made.

7.5 Recommendations
As the Project's data are drawn together, a number of new scientific questions arise. These emerging questions will take significant effort to answer properly and goes beyond the current scope of this project. It is important to stress the fact that ultimately the lessons learnt from these comparisons of single and dual lidar with dispersion model parameters will lead to the improved understanding of the atmosphere. In turn this will allow the necessary adjustments of current models to make more accurate air quality forecasts in the future.

A key result of the lidar observations was to indicate that urban pollution concentrations were frequently being underestimated using these models, though this observation was dependent upon the prevailing conditions. Only further observational work under differing atmospheric conditions, would allow these variations to be fully understood and quantified.

It is therefore recommended that further field trials are undertaken, whilst the lidar equipment is fully functional, in order to build on this achievements of ISB-52 and to allow the full validation of air quality models.

8 REFERENCES

[1] DR Middleton, Matching urban lidar data to dispersion models. ISB52-01March 02.

[2] Pearson, GN DV Willetts, & RI Young. Boundary layer meteorology by pulsed lidar. ISB52-02. April 02.

[3] GN Pearson & DV Willetts, Assessment of lidar performance and data from the first dual Doppler lidar trial. ISB52 TWP March 2003.

[4] RI Young, S Siemen, AR Holt & GJG Upton, Identification of key flow parameters for visualisation ISB52-03 Aug 02.

[5] F Davies, C Collier, K Bozier & DR Middleton, Identification of key parameters for dispersion models. ISB52-04 Feb 2003.

[6] RI Young, F Davies, GN Pearson, DV Willetts & K Bozier, Description of the first ISB-52 Dual Doppler lidar trial. ISB52-05 March 2003.

[7] Boundary Layer Measurements of Dispersion Model Parameters using Dual Doppler Lidar at Malvern, UK. F Davies, C Collier, A Holt, D Middleton, G Pearson, S Siemen, DV Willetts & RI Young. ISB52 -06 July 2003.

[8] RI Young, GN Pearson, C Collier, F Davies & K Bozier. Description of the RAF Northolt ISB-52 Dual Doppler Lidar Trial. ISB52-07 August 2003.

[9] S Siemen and AR Holt. Visualisation of Dual Doppler Lidar data, ISB52-08. November 2003.

[10] S Siemen, AR Holt & A Pilgrim.Visualisation of Dual Doppler lidar data software user handbook. ISB52-09. August 2004.

[11] CG Collier, F Davies, AR Holt, DR Middleton, GN Pearson, DV Willetts & RI Young. Dispersion model testing using dual lidar data.. ISB52-10. June 2004.

[12] Pearson G N and Collier C G (1999) A pulsed coherent $CO2$ lidar for boundary layer meteorology. *Q. J. R. Meteorol. Soc*., 125, 2703 – 2721.

[13] Bozier K.E. Pearson G.N. Davies F. and Collier C.G. (2004) Evaluating the precision of a transverse excitation atmospheric based $CO2$ Doppler lidar system with in-situ sensors. *J. Optics A: Pure Appl. Opt*. 6, 1-9.

[14] Ryall D B and Maryon R H (1996). The NAME 2 Dispersion Model: A Scientific Overview. Met Office Turbulence and Diffusion Note No. 217b.

[15] Maryon R H, Ryall D B and Malcolm A L (1999). The NAME 4 Dispersion Model:Science Documentation. Met Office Turbulence and Diffusion Note No. 262. Met Office London Rd Bracknell Berks RG12 2SZ, UK.

[16] Webster H N and Thomson D J (2001). In search of a new plume rise scheme for NAME. Met Office Turbulence and Diffusion Note No. 272.

[17] Gal-Chen T, Xu M and Eberhard W L (1992) Estimations of Atmospheric Boundary Layer Fluxes and Other Turbulence parameters from Doppler Lidar Data. *J.Geophys. Res.*, 97 18,409-18,423.

[18] Frehlich, R.G., Hannon, S.M. and Henderson, S.W. 1994 'Performance of a 2μm coherent Doppler lidar for wind measurements', J. Atmos. Ocean Tech., 11, 1517-1528.

[19] Frehlich, R.G., Hannon, S.M. and Henderson, S.W. 1998 'Coherent Doppler lidar measurements of wind field statistics', Boundary-Layer Met., 86, 233-256.

[20] Davies, CG Collier, GN Pearson and KE Bozier. (2004) Doppler lidar measurements of turbulent structure function over an urban area. *Journal of Oceanic and Atmos Tech. 21 753-761.*

[21] Rye B J and Hardesty R M (1993) Discrete spectral peak estimation in incoherent backscatter heterodyne lidar. II Correlogram accumulation. *IEEE Trans. Geosci. Remote Sens.*, 31, 28 - 35.

[22] www.metoffice.com/research/nwp/numerical/operational/index.html

[23]http://www.metoffice.com/research/nwp/publications/nwp_gazette/jun02/um.html

[24] http://www.metoffice.com/research/nwp/numerical/unified_model/new_dynamics.html

[25] Oke, T.R. 1990 Figure 8.10 on page 283 Boundary Layer Climates, 2nd Edition 1987, 1990, Routledge, London.

[26] http://www2.dmu.dk/atmosphericenvironment/cost715.htm

[27] Browning and Wexler, The Determination of Kinematic Properties of a Wind Field using Doppler Radar. Journal of Applied Meteorology, Vol. 7, 105-113pp, 1968.

[28] Mok T.M. and Rudowicz C.Z. (2004) A lidar study of the atmospheric entrainment zone and mixed layer height over Hong Kong. *Atmospheric Research*, 69, 147 – 163.

[29] Middleton and Davies. Evaluation of dispersion model parameters by dual Doppler lidars over west London, U.K *9th International Conference on Harmonization within Atmospheric Dispersion Modelling for Regulatory Purposes 1-4 June 2004.*

[30] Davies, Middleton and Pearson. Observations of boundary layer depth over an urban / rural transition *A.M.S. 5th Symposium on the Urban Environment, 23-27 August 2004.*

[31] Davies, Collier, Bozier, Middleton, Pearson. Dual Doppler lidar measurements for improving atmospheric dispersion models *Photon 04, 6 – 10th September* – 2004.

[32] Collier and Davies. Observations of the development of the Convective boundary layer using radar and Doppler lidar. *European Radar Conference, Sept. 2004.*

[33] Drobinski, P.A., Dabas, A.M. and Flamant, P.H. (2000): Remote measurement of turbulent wind spectra by heterodyne Doppler lidar techniques, *J.App.Me.*, 39, 2434-2451.

9 GLOSSARY

ADMS - Atmospheric Dispersion Modelling System dispersion model from CERC

AEOLIUS - A dispersion model used by the Met office

AERMOD - A dispersion model from the American EPA.

BOXURB airflow - A dispersion model developed by the Met Office to describe through an urban canyon modelled as a box.

CW - Continuous wave

EPA - Environmental Protection Agency, a US government organisation

FWHH - Full width half height, a measure of the depth of field of the sensing zone of a CW lidar.

ISB - Invest to Save Budget

ISC - Dispersion model

LATAS - Laser Airborne True Airspeed sensor, an early Malvern Lidar

LDV - Laser Doppler Velocimeter

LDV1 - Laser Doppler Velocimeter 1 (A Lidar developed at Malvern).

MRU - Met Office research unit

NAME - Main dispersion model used by the Met Office

NWP - Numerical weather prediction

RAM - A dispersion model

RHI - Range height indicator

TEA Dioxide - Transfer excited atmosphere (pressure). A type of Carbon lasers that emits pulses of relatively high energy. Used in the pulsed lidar to achieve measurements to greater ranges.

10 Appendix 1 VARIABLES USED IN DISPERSION MODELS

A1.1. Introduction

Sensors for boundary layer measurements fall into two categories, as discussed by Kaimal and Finnigan (1994) Chapter A2. In situ sensors on masts and on the surface and within the ground were deployed in the Met Office urban field experiments in Birmingham; see Ellis and Middleton (2000). In situ sensors are the method of choice for surface studies owing to their accuracy and resolution for such quantitative work, Kaimal and Finnigan (1994). Remote sensors offer increased range and a spatial scanning capability, but according to these authors (ibid) are constrained in minimum range and spatial resolution. They suggest that

> "Used in combination, however, the two types of sensor provide a more
> complete description of the flow field being studied than either of the
> two can provide separately."

This is a most important point. It emphasises the underlying scientific relevance to the Met Office research programme of work with the Salford and Malvern Lidars in an urban context. The hope is through the ISB funded Contract, new insights for the turbulent flow fields within dispersion modelling to forecast air quality will result. This report examines the purpose, definitions, spatial and averaging properties of the most important variables that are used in dispersion models. It then addresses the Lidar output data to examine ways of matching the one style of data to the possible variables. Some dispersion quantities will not be yielded up from the Lidar output, and must still be measured in more traditional fashion.

A1.2 Wind Shear

Both wind-speed and direction change with height. This shear can have a dramatic effect upon a plume and dispersion models vary in their ability to represent such behaviour. They are often limited by the available input data, such as a mean wind at 10 m height, rather than a profile through the atmosphere. Radiosonde data or numerical weather model output can be used to obtain wind profiles. Wind shear can be modelled in typical conditions as is done in the ADMS model. The profiles for direction and velocity are functions of height to the boundary layer depth or base of lowest inversion according to the prevailing stability (defined below), viz:

1. In convective conditions there is much vertical mixing of momentum, and little change of wind direction and speed with height.
2. In stable conditions the vertical mixing of momentum is suppressed, and much sharper gradients occur.

The surface wind is usually 'backed' relative to the geostrophic wind in the northern hemisphere i.e. rotate anticlockwise from the geostrophic wind direction to get the surface direction. Typical observed angles (Hanna et al., 1983) between the surface wind and the geostrophic (free stream) wind are as follows:-

unstable 5-10°, neutral 15-20°, and stable 30-50°.

These angles represent a measure of the turning of the wind direction between the free flow above, and the wind near the ground. Wind velocity increases with height, gradually approaching the free-stream flow. The velocity profile depends on the stability (defined below), and as can be seen from measurements using a balloon ascent (or 'radiosonde'), may not necessarily fit any smooth analytic function. However a convenient formula for the increase in wind speed at greater height in neutral conditions is the logarithmic wind profile

$$u(z) = \frac{u_*}{k} \ln(\frac{z}{z_0})$$

When plotting the graph, of $\ln(z)$ versus $u(z)$,

$$\ln(z) - \ln(z_0) = \frac{k}{u_*} u(z)$$

with intercept $-\ln(z_0)$ and slope $\dfrac{k}{u_*}$.

Here $u(z)$ m s^{-1} is the mean wind velocity at the height z m in a neutral flow near to the surface i.e. within the boundary layer. The friction velocity u_* (m s^{-1}) has been discussed above; it can be measured by fitting this profile for $u(z)$ to observed values of the mean velocity at different heights. Rotach (1993) has emphasised the importance of locally derived values of scaling parameters. Thus friction velocity would be derived from the turbulence data directly (method 2 below; Section A1.2.1). The von Karman constant k does not depend on stability and is usually set to 0.4 (dimensionless). In neutral stability, when this equation is assumed to apply, once u_* has been measured and k estimated, the wind profile can be used to estimate z_0. It is derived from the intercept of the graph.

Measurements of $u(z)$ versus z in neutral stability will show reasonable scatter about a straight line of $u(z)$ versus $\ln(z)$. The slope is u_*/k and the intercept where $u(z) = 0$ is at a height z_0. The roughness length z_0 (as it is called) is used to describe the effect of how rough is the surface beneath the flow. The roughness length over the sea is typically 0.001 m, over lawn 0.01 m, uncut grass 0.05 m, and 1 m over wooded landscapes (Seinfeld, 1985, page 495). Roughness length is a measure of, but is much smaller than, the size of the roughness elements. Grimmond et al. (1998) have given a detailed comparison of methods to measure the roughness length for urban areas using anemometry. They also mention estimates based upon surface geometry i.e. 'morphogenetic' methods.

In stability's other than neutral, more elaborate functions are used to describe the variation of the wind with height. These functions give deviations from the logarithmic wind profile according to whether the conditions are stable or unstable. To do this they depend upon the Monin Obukhov length L (a measure of stability in the surface layer) as in Seinfeld (1985).

For completeness, we note that the friction velocity may be derived from three different ways of measuring the horizontal shear stress, as discussed by Nemoto and Nishimura (2001):
1. Profile method, using logarithmic fit in neutral stability, requiring anemometers (cup or sonic) at several heights (on a suitable well exposed mast).
2. Eddy correlation method, where turbulence components are measured (e.g. by sonic, or hot-wire anemometers) and covariance calculated to give the Reynolds stress. This gives the local friction velocity (below).
3. Direct measurement of drag force on the surface using a drag plate. This method has a long pedigree, and requires a carefully constructed mechanical assembly with strain gauges or other force-transducers.

A1.2.1 Local Friction Velocity u_*

The friction velocity may be derived from the vertical profile of wind speed versus height. This works over a uniform horizontal surface. Where the surface structure is more complicated, with roughness elements of differing sizes, as in an urban situation, Rotach (2001) has suggested that u* is best determined as the local friction velocity. This is done via the eddy correlation of fluctuating wind components measured with an ultrasonic anemometer (or similar device); it represents a direct measure of the local turbulent stress via the covariance:

$$u_* = \sqrt{-\overline{u'w'}}$$

In parameterising the urban turbulence and wind profiles, it is the local friction velocity that should be used. Rotach (2001) describes:

- a maximum at the top of the urban roughness sub-layer, at $z = z_*$,
- to be constant in the urban inertial sub-layer, at $z_* < z <\approx 0.1 z_i$,
- to decrease to small(er) values as $z \rightarrow z_i$,
- and to decrease towards zero as $z \rightarrow d$ or 0.

It would be a significant step forward to be able to determine in a field experiment the maximum in the local friction velocity u_* and its associated height z_* above an urban area. Likely values of z_* are thought to fall between 2 to 5 times (mean) building height; cf Rotach (2001), and Roth (2000). Here one must distinguish mean building height from the largest building height; a city often has a distribution of heights.

A1.2.2 Urban Roughness Scaling Height z_*

Because modern ideas on the urban Roughness Sub-layer suggest that a new quantity z_* should be measured, some trials are also needed to see if the CW lidar instrument LDV1 could identify the height z_* at which the Reynolds stress $\overline{u'w'}$ (or the related friction velocity u_*) passes through a maximum value. If the LDV1 could yield a profile of either quantity this would be a significant achievement in developing our methods to parameterise z_*. The urban roughness scaling height z_* is thought to fall in the region 2 to 5 times building height. See Rotach (in preparation) and Roth (2000). If z_* proves to be a useful new concept to include in dispersion models, it would be valuable to measure it over several UK towns and cities. The lidars could be deployed in a series of campaigns for this purpose. It is not clear whether measurements near enough to the ground can be made using the dual pulsed lidars; however LDV1 and the masts could provide useful lower level data.

A1.3 Measurements for Air Pollution Meteorology

In air pollution meteorology there are some measurements which are particularly relevant to the dispersion of pollutants. See also the AMS Workshop account by Hanna et al. (1977). Briefly, the instrumentation includes:

A1.3.1 Anemometer and Wind Vane

All anemometers require careful siting; the choice of site may often be a compromise between the ideal and the possible. The cup anemometer and wind vane provide basic data on wind speed and direction near the surface. They should be properly set up according to well established rules of exposure, such as distance from obstacles. A paper chart (anemograph trace) gives some idea of the fluctuations in wind direction.

A1.3.2 Bivane

The bivane is a delicately balanced vane designed to have two axes of rotation. It can respond rapidly to eddies in the wind, and yields the standard deviations of fluctuation of wind direction and elevation, $\sigma(\theta)$ and $\sigma(\phi)$. Methods to calculate standard deviations of wind direction are discussed by Verrall and Williams (1982), with allowance for the discontinuity when direction passes through 360°. The direction standard deviations, $\sigma(\theta)$ and $\sigma(\phi)$, enable plume spread parameters σ_y and σ_z to be calculated (see discussion of Practical Schemes, in Section A1.10 below). Formulae for the calculation were reviewed by Hanna et al. (1977). They caution that whilst the standard deviation of vertical wind direction $\sigma(\phi)$ is a good indicator of stability, it is a difficult parameter to measure. The ultrasonic anemometer (below) can also be used to measure these standard deviations (and is more robust), although such equipment may be better employed to measure the Monin Obukhov length L (below).

Sedefian and Bennett (1980) compared several schemes for classifying the turbulence regime, including the use of $\sigma(\theta)$. The standard deviation method to diagnose stability has been used in difficult situations, like remote valleys, e.g. Leahey and Halitsky (1973) who used bivanes. These standard deviations of direction measured in the field can be used to diagnose the Pasquill stability class. Strictly speaking (ibid), it is necessary to take samples for a period T and apply running means with the correct averaging time ($x/\beta u$ for travel distance x, wind speed u, and $\beta=4$) before the calculating standard deviations of wind direction. Some dispersion models such as ISC3, RAM, or CALINE will require the stability class as an input variable in order to describe the rate of plume spreading: the meteorological data must be processed before the model is run. When a model requires the direct input of standard deviation(s) of wind direction, but these are not available, sensible estimates may be made by referring to the values tabulated in Hanna et al. (1982) after the work of F Gifford. The values are as in Table A1.1.

Description	Pasquill Class[*]	Standard Deviation (at 10 m) σ_θ degrees
Very unstable	A	25
Moderately unstable	B	20
Slightly unstable	C	15
Neutral	D	10
Slightly stable	E	5
Moderately stable[**]	F	2.5

Table A1.1 Estimates of standard deviation of wind direction (from Hanna et al., 1982).

Notes:
* Pasquill stability category (or class) is defined later (Practical Schemes, Section A1.10)
** In the more stable conditions it is not easy to define the most appropriate value for the standard deviation of wind direction, largely because stable boundary layers may not be in equilibrium, and meandering of direction is seen in light winds. Larger horizontal standard deviations may be appropriate on occasion.

A1.3.3 Ultrasonic or turbulence anemometer

An ultrasonic anemometer uses three axes of measurements, recording the effect of air movement on the time taken for sound waves to traverse a short gap. There are no moving parts and rapid fluctuations in the flow are recorded. A lower frequency ultrasonic anemometer is also available. Ultrasonic anemometers have possible advantages of robustness over bivanes or propellers for use in towns. (Alternatively three lightweight propellers are used to record the three components of the wind, but are less rugged, and are subject to friction in the slowest winds.) Valuable statistics of turbulence are obtained from these instruments. With the components u, v in the horizontal and w in the vertical, their standard deviations are σ_u, σ_v, and σ_w. Fast response measurements of temperature can be derived from the sound velocity in air, which the device also measures. Turbulence measurements in conjunction with rapid measurements of temperature and water vapour (the latter requiring an additional instrument) can be used to measure the sensible heat flux and latent heat flux respectively. The stability parameter L (Monin Obukhov length) may then be calculated from the measured turbulence data (cf Seinfeld, 1986). This method of diagnosing stability via L relies on the measurement of fluxes. Diagnosis of stability via vertical temperature gradients will be considered later (see under Lapse rate).

A1.3.4 Upper Air Soundings
Radiosonde balloons are released from several sites in the country on a routine (synoptic) basis. Pressure, temperature, and dew-point (for humidity) define the state of the atmosphere as the balloon ascends. Its speed and direction (that of the winds aloft) are obtained by electronic means such as radar or satellite-based navigation systems, though a theodolite and rate of ascent can be used. Radiosonde data are invaluable in air pollution studies because they give information on the temperature profile, which is important in affecting the vertical motion of pollutants, and can be used to identify boundary layer depth.

A1.3.5 Sodar and Lidar
As implied by their names these are radar-type methods, using sound waves or light waves respectively. The general idea is to send a pulse of energy aloft, then to record the time taken for it to be scattered back to earth. Sound is scattered by regions with a lot of temperature fluctuation, light by particles and aerosol. The change in frequency due to Doppler shift reveals velocity data about the upper air as well. Each method has limitations, such as range, which is sensitive to ambient conditions. The data can be very useful in characterising conditions at a new site. Lidar is useful to identify plume rise. Sodar is able to characterise the mixing depth (defined above).

A1.4 Energy balance
The energy balance at the surface must be represented in dispersion models in order to diagnose the atmospheric stability. The urban energy balance is not usually done explicitly in existing models, although they all diagnose a stability. In order to make full use of the lidar data some characterisation of surface processes is required. This means the field experiments need to measure the radiation terms, sensible heat flux, and latent heat flux. The ground flux, or temperatures in the ground, are needed.

A1.4.1 Insolation
The sun has a high surface temperature (about 5800 K) and emits mostly in the visible and short wave part of the electromagnetic spectrum (400-700 nm). Energy reaches the upper atmosphere at a rate of about 1380 W m^{-2} (the solar constant). Energy

reaching the earth's surface (insolation) is in the range 0-1000 W m^{-2} at low-latitudes or in mid-latitude summer, but just 0-200 W m^{-2} in mid-latitude winter (McIlveen, 1992). The amount, which actually reaches the ground, depends on latitude, because this alters the path length through the atmosphere. It also depends on the season and time of day, as well as on local factors like cloud and precipitation. It is measured using an upward looking short wave radiometer. A downward sensor is also needed, because a significant fraction is reflected.

A1.4.2 Surface Cooling
Any surface emits long-wave radiation according to its absolute temperature T, and its emissivity. For a black body (emissivity is 1), the maximum energy E emitted per unit time per unit area of surface obeys Stefan's law (Seinfeld, 1988, page 448)

$$E = \sigma T^4$$

where the Stefan-Boltzmann constant $\sigma = 5.673 \times 10^{-8}$ W m^{-2} K^{-4} .
Gases in the air, cloud droplets, the sea and the land absorb incoming solar radiation. They also emit radiation according to their temperature. Surface cooling is influenced by the radiation loss and the thermal properties of the ground. Ground loss of radiation is measured by a downward looking long wave radiometer; an upward looking sensor is also needed to detect black body radiation from clouds and the air.

A1.4.3 Radiation and cloud
Cloud cover is routinely observed during each synoptic observation. The sky is divided into eighths and the amount of cloud in each layer and the height of the cloud base are reported in oktas and feet respectively. In the USA, cloud is reported in tenths. By day, without much cloud cover, the land receives more energy than it emits, so its temperature rises. By night, without much cloud cover, the land emits more than it receives so it cools down. Cloud can reduce the radiation reaching the ground during the day. By night, the clouds represent a surface that is warmer than a clear night sky, so their radiation reduces the rate of cooling of the ground. Daytime convective growth of the boundary layer and night time development of stable conditions by surface cooling are both affected by the extent of cloud cover. This is why the Pasquill stability Class is selected according to incoming solar radiation (day) or cloud cover (night), reflecting the importance of heating and cooling the air in driving or suppressing vertical motion Similarly, an estimate of the Monin Obukhov length is made within some dispersion models and the starting point could be cloud cover in order to calculate the radiation part of the energy balance (below). Ultimately the energy term needed is the sensible heat flux described below.

A1.4.4 Energy Balance
The energy received at the surface from the sun during the day depends upon the latitude, time of year, cloud cover, and surface albedo. The albedo is the fraction of the incoming radiation that is reflected back, typically 0.29-0.34 (Strahler and Strahler, 1992). The absorbed energy depends upon (1.0 - albedo), so a fraction 0.7 of the energy striking the surface after passage through the atmosphere and clouds is absorbed in the land or ocean. The albedo is very site specific. In meteorology it is necessary to know how the energy is shared between the air, ground and water. The flow of energy for each method of transfer is described as a 'flux', which means the rate of transfer of energy per unit area per unit time. Semantically, 'net radiation', like 'sensible heat flux' or 'latent heat flux', is also a flux, although the word 'flux' seems

to be dropped in common parlance when referring to the 'net radiation'. These energy terms in a simple energy balance at the surface are as follows.

Net radiation R_N is the incoming solar long wave radiation minus the outgoing radiation. Positive net radiation $R_N > 0$ means downward flux is larger than the upward flux, e.g. 60-80 W m^{-2} at noon, but -10 W m^{-2} overnight. Net radiation is strongly influenced by cloud cover.

Sensible heat flux H is the energy carried upwards (positive) or downwards (negative) by the turbulent motions of warm and cool air parcels, e.g. 280 W m^{-2} at noon, - 30 W m^{-2} overnight, where positive sensible heat flux denotes upward transport of heat. It is very important in controlling vertical mixing. Fluctuations w' in the vertical velocity and fluctuations θ' in the potential temperature (defined below) can be measured and their covariance calculated. With the vertical heat flux as H, density ρ, specific heat C_p

$$H = \rho\, C_p\, \overline{w'\theta'}$$

where $\overline{w'\theta'}$ is the vertical flux of temperature fluctuations i.e. $H / \rho C_p$.

Latent heat flux H_L is the heat of vaporisation carried upwards (positive) or downwards (negative) by the movement of eddies carrying water vapour.

Ground flux H_G is the rate at which energy is transferred between air and ground, being absorbed by the ground (positive) or lost from the ground (negative).

The simple energy balance at the surface is then (see Arya, 1988, pp. 10-12):

$$R_N = H + H_L + H_G$$

At night when winds are light, and skies clear, the net radiation is negative, causing cooling at ground level. Vertical mixing in the surface cooled layer is suppressed; mixing is poor. The air is stable. (The cooling can be sufficient for fog to form if the temperature goes below the dew point and wind is light). In the day, light winds and clear skies mean that the positive net radiation warms the ground rapidly, the temperature of air at the surface rises, and convection takes place. Vertical mixing is enhanced. The air is unstable.

A1.4.5 Stability
Dispersion models for air quality use the idea of stability as a means of quantifying the amount of mixing or spreading of a plume. Stability is a measure of whether the atmosphere is likely to enhance or suppress turbulent mixing. The Monin Obukhov length is used, assuming the urban area to be horizontally homogeneous. See below after Lapse Rate.

A1.5 Urban Surface Energy Balance
In urban areas, the normal terms in the energy balance apply. In addition there may be a change to the water cycle through irrigation or surface drainage. The storage of heat in buildings and concrete structures is very important, as is its slow release as night-fall approaches. Anthropogenic heating is also a contributor to the surface transfers of heat energy. Buildings and vehicles emit significant quantities of energy, perhaps attaining 10 % of solar input.

A1.6 Temperature and Pressure

A1.6.1 Ideal Gas Law
The familiar equation of state

$$PV = nR_0 T$$

applies to n (dimensionless) moles of gas at pressure P (N m^{-2}), absolute temperature T (K), volume V (m^3), and universal gas constant R_0 (8.31432 J mole^{-1} K^{-1}). In meteorology it is convenient to use the form:

$$R = \frac{R_0}{W}$$

to define the specific gas constant R J kg^{-1} K^{-1} with molar mass W kg mole^{-1}. In ideal conditions, gas at constant volume which is given a change in pressure from P_1 to P_2 experiences a temperature change from T_1 to T_2

$$T_2 = T_1 \frac{P_2}{P_1}$$

In the atmosphere this must be modified as below (to give Poisson's Equation) because the volume of an air parcel is not constant as it ascends and expands.

A1.6.2 Hydrostatic Equation
The pressure at the base of a column of fluid is the gravitational force due to the column above, per unit area. In the atmosphere, about 10^4 kg of air press down on each square metre (Lewis, 1991). If the pressure is P at height z with density ρ the mass of a layer of depth dz per unit area is just $\rho\, dz$. The change in pressure from z to $z+dz$ is dP:

$dP = -\rho\, g\, dz$

$$\rho = \frac{P}{RT}$$

$$dP = -\frac{P}{RT} g\, dz$$

Integrating from z_1 to z_2 gives the hydrostatic equation (McIlveen, 1992).

$$P_2 = P_1 \exp\left\{ -\frac{(z_2 - z_1)}{(RT/g)} \right\}$$

This equation applies to the vertical motion of air parcels, including pollutants. As a parcel rises, its pressure must decrease. The accompanying expansion causes a change in temperature, which may cause changes in state as well. In the atmosphere, measurements show that the absolute temperature T varies with height z from day to day and hour to hour. The hydrostatic equation enables the pressure difference across two heights to be calculated, assuming the layer of atmosphere has an absolute temperature T.

A1.6.3 Potential Temperature
In a laboratory a useful standard state is 'STP', standard temperature and pressure, 0 Celsius and 760 mm mercury (1013.25 mb). In the atmosphere a more practical standard is to refer everything to a pressure of 1000.0 mb, 10^5 N m^{-2}. The compression of the air without any change of state (no condensation/evaporation) and with no heat gain or loss is a dry adiabatic process. The potential temperature is the temperature of the parcel when it has been compressed reversibly to 1000.0 mbar in a

dry adiabatic process. However the air parcel can change its volume in the atmosphere, so we must allow for the work done by expansion, $P\,dV$.

Poisson's equation gives the new temperature in terms of the pressure change, allowing for the work done in the adiabatic expansion:

$$\frac{T_2}{T_1} = \left(\frac{P_2}{P_1}\right)^{R/C_p}$$

Define the potential temperature θ to be T_2 at $P_2 = 1000.0$ mbar. Then

$$\theta = T_1\left(\frac{1000.0}{P_1}\right)^{R/C_p}$$

where the air parcel at P_1 , T_1 , has potential temperature θ. The practical value of θ is that it converts T_1 into a temperature at the standard pressure of 1000.0 mb (10^5 Pa). This corrects the temperature for expansion due to the drop in atmospheric pressure with height. Note that R and C_p , should be in consistent units. For dry air, $R = 287$ J kg^{-1} K^{-1}, C_p =1004 J kg^{-1} K^{-1}, and the exponent R/C_p =0.286.

A1.6.4 Lapse Rate

Lapse rate (Latin: lapsus, fall) is the rate of decrease of temperature with height. Formally

$$\Gamma = -\left(\frac{\partial T}{\partial z}\right)$$

A positive lapse rate $\Gamma > 0$ is a decrease of temperature with height. A negative lapse rate $\Gamma < 0$ is an increase of temperature with height. A zero lapse rate $\Gamma = 0$ has no change in temperature with height.

A1.6.5 Environmental Lapse Rate

This is the lapse rate Γ_e as measured in the atmosphere, perhaps using a balloon and thermistor.

A1.6.6 Dry Adiabatic Lapse Rate

This is a theoretical ideal which is of much use when discussing the ascent or descent of air. When an air parcel ascends without change of state, it is assumed to cool adiabatically due to the drop in pressure with height. The dry adiabatic lapse rate has the form

$$\Gamma_d = -\left(\frac{\partial T}{\partial z}\right) = +\left(\frac{g}{C_p}\right)$$

The numerical value of Γ_d is 9.8 °C km^{-1}. The environmental lapse rate Γ_e is however often about 6.0 °C km^{-1}. Ascending dry air would cool adiabatically at 9.8 °C per km, whilst the surrounding air might actually get cooler at only 6 °C per km. The environmental lapse rate is said to be subadiabatic when it cools more slowly than the dry adiabat and is called stable. It is called a superadiabat when it cools more rapidly and is called unstable.

A1.6.7 Moist Adiabat

The atmosphere can contain significant amounts of water vapour. When considering the change of temperature with height, and the behaviour of air parcels as they move in the vertical, it is essential to include the effects of changes of state for the water. The dry adiabatic lapse rate described above is for the special case that no change of state occurs. This can be a useful description up to the height above ground at which temperature is cold enough for condensation to occur. Once above the condensation level (which is a good guide to the height of the cloud base) a moist or saturated adiabat must be used when discussing vertical motion of the air.

If condensation takes place, the latent heat of vaporisation of the water is released as heat and in turn adds to the buoyancy. The saturation adiabatic lapse rate is similar to the dry adiabat, but subtracts a term for the latent heat effect:

$$\Gamma_m = +\left(\frac{g}{C_p}\right) - \left(\frac{L}{C_p}\right)\left(\frac{\partial m_s}{\partial z}\right)$$

where the moist adiabat Γ_m contains an extra term which depends upon the latent heat L and vertical gradient of water vapour m_s. Here m_s is the mass of water vapour per mass of air at saturation, itself a function of temperature. When saturation occurs, the temperature decreases more slowly with height than for the dry adiabat. Hanna et al. (1982) give values for the moist adiabat ranging from 9 °C per km (cold polar air) to 4 °C per km (warm tropical air).

A1.6.8 Using the Lapse Rate: Stability
A stable atmosphere arises when it is difficult for air to be moved up or down. In a neutral atmosphere the motion is not affected. In an unstable atmosphere, vertical motion tends to be enhanced. The stability of the atmosphere is dependent on the temperature lapse rate. If air is moved up a distance dz from a height z, then its temperature decreases from T at z to become $T - \Gamma_d\ dz$ at height $z + dz$. However the surrounding air will have a temperature $T - \Gamma_e dz$ at the new height. Three cases arise for dry air:

1. If $T - \Gamma_d\ dz < T - \Gamma_e dz$ then the air parcel is colder than its surroundings at the new level. It will be more dense and tend to sink back, suppressing the motion. Conditions are stable.
2. If $T - \Gamma_d\ dz = T - \Gamma_e dz$ then the air parcel cools at the same rate as its surroundings. It will keep the same temperature and the same density as the air around it. The motion is not affected there being no buoyancy difference, so conditions are neutral.
3. If $T - \Gamma_d\ dz > T - \Gamma_e dz$ then at the new level the air parcel is warmer than its surroundings. It will be less dense and tend to continue to rise, enhancing the motion. Conditions are unstable.

The conditions for stability are in Table A1.2.

Stability	Typical conditions	Environmental versus Dry Adiabatic Lapse Rate	Environmental Temperature Gradient	Description
Stable	Overnight, clear sky, light wind	$\Gamma_e < \Gamma_d$	$\partial T_e/\partial z > -9.8$ C km^{-1}	Subadiabatic
Neutral	Overcast, windy, day or night	$\Gamma_e = \Gamma_d$	$\partial T_e/\partial z = -9.8$ C km^{-1}	Adiabatic
Unstable	Clear skies, strong sunshine light wind	$\Gamma_e > \Gamma_d$	$\partial T_e/\partial z < -9.8$ C km^{-1}	Superadiabatic

Table A1.2 Stability conditions in terms of the environmental (i.e. actual) lapse rate.

These conditions also apply for downward motion (as is seen by replacing *dz* by - *dz*). Stable conditions suppress the displacement, whether it be up or down. Unstable conditions enhance the motion in either direction.
Note: in this context we refer to 'static' stability; dynamic stability has a different cause and meaning.

A1.6.9 Inversion
There are several causes (see below) for a temperature inversion: radiation, subsidence, frontal (Seinfeld, 1986) page 462. They amount to cooling from below, or warming from above.

A subsidence inversion is the result of descending air (subsidence) being warmed by compression. The warming of elevated layers of air can be more than lower down and lead to an inversion. Anticyclonic situations have subsidence and a tendency for poor air quality.

Frontal inversion occurs at a front which is where air masses of different temperatures, pressures and humidities meet. In warm or cold fronts the warm air lies above a sloping wedge of colder air, causing an inversion.

An advection inversion occurs when warm air flows over a cooler surface. Warm air off the sea passing over cold land, gives a surface-inversion. If a cool sea-breeze is overlaid by a warm land-breeze, the result is an elevated inversion.

A radiation inversion occurs when on a clear night radiant heat is lost to space and the ground cools rapidly. Air near the ground is also cooled and can become very still; this is a surface-inversion. Air quality can be very poor when conditions are stable. Such radiation cooling causes the familiar ground frost.

In the convective boundary layer the height of the base of the first inversion layer from the ground is the inversion height z_i (Lenschow, 1986; Chapter 1, p. 6). This inversion layer is often quite conspicuous as a sharp increase in θ at some elevation when vertical profiles of temperature and humidity are plotted. It is especially informative to plot height z versus potential temperature θ.

A1.7 Averaging the Planetary Boundary Layer

When the matching of the Lidar data to dispersion model variables is considered, it quickly becomes apparent that careful definition of "averaging" is required. The importance of averaging is discussed by Lenschow (1986; Chapter 1, pp. 6-7) In a turbulent boundary layer, there is a seemingly random three dimensional velocity field, along with random scalar fields of temperature, humidity, and pollutants. Averaged quantities are therefore studied. Averaging minimises the apparent chaos in the instantaneous values. In the daytime the averaging is especially important because large convective eddies can strongly bias short-term observations.

Lenschow (ibid) identifies several ways to average:
1. In turbulence theory, as an average over an infinite number of realisations, an ensemble average.
2. In numerical models (and we may add, especially in numerical weather prediction, NWP) a volume average is also used.
3. In experimental data processing, averages may be of the ensemble type, or taken over volume, area, line, or time.

A volume such as in NWP can be very large e.g. a layer of atmosphere some hundreds of metres deep and many kilometres in each horizontal co-ordinate. The NAME model for example running on mesoscale NWP data has its lowest level at approximately 10 metres and the grid is on a $\approx$10-12 km spacing; the volume is thus of order $\approx 10^9$ m^3. NAME would receive an updated value for the mesoscale NWP data in this cell every 1 hour. On global NWP data the grid scale jumps to $\approx$ 60 km and time spacing to 3 hours.

The NWP data represent time separated instantaneous sample values drawn from a continuously evolving field. They have implied spatial averaging over model cells; the cells vary in size due to the non-linear height co-ordinate and spherical grid layout. Furthermore, variables such as wind components, temperature and pressure are arranged on staggered grids to suit the numerical formulation of the forecast model. The evolution of the weather fields within the numerical forecast model is not 'seen' by the dispersion model NAME, which can only retrieve archived values; these are restricted by storage and other resource constraints (e.g. more frequent output from NWP means more computer time for the forecast as it runs) to 1 hour (mesoscale) and 3hour (global). A number of dispersion model variables are not output in the NWP data, and must be generated subsequently within NAME. This point will be discussed elsewhere in this report.

A Lidar may take a series of values from light back-scattered from the many aerosol particles within some sampling volume; the volume is approximately a beam cross-sectional area times the gated pulse length (speed of light times gate time window). For a 30 cm diameter beam with gated pulse length 150 m, the implied sampling volume in any instant would be of order $\approx$ 10.6 m^3.

Time averaging on an ultrasonic anemometer may be for 10 minutes or an hour, with velocity recording at a fixed point from 4 to 20 times per second (according to instrument and data logging set up). The sampling time may be designed to match air pollution and traffic recording, which are usually hourly, being reported at each hour-

end, or for some time period 2^n seconds to suit spectral analyses. In some experiments both sampling periods may be required. In intensive field campaigns it is therefore best to store all the raw data for subsequent processing and analyses. In routine continuous observations, this may be too costly in resources and near real-time data reductions become essential.

A1.8 Richardson number
Richardson derived an equation for the rate at which turbulent kinetic energy was produced (Sutton, 1953, page 152). His ratio is a convenient and dimensionless measure of whether the atmosphere was tending to create turbulence or to dissipate it.

$$Ri = \left(\frac{g}{\theta}\right)\frac{\left(\frac{\partial \theta}{\partial z}\right)}{\left(\frac{\partial u}{\partial z}\right)^2}$$

McIlveen (1992, page 304) points out that when Ri falls to less than 0.25, turbulence is expected to appear. Similarly, when Ri exceeds 0.25, turbulence is suppressed: conditions are stable. This criterion, or variants of it, are used to locate the top of the boundary layer depth in some models. Ri changes sign, becoming negative in unstable conditions because $\frac{\partial \theta}{\partial z} < 0$. Similarly, $Ri = 0$ in neutral stability. See Seinfeld (1986) page 495 for further information.

A1.9 Brunt Vaisala Frequency
The temperature varies with height, but this may differ from the adiabatic lapse rate. Consider an air parcel which is moved to a different height. Its temperature will follow the adiabat, but the surroundings need not. If the surrounding air in the environment at the new height has a different density then a buoyancy force exists. When the buoyancy force is opposite to the displacement, we have a restoring force at work. Simple harmonic motion is possible. The familiar equation for simple harmonic motion becomes:

$$\frac{\partial^2 z}{\partial t^2} = -N^2 z$$

where

$$N^2 = \left(\frac{g}{\theta_e}\right)\left(\frac{\partial \theta_e}{\partial z}\right)$$

Here θ_e is the potential temperature of the environment at the height z of interest. N defined as above is the angular frequency of the motion, the Brunt Vaisala frequency. For N^2 to have a real root, the oscillations with frequency N require stable conditions i.e. the surrounding air must cool at an environmental lapse rate (see above) which obeys $\Gamma_e < \Gamma_d$. The air must cool more slowly with height than the dry adiabatic lapse rate for there to be a restoring force.

The Brunt Vaisala frequency is of significance in air quality problems where there is the chance that vertical oscillations of the air could bring pollutants towards the ground. Simple models do not usually consider a plume whose height may oscillate with gravity waves to the lee of an obstacle such as a ridge. The wavelength (McIlveen,1992, page 360ff, 368ff) is

$$\lambda = \frac{2\pi u}{N}$$

for a wind speed u over the obstacle. The wavelengths can be 3-20 km.

A1.10 Monin Obukhov length

The Monin Obukhov length L expresses the relative importance of shear (speed change with height) and convection in creating turbulence, and has the form of a length scale because it takes convective thermals some distance to accelerate to the point where they generate significant turbulence. This variable is used to describe the stability of the atmosphere in many field experiments. It is an essential parameter in modern dispersion models. Businger in Nieuwstadt and van Dop(1982) has defined the basis of L. In attempting to solve the equations governing the flow, some simplifying assumptions about the turbulence have to be made. Otherwise the mathematical problem of 'closure' is met, where there are more unknowns than equations, and which would make solution impossible. In the course of writing down equations for the so-called second-order closure, two terms for the production of turbulence kinetic energy appear. They are the production due to shear in the mean flow, and production due to buoyancy which tends to cause vertical motions. Obukhov sensed that the height above the surface where these two terms were equal might be a useful measure. Near the surface, shear production is dominant; above the height of the Obukhov length L buoyancy production is dominant. He solved for the height where the ratio of these terms was equal to one. He made the assumption that near the surface the wind speed obeyed

$$\frac{\partial u}{\partial z} = \frac{u_*}{kz}$$

which on integration gives a logarithmic wind profile seen above. The friction velocity u_* m s^{-1} is measured via the wind speed fluctuations, using the shear stress as noted earlier.

He arrived at a definition of the Obukhov length in metres as

$$L = -\frac{\theta u_*^{3}}{kg\,\overline{w'\theta'}}$$

where $\overline{w'\theta'}$ is the vertical flux of temperature fluctuations (measurable using an ultrasonic anemometer with eddy correlation of fluctuations in temperature and vertical wind velocity), k is the von Karman constant (typically 0.4), and g the acceleration due to gravity. The minus sign has been introduced so that L has the same sign as the Richardson number. L and Ri are >0 in statically stable conditions but <0 in statically unstable conditions.

With the vertical heat flux H, density ρ, specific heat C_p, vertical flux of temperature fluctuation $H/(\rho C_p)$, and average temperature of air near the surface T_s (i.e. absolute temperature in degrees Kelvin), an alternative form is

$$L = -\frac{T_s u_*^{3}\rho C_p}{kgH}$$

This is convenient when T_s, H and u_* can be estimated from routinely observed meteorological quantities (and the other quantities ρ, C_p, k, g are constants). Arya (1988) page 159 has a useful nomogram for L as a function of friction velocity and surface heat flux.

By definition L could have values in the range $-\infty \le L \le +\infty$. The sensible heat flux $|H|$ is usually of magnitude 10 to 120 W m^{-2} and the friction velocity u_* is always positive and its magnitude is often 0.05 to 0.25 m s^{-1}; the practical range of $|L|$ is 1 to 1000 m.

1. When conditions are unstable, with upwards positive heat flux H, L is negative.
2. When conditions are stable, with downwards negative heat flux H, L is positive.

According to Lewis (1991), L is positive and small in stable conditions with light winds at night. It is small and negative (about -10 m) on strongly convective days, about -100 m on windy days with some solar heating, and tends to infinity in the neutral case with purely mechanical turbulence. Processing of routine meteorological observations is used to estimate L for use by the ADMS or AERMOD models; likewise the Indic model can process measurements of turbulence, temperature and wind speed to obtain L.

Incidentally, the Monin Obukhov length can be used to obtain a dimensionless height ζ.

$$\zeta = (z/L)$$

The height ζ is the vertical co-ordinate used in Monin Obukhov similarity theory (proposed by these workers in 1954). It is used by the more modern dispersion models in formulae (cf Seinfeld, 1986) that describe as a function of height z the state of the atmosphere near the ground.

For Monin Obhukov in urban areas, remember that local values of the scaling variables are required (Rotach, 1999).

A1.11 Convective Scaling Velocity

Near to the surface the flow is strongly affected by the frictional drag. Therefore as noted above the friction velocity is a useful quantity. In strong convection and well away from the surface another scaling velocity is required, because the flow is being driven upwards by the thermals. The convective velocity scale w_* has been used successfully when trying to match laboratory studies of convection in water tanks to observations in the atmosphere. (cf Tennekes, in Nieuwstadt and van Dop, 1982, page 59). The value of w_* is related to the mixed-layer height h, the height to which convection has grown, and the surface heat flux H (Arya, 1988, page 178) was discussed earlier. Here a temperature difference between the surface air and that higher up is driving the convection with a characteristic velocity w_*

$$w_* = \left(hg \frac{\left(\overline{w'\theta'} \right)}{\theta} \right)^{\frac{1}{3}}$$

where $\left(\overline{w'\theta'} \right)$ is the vertical flux of temperature fluctuations and can be expressed in terms of the sensible heat flux H via $H / \rho C_p$ as seen earlier.

The convective velocity scale w_* has meaning only in unstable conditions when there is upward movement of heat, just as the Brunt Vaisala frequency N has meaning only in stable conditions. These parameters have a special role to play in the more modern models when seeking to model dispersion, especially for elevated plumes that are well above the ground.

A1.12 Height to Maximum Stress (Depth of Roughness Sub-Layer) z_*

This is the height above ground at which the friction velocity attains its maximum value. It will typically be a few times building height, as discussed earlier. It can be derived from the profile of Reynolds stress.

A1.13 Roughness Length z₀

This is the measure of the roughness, as it appears in the wind profile. It can be derived from the wind speed data versus height.

A1.14 Displacement Height d

This is a scaling height where the Reynolds stress and mean wind speed fall to near zero.

A1.15 Mixing Height

This quantity has great importance for improving urban air quality forecasts. The mixing height is used in several dispersion models as the height from the ground through which pollutants may be expected to disperse. It is a useful concept but fraught with difficulty because in the real atmosphere it is not easily defined. On some occasions there is a well defined single inversion at some height above ground, acting as an effective lid to prevent vertical mixing of pollutants above it. In the case of large buoyancy or momentum driven plumes, the flow may partially or wholly penetrate the inversion, and then sinks back to its proper density determined height as the overshooting motion is damped and decays. On other occasions there may be a ground based inversion, so the layer of air near to the ground is stable, suppressing vertical spread. The possibility of multiple layers in the atmosphere should also be remembered, according to the interactions between the synoptic flow, local mesoscale effects like sea breezes or valley winds, topographic effects, and urban effects. Diagnosis of a boundary layer depth or mixing layer height will not be straightforward in such a situation.

A2 SPECTRUM OF TURBULENCE

A2.1 Introduction to Spectra

Early work to measure a spectrum of turbulence was inspired by G I Taylor and conducted in the wind tunnel using electrical analogue filtering circuits by Simmons and Salter (1938).

Spectra of atmospheric turbulence were the subject of active study in the 1950s. Panofsky and Deland (1959) provide a clear introduction:

- Power spectra describe the contribution of oscillations with particular frequencies f or wave numbers f^{-1} to the total variance of a variable.

- For turbulence, the variables are the velocities u, v, w in the three Cartesian directions x, y, z along wind, cross wind and vertical respectively.

- Velocity components when given as a function of time at a fixed point yield the Eulerian time spectrum as a function of frequency. Most spectral estimates are from fixed anemometers so represent Eulerian time spectra.

- Velocity components when given simultaneously at many points yield the Eulerian space spectrum as a function of wave number. With a many-point sample, usually measurements are all along a line, giving a one-dimensional Eulerian space spectrum. This is described simply as the "space spectrum" in their

paper (ibid). This is the case with a anemometer mounted on an aeroplane flying through the turbulent boundary layer, Panofsky and Deland, 1959. However Lenschow, 1986, Section 4.2 page 10, suggests a moving probe like an aircraft measures time series data.

NB: Perhaps this contradiction arises because the more modern instrumentation is much faster in acquiring data, so the time and space changes even as an aircraft flies may now be resolvable.

- When the values are fluctuations of the velocities of a given particle of air with time, they yield the Lagrangian space spectrum. Lagrangian space spectra may be studied by following individual air elements by means of a tracer, or when analysing the statistical properties of diffusion from a continuous source.

With regard to the measurement of spectra, and their practical, even engineering, application, Panofsky and Deland (1959) further explained that:

- Eulerian <u>time</u> spectra are related to easily measured atmospheric variables, but are least useful in applications.
- Eulerian <u>space</u> spectra are most relevant to the reactions of structures to turbulence, particularly aircraft.
- Lagrangian spectra are required for the prediction of dispersion.

Consequently they point out (ibid) that it is important to know if the various spectra are related, and whether point (fixed anemometer) and line (aircraft) observations can be combined to improve understanding.

NB: Lagrangian spectra are not discriminated here into time and space variants.

A2.2 Time Spectra and 1-D Space Spectra

Quoting Panofsky and Deland (1959, p. 42):

> "G I Taylor (1938) postulated that time spectra should be equivalent to space spectra in the direction of the mean motion, provided that t is replaced by x/U, or the frequency n by kU where U is the mean wind speed and k the wave number. Taylor further stated that this transformation would be satisfactory provided the level of turbulence is low. Ogura (1953) and Gifford (1956) developed a theory indicating that the relation should be good even when the ratio of the turbulent fluctuations to the mean wind speed is of order one."

(Here t is time, x distance in the mean flow direction downwind, U mean flow velocity, n frequency, and k the wave number n^{-1}).

Panofsky and Deland (1959, p. 42) quote wind tunnel studies, and atmospheric work, by others, as experimental verification of Taylor's hypothesis for wavelengths up to 200 m. In an urban atmosphere, especially near or amongst the roughness elements, it is not certain if Taylor's hypothesis still applies. This could be significant when lidar data are being transposed into a form consistent with dispersion model met-preprocessors. Its significance or otherwise in the planned experiments with the dual lidars is unclear at the time of writing. However in discussion it is natural to assume some aspects of the flow are at least reproduced over some area, but this implicit assumption may not be true near the urban surface. If the turbulence fields vary rapidly in space it may constrain the use of simplifying assumptions in processing lidar data. The lidar scans on an arc as the beam elevation is changed; for a given lidar

gate time, or distance up the beam, the sampling point is changing position horizontally across the city as the elevation is altered.

A2.3 Conventions with Spectra

Spectra plot the frequency n (Hz *i.e.* s^{-1}) horizontally. Alternatively, they may plot wave number $k = n^{-1}$ (s) on the horizontal axis. When several orders of magnitude are involved, the logarithm of frequency $\log n$ or of wave number $\log k = -\log n$ is plotted on the horizontal axis. The power (J s^{-1}) associated with each frequency is plotted on the vertical axis.

A2.4 Turbulent Kinetic Energy TKE

Kinetic energy is defined as

$$KE = \frac{1}{2}mv^2 .$$

Its dimensions are ML^2T^{-2} and units J.

If the mean velocity is $\bar{u}$ the kinetic energy of the mean flow per unit mass is

$$MKE = \frac{1}{2}\bar{u}^2$$

where the overbar implies that a mean value of the velocity is taken.

Turbulent kinetic energy (J) is defined as $\frac{1}{2}m\overline{u'^2}$.

Turbulent kinetic energy per unit mass (J kg^{-1}) is therefore given by

$$TKE = \frac{1}{2}\overline{u'^2} \equiv \frac{1}{2}\overline{(u-\bar{u})^2} \equiv \frac{1}{2}\sigma_u^2$$

Here σ_u^2 is the variance of the velocity fluctuations[1], $\overline{u'^2}$.

The velocity fluctuations u' are measured by subtracting $\bar{u}$ from $u(t)$; and $\overline{u'^2}$ is found by calculating their standard deviation. Note that $\overline{u'^2} > 0$.

In meteorology, it is traditional to consider unit mass of air, implying $m = 1$.

Considering all three components of the flow, with variances of velocity fluctuations σ_u^2, σ_v^2, and σ_w^2 gives

$$TKE = \frac{1}{2}\left(\sigma_u^2 + \sigma_v^2 + \sigma_w^2\right)$$

Three methods of deriving the mean velocity $\bar{u}$ were analysed in the Appendix to Sakai et al. (2001):

1. Centred running mean (their equation A1) of an odd number of successive measurements centred upon the time t . There is no phase lag (their equation A2).
2. Block average, where an average over a time interval is used for $\bar{u}$. The block average is often used: $\bar{u} = \frac{1}{n}\sum_1^n u_i$ .The transfer function is their equation A3.

---

[1] It can be shown that $\overline{u^2} = \overline{(\bar{u}+u')^2} = \overline{\left(\bar{u}^2 + 2\overline{u}u' + u'^2\right)} = \bar{u}^2 + 2\overline{\bar{u}u'} + \overline{u'^2} = \bar{u}^2 + \overline{u'^2}$ since $\overline{u'} = 0$.

3. Linear trend removal where the mean flow is represented by a fitted straight line across the interval. A phase change is introduced (see their equation A4).

Sakai et al. (2001) describe transfer functions for each method. Consideration must be given to outliners in the data for $u(t)$ when filtering the data to derive $\bar{u}$. The work of Sakai et al. (2001) has significance in the present Project because it highlights the importance of low frequencies when measuring fluxes over a rough surface. Lessons drawn from their forest studies are relevant to our urban experiments.

A2.5 Eddy Dissipation

This is the process whereby the kinetic energy of the turbulent energies is being degraded into heat energy, or thermal molecular motions. It arises through the effects of molecular viscosity (below) acting as a frictional force upon adjacent layers of fluid having a velocity gradient between them. Before defining the eddy dissipation rate ε, we explain molecular viscosity η and its associated kinematic molecular viscosity ν.

A2.5.1 Coefficient of Molecular Viscosity η

The kinetic theory of gases reveals that when an ideal gas undergoes shear, so that one layer of gas moves past another, there is a frictional force. The force arises because molecules transferring between adjacent layers transfer momentum between the layers. The viscosity is a characteristic property of the fluid, being much smaller in a gas than in a liquid. The frictional force F increases with the velocity gradient u/d and with the area A of sheared fluid. The coefficient of viscosity η is expressed as the force per unit area per unit velocity difference between layers, with unit separation between layers:

$$F = \frac{\eta A u}{d}$$

Using mean molecular velocity v, molecular mean free path λ, density ρ, kinetic theory has:

$$\eta = \frac{1}{3} v \lambda \rho$$

In an ideal gas, the coefficient of viscosity derived from kinetic theory is independent of pressure P because λ depends inversely upon ρ. In real gases, the viscosity does vary with pressure, but only by small amounts, unless very high pressures are attained. The theory also shows that the coefficient of viscosity in a gas depends upon the mean free path λ, and hence upon the absolute temperature T of the gas.

As layers of fluid pass each other, work is done by the molecular viscosity. The work done being the frictional force times the distance of action. Within a turbulent flow, as the eddies twist and swirl past each other, velocity shear means that the kinetic energy associated with the turbulence is being constantly degraded into molecular motions i.e. into thermal energy, or heat. Molecular viscosity thus plays an essential role in turbulence by controlling this dissipation of the motions through smaller and smaller eddies into heat. This process increases the entropy of the molecules, so it is not reversible.

A2.5.2 Kinematic Molecular Viscosity υ

The coefficient of molecular viscosity η (above) may expressed per unit mass of fluid, by dividing by the density ρ, and this gives the kinematic viscosity $v = \dfrac{\eta}{\rho}$. The kinematic viscosity (Lewis, 1991) will vary with ρ in the atmosphere.

A2.3 Eddy Dissipation Rate ε
In the Navier Stokes equations for fluid flow, the velocity components may be separated into mean and fluctuating quantities (e.g. $\bar{u}$ and u' respectively). An equation for turbulent kinetic energy production can then be derived. Busch explains that the equation for turbulent kinetic energy includes terms which are dependent upon molecular viscosity. The shape of the turbulent energy spectrum is uniquely determined by the molecular viscosity ν and the turbulent kinetic energy dissipation rate ε. See for example Busch pp. 26-28 in Haugen Workshop on Micrometeorology; with reference to Equation 8.14. Thus, by measuring the spectrum of turbulence, and if in the inertial sub-range, it may be possible to estimate the corresponding value for ε. In this region the spectrum is expected to have the usual -5/3 behaviour.

Panofsky and Deland (1959; p. 47) divide the micrometeorological spectrum into 3 parts:
1. Frictional dissipation, with wavelengths of order ≈ centimetre.
2. Inertial sub-range, where turbulent energy is neither created nor destroyed. Theoretical predictions suggest the spectrum $S(n)$ varies as $n^{-5/3}$, where the frequency is n, but it also appears as $n^{-2/3}$ when plotted in the form $nS(n)$. Turbulence here is isotropic; the lateral wind components v, w have 30% more energy than the longitudinal component u.
3. Energy-producing range, where the form of the spectrum is not given by these authors (ibid) , but it must approach a non-zero value in the limit of zero frequency ($n \rightarrow 0$). n

Since there are three orthogonal wind components, three distinct one-dimensional spectra can be envisaged. Within the inertial sub-range (isotropic turbulence) the spectra tend to be similar. The height of observation z above the ground is an important consideration when interpreting the spectra. Spectra are plotted with a vertical co-ordinate (ordinate) as $\dfrac{nS(n)}{\overline{v_z}^2}$, where multiplying by the frequency n means that the area on the spectrum between two frequencies represents the variance contributed by motions between them. Here $\overline{v_z}^2$ is a normalising factor, the square of the mean velocity recorded at height z. The quantity $S(n)$ is the energy spectrum for the turbulent velocity fluctuations. Because of the wide range of possible frequencies, the horizontal axis plots the logarithm of frequency. Plotting of spectra in meteorology is reviewed by Kaimal and Finnigan (1994, Chapter 2, pp. 37-39.)

It may seem surprising at first glance that an energy spectrum is drawn from the velocity fluctuations, or rapid deviations from the mean, until one remembers that velocity squared (multiplied by half the mass) is a measure of kinetic energy. The spectrum of turbulence reveals the fraction of the turbulent kinetic energy carried by motions at different frequencies, within the measured range. The highest measured

frequency is limited to half the digitising frequency, and the lowest recorded frequency is constrained to have a period less than the duration of sampling.

Calculation of the turbulent kinetic energy dissipation rate ε from the spectral energy at the high frequency end of the spectrum is discussed in Kaimal and Finnigan (1994, Chapter 2, p. 36); see Term V in Equation 1.59 in, page 26 and their Chapter 2; pages 32-6A1. This high frequency part of the spectrum is called the inertial sub-range. Kolmogorov had argued on dimensional considerations that the turbulent kinetic energy $E(\kappa)$ for wave-number κ may be proportional to $\varepsilon^{2/3}\kappa^{-5/3}$. The formula (Equation 2.3) in Kaimal and Finnigan (1994, Chapter 2, p. 36) is due to Kolmogorov (1941) and represents the one-dimensional spectrum using wind velocity component u in the wave number form using κ_1:

$$F_u(\kappa_1) = \alpha_1 \varepsilon^{2/3} \kappa_1^{-5/3}$$

Equivalently, using frequency n:

$$F_u(n_1) = \alpha_1 \varepsilon^{2/3} n_1^{5/3}$$

Here α_1 is the Kolmogorov constant of proportionality, between $\approx 0.5 - 0$.A2. Hence

$$\ln F_u(\kappa_1) = \ln\left(\alpha_1 \varepsilon^{2/3}\right) - \frac{5}{3}\ln \kappa_1$$

and these spectra when plotted as $\ln(F(\kappa_1))$ versus $\ln(\kappa_1)$ will show in the inertial sub-range a slope of -5/3 with intercept $\ln\left(\alpha_1 \varepsilon^{2/3}\right)$. Since α_1 is known, ε can be determined from this intercept.

The turbulent kinetic energy dissipation rate ε is the amount of energy dissipated per unit time normalised by the mass of fluid. The dimensions of ε are $L^2 T^{-3}$ and units $m^2 s^{-1}$. The variable ε is used in dispersion models, especially random walk Lagrangian models like NAME, because under a typical velocity in the eddies, the smaller eddies dissipate faster, and the spreading of particles depends upon the sizes of the eddies. Near the ground, where strong shear is expected, ε increases rapidly (because it depends upon u_*^3/z).

It could be very useful if the Lidar could measure eddy sizes directly, but a potential problem lies in the relative sizes of the Lidar pulse volume (sampling space) and its relationship to eddy size (which could be greater or smaller). Ideally the three dimensional field of ε might be measured; furthermore direct measurements of ε in the vicinity of dispersing momentum and buoyancy driven plumes would be most valuable for the improving of air quality forecasting. The behaviour of turbulence in the urban Roughness Sub-Layer (RS), where u_* is not constant, may be somewhat different from that in the urban Inertial Sub-Layer, where u_* may be assumed to be constant with height. Consequently, measured profiles of ε will be most valuable. A comprehensive review of atmospheric turbulence over cities has been compiled by Roth (2000). Within the region up to some 2 to 5 times building height, the basis of several approaches to micrometeorological exchange processes is in doubt. He stresses the importance of urban turbulence measurements that are required within the

urban canopy and its overlying urban boundary layer. The present Project offers scope to address some of these needs in a way that traditional tall masts on their own would not. In short, much more is to be learned if the masts, LDV1, and dual lidar were to be deployed together. Even on its own however, the dual lidar system offers a capability of spatial sampling for the turbulence that governs urban pollutant dispersion over a city that will be unique.

A2.6 Integral Time-scale
Once the lidar has determined the turbulent kinetic energy dissipation rate ε, the other fundamental dispersion parameter is the integral time-scale of the turbulence.

Consider a point sensor that records a velocity $u(t)$ as a series of time or as space separated measurements u_i. Their mean velocity is

$$\bar{u} = \frac{1}{n}\sum_{i=1}^{n} u_i$$

This is an ensemble mean of n values. It represents a time average if the sensor is stationary and the flow moves past it.

It represents a spatial average if the points are spaced out by co-ordinate but are sampled together simultaneously in time. It could be regarded as a line, area or volume average according to the positions of the points sampled.

The turbulent fluctuation is

$$u'(t) = u(t) - \bar{u}$$

Their standard deviation has dimensions of velocity, units m $^{s-1}$, and from n values is given by

$$\sigma_u = \sqrt{\frac{1}{n}\sum_{1}^{n}\left(u_i - \bar{u}\right)^2}$$

(and when the mean value $\bar{u} = 0$, this would become the root mean square value).
The standard deviation of wind velocity fluctuations is a quantity of much importance in dispersion modelling. It is normally implicit that σ_u, σ_v and σ_w are to be calculated by some semi-empirical formulation in the dispersion model, and are Eulerian quantities. That is, they are treated as if derived from three-dimensional anemometer data taken at a fixed point. The spreading of particles is calculated using the standard deviations of the fluctuations in the three wind speed components. Note that the calculation of standard deviation is well defined and is not assuming any particular shape for their probability distribution. The wind speed fluctuations need not be normally distributed; σ_u, σ_v and σ_w can still be used to model dispersion.

The auto (i.e. self) correlation coefficient for a time lag τ is the dimensionless quantity

$$R(\tau) = \frac{\overline{u'(t)u'(t+\tau)}}{\sigma_u^2}$$

When there is a wide range of velocity fluctuations, the variance in the denominator will be large, and the auto correlation $R(\tau)$ will be small.
The integral time-scale of the turbulence is

$$T = \int_0^\infty R(\tau)\,d\tau$$

with dimensions of time, and units s.

The larger the eddies, the greater distance in space over which the velocity is correlated, and for a fixed point (Eulerian) sensor, the longer is the time for which the velocity values remain correlated. The larger the eddies, the slower does $R(\tau)$ decrease with increase in τ and the larger is its integral time scale, after Hanna et al. (1982; pp. 8 ff.). Since a large integral time scale implies larger eddies, this has implications for the dispersion of pollutants, and is used in the NAME model.

A2.6.1 Lagrangian Timescale τ_L

This is given by $t_L \equiv T$ under the assumption that the velocity values $u_i(t)$ were taken moving with the flow (Lagrangian sampling). This implies that the sensor is moving with the mean velocity $\bar{u}$ and is merely sensing the fluctuations in velocity of fluid next to the moving sensor. Once the Lagrangian velocity fluctuations have been measured, their auto-correlation's with increasing lag-times may be evaluated, and from the integral of the auto-correlation with respect to time, the Lagrangian integral timescale is determined. Directly measured values of the time-scale would, with the profiles of ε, fill a very significant gap in the dispersion modelling repertoire. Both variables have an important influence upon the calculated pollutant concentrations.

When Lagrangian measurements of velocity fluctuations are not feasible, an approximate route may be to determine the Eulerian integral time-scale, and to then make some assumption about the relative magnitudes of the two types of integral time-scale. Then the Lagrangian might be estimated via the Eulerian; in practise this route is the more likely.

A2.6.2 Eulerian Timescale τ_E

This is given by $t_E \equiv T$ under the assumption that the velocity values $u_i(t)$ were taken at a fixed point, not moving with the flow but allowing the flow to move past the sensor (Eulerian sampling)as if the turbulence were somehow frozen as in Taylor's hypothesis.

A2.7 Integral Lengthscale

For completeness, we note in similar vein that the auto (i.e. self) correlation coefficient for a point separation s is the dimensionless quantity

$$R(s) = \frac{\overline{u'(x)u'(x+s)}}{\sigma_u^2}$$

When there is a wide range of velocity fluctuations, the variance in the denominator will be large, and the auto correlation $R(s)$ will be small.

The integral length-scale of the turbulence is

$$L = \int_0^\infty R(s)\,ds$$

with dimensions of length, and units m. NB This L is not the Monin Obukhov Length. The larger the eddies, the greater distance in space over which the velocity is correlated, and for a fixed point (Eulerian) sensor, the longer is the time for which the velocity values remain correlated. The larger the eddies, the slower does $R(\tau)$ decay.

A2.7.1 Lagrangian Lengthscale

As before, with s replacing τ, this is defined using the velocities of particles following the flow.

A2.7.2 Eulerian Lengthscale

As before, with s replacing τ, this is defined using the velocities of particles measured on a fixed point.

Table A1.3 Characteristics of sonic and lidar sensors for atmospheric turbulence and mean flow components.

	3-D Sonic Anemometer	Continuous Wave Single Lidar	Pulsed & Gated Single Lidar	Pulsed & Gated Dual Lidar
Principle	Ultrasound time-of-flight	Doppler shift light frequency	Doppler shift light frequency	Doppler shift light frequency
Sampling Frequency	Typically log at 4-10 Hz Preset options only?	Rotate scan at ½ to 2 Hz. One height: 10/minute Five heights: 16 profile/hour	Pulsing at ≈100 Hz	Pulsing at ≈100 Hz
Spatial Coverage	Point measurement (few cm path)	Focal Plane at Variable Focal Length	Beam Volume for gate open period	Beam Overlap Volume for gate open
Averaging	Temporal average of time series	Volume average of Lorentzian sightline weighting function	Volume average over gate volume (long truncated cone)	Volume average over overlap space (long truncated cone)
Primary Measurement	3 orthogonal components u, v, w; u down-wind	Velocity resolved along beam axis	Velocity resolved along beam axis	Velocity resolved along each of 2 beam axes
Inferred Measurement	De-trend; Mean u, θ; Standard Deviation via Taylor: 'frozen turbulence'	Scan/rotate inclined beam to infer 'frozen flow' over scanned space (continuity)	Scan/rotate inclined beam to infer 'frozen flow' over scanned space (continuity)	Solve 3-D flow field from 2 beams' overlap components & 'frozen flow' - vertical slice
Number of samples for half hour	2^{14} Samples at 10 Hz gives 27.3 minutes	Integrate for 2 minutes to infer flow; Rotate 15 scans/half-hour	Trade-off scan pattern with sampling	Trade-off scan pattern with sampling
Location of Measurements	Mast: 15m, 30m, 45m. Structures obstruct wind. Tethersonde restricted in urban areas.	Range by varying focus Absolute maximum range 200m	Range from 3rd gate range out to 10 km	Range from 3rd gate range out to 10 km but limited to overlap reach of both beams

Table A1.4 A list of variables used in dispersion models, measured by a variety of techniques. (Not all of these are measurable by lidar.)

Variable	Symbol	Notes
Mixing height	z_i	Height of lowest inversion Beware multiple layers
Boundary layer depth	h	Rural value City has internal layer(s)
Wind speed	$u(z)$, $v(z)$, $w(z)$,	Plume models use $u(10)$
Wind direction	$\theta(z)$	Plume models use $\theta(10)$ Beware blowing to/from.
Potential Temperature	$\theta(z)$	Plume models use the lapse rate $\dfrac{\partial\theta}{\partial z}$
Height	z	Or via pressure (NAME)
Pressure	$p(z)$	Or eta co-ordinate
Mean flow (space or time average)	$\bar{u}$, $\bar{v}$, $\bar{w}$	Via batch or running means of u, v, w
Turbulent fluctuation	u', v', w'	Via $u' = u - \bar{u}$ etc.
Reynolds stress	$\overline{u'w'}$, $\overline{v'w'}$	For urban roughness sublayer and to get u_*
Turbulence	σ_θ, σ_ϕ	Std dev of wind angles for plume models cf Pasquill
Turbulence	σ_u, σ_v, σ_w	Std dev of wind velocity component fluctuations
Turbulent kinetic energy	$TKE = \dfrac{1}{2}\left(\sigma_u^2 + \sigma_v^2 + \sigma_w^2\right)$	Kinetic energy of turbulent velocity fluctuations
Local Friction velocity	u_*	via Reynolds stress for urban roughness layer $u_*^2 = \left(\overline{u'w'}^2 + \overline{v'w'}^2\right)^{1/2}$
Log law for mean wind speed	$\bar{u} = \dfrac{u_*}{k}\ln\left(\dfrac{z-d}{z_0}\right)$	Velocity & stress approach zero at height $d+z_0$. Some authors use log law with implicit value $d=0$.
Displacement height	d	Height adjustment for better log law fit at low heights.
Surface roughness length	z_0	Measure of overall aerodynamic roughness.
Urban roughness sublayer scale height	z_*	Height to which roughness affects turbulence statistics Height of maximum stress
Mean building height	$\bar{h}$	Must be known to interpret results: $z_* \approx \beta\bar{h}$; $\beta \approx 1-5$. Need to establish β
Von Karman constant	k	$k \cong 0.4$ (dimensionless)

Kolmogorov constant	α_1	Value is $\alpha_1 \approx 0.5 - 0.6$
Eddy dissipation rate	ε	Via inertial sub-range part of spectrum $\ln F(\kappa_1)$ versus $\ln \kappa_1$ since intercept is $\ln\left(\alpha_1 \varepsilon^{2/3}\right)$; $\alpha_1 \approx 0.5 - 0.6$
Lagrangian integral timescale	$\tau_L = \int_0^\infty R(\tau)d\tau$	Decay time scale for auto correlation coefficient $R(\tau) = \dfrac{\overline{u'(t)u'(t+\tau)}}{\sigma_u^2}$ for lag τ & velocity variance σ_u^2
Sensible heat flux	H (sometimes Q_H)	Urban or rural heat carried up by convective eddies.
Latent heat flux	λE (sometimes Q_E)	Heat carried upwards by water vapour flux E and latent heat λ.
Ground heat flux	G (sometimes Q_S)	Heat transfer flux into Ground G or Soil S
Building heat fluxes		Analogous to G but into building fabric; plays role in urban heat store effect.
Anthropogenic heat flux		Released from energy use.
Net incoming all-wave solar radiation reaching surface	R or Z (sometimes Q^*)	After passage through cloud
Precipitation		For wetness of surface
Temperature	$\theta(z)$ or $T(z)$ where z is at several altitudes and also below ground level.	Sensor response: Lapse rate: slow. Sensible heat flux: fast. Ground: slow.
Mean temperature	$\overline{\theta}$	Batch/running mean of θ
Temperature fluctuation	θ'	From $\theta' = \theta - \overline{\theta}$, usually via sonic or fast thermometer
Flux of temperature fluctuation	$\overline{w'\theta'}$	Measure w' and θ' rapidly at same point
Flux of sensible heat (above)	$H = Q_H = \rho C_p \overline{w'\theta'}$	Measured via vertical turbulent fluctuations
Brunt Vaisala frequency (stable lapse rate)	$N = \sqrt{\left(\dfrac{g}{\theta_e}\right)\left(\dfrac{\partial \theta_e}{\partial z}\right)}$	Associated with buoyancy restoring force (stable lapse rate)
Convective scaling velocity	$w_* = \left(hg\dfrac{\overline{(w'\theta')}}{\theta}\right)^{1/3}$	Associated with speed of convection (unstable)
Monin Obukhov Length	$L = -\dfrac{\theta u_*^3 \rho C_p}{kgH}$	Stability scale height above which convection dominates turbulence
Dimensionless height	ζ	Defined as $\zeta = \dfrac{z}{L}$

References

Arya S P (1988)
Introduction to Micrometeorology,
Academic Press, San Diego, 303pp.

Niels E Busch (1973)
Workshop on Micrometeorology
American Meteorological Society.

Businger (1982)
See chapter in Nieuwstadt and van Dop.
Atmospheric turbulence and air pollution modelling.
D Riedel Publishing Company.

Buttler W T, Soriano C, Baldasano J M and Nickel G M (2001)
Remote sensing of three-dimensional winds with elastic lidar: explanation of
maximum cross-correlation method.
Boundary Layer Meteorology Vol. 101 (3) pp. 305-328.

Ellis, N.L. and Middleton, D.R. (2000)
Field measurements and modelling of urban meteorology in Birmingham, U.K.,
Turbulence and Diffusion Note No 268
Met Office, FitzRoy Road, Exeter EX1 3PB, UK

French A P (1971)
Vibrations and Waves. Pages. 274-280.
MIT Introductory Physics Series, published by Thomas Nelson & sons, London.

Grimmond S B et al. (1998)
Aerodynamic roughness of urban areas derived from wind observations, Boundary
Layer Meteorology 89 pp 1-24.

Hana S R (1977)
American Meteorological Society, "AMS Workshop on stability classification
schemes and sigma curves- summary of recommendations,"
Bull. Amer. Meteor. Soc., Vol. 58, #12, pp. 1305-1509.

Hana et al (1982)
Handbook on atmospheric diffusion technical information centre.
US Department of Energy report DOE/TIC-11223.

Hana S R (1983)
Lateral turbulence intensity and plume meandering during stable conditions.
J Clim Appl Meteorol 22 pp 1424-1430.

Haugen D A (Ed.) (1973)
Workshop on Micrometeorology
American Meteorological Society Boston MA 392 pp.
See article by N E Busch especially.

Kaimal J C and Finnigan J J (1994)
Atmospheric Boundary Layer Flows. Their structure and measurement.
Oxford University Press.

Lenshaw DH (1986)
Surface exchange and vertical distribution
WMO global report 16 (1) pp 141-147.

Lewis R P W Editor (1991)
Meteorological Glossary. Sixth Edition.
HMSO London.

Maryon R H, Ryall D B and Malcolm A L (1999)
The NAME 4 Dispersion Model: Science Documentation
Met Office Turbulence and Diffusion Note No. 262

R. McIlveen. (1992)
Fundamentals of Weather and Climate, Chapman and Hall.

Nemoto M and Nishimura K (2001)
Direct measurement of shear stress during snow saltation.
Boundary Layer Meteorology 100: 149-170.
Nieuwstadt, F. T. M. and Van Dop, H. (1982)
 Atmospheric Turbulence and Air Pollution Modelling, Reidel Publishing Company,
Dordrecht.

Panofsky H A and Deland R J (1959)
One-dimensional spectra of atmospheric turbulence in the lowest 100 metres.
Ed F N Frenkiel and P A Sheppard.
Advances in Geophysics Volume 6 pp. 41-64. Academic Press, London

Raupach M R (1981)
Conditional statistics of Reynolds stress in rough-wall and smooth-wall turbulent
boundary layers.
Journal of Fluid Mechanics Vol. 108 pp. 363-382.

Rotach M W, Batchvarova E, Berkowicz R, Brechler J, Janour Z, Kastner-Klein P,
Middleton D, Prior V, Sacré C, Soriano C (2001)
Wind input data for urban dispersion modelling.
Presented to COST 715 WG4 Workshop, Prague, Czech Republic, 15-16 June 2000.
Published by European Commission under COST 715 as Report EUR 19446, pp 77-
8A2. Preparation of meteorological input data for urban site studies, ed. by M
Schatzmann, J Brechler, B E A Fisher.

Rotach M W (1999)
On the influence of the urban roughness sublayer on turbulence and dispersion.
Atmospheric Environment Vol. 33 pp. 4001-4008

Rotach M W (1993a)
Turbulence close to a rough urban surface Part I Reynolds stress.

Boundary Layer Meteorology Vol. 65 pp. 1-28

Rotach M W (1993b)
Turbulence close to a rough urban surface Part II Variances and gradients.
Boundary Layer Meteorology Vol. 66 pp. 75-92

Roth M (2000)
Review of atmospheric turbulence over cities
Quarterly Journal Royal Meteorological Society Vol 126, pp. 941-990.

Ryall D B and Maryon R H (1996)
The NAME 2 Dispersion Model: A Scientific Overview
Met Office Turbulence and Diffusion Note No. 217b

Sakai R K, Fitzjarrald D R and Moore K E (2001)
Importance of low-frequency contributions to eddy fluxes observed over rough surfaces.
Journal of Applied Meteorology Vol 40 pp. 2178-2192.

Scorer RS (1968)
Air Pollution
Pergamon Press.

Seinfeld, J. (1985).
Atmospheric physics and physics of air pollution. Wiley.

Sedefian, L., & E. Bennett, (1980)
A comparison of turbulence classification schemes, Atmospheric Environment, 14: pp. 741-750.

Strahler, A.H., and A.N. Strahler. (1992).
Modern Physical Geography. John Wiley and Sons, Inc.

Webster H N and Thomson D J (2001).
In search of a new plume rise scheme for NAME
Met Office Turbulence and Diffusion Note No. 272

11 Appendix 2 EXTRACTING WIND INFORMATION FROM SCANS USING TWO LIDARS.

B.1 Introduction

A single lidar measures the component of the wind along the radial from the lidar. By performing a complete azimuth scan at constant elevation, it is possible to gain additional information. This is the VAD (velocity-azimuth-display) procedure. If the wind is constant over the coverage area of the scan, then the wind component measured will describe a sine wave when plotted against azimuth. Where the graph crosses the (azimuth) axis, the velocity is tangential to the radial at that azimuth. The direction of the maximum component gives the direction of the wind [cf figure 1]. The direction is often easier to obtain from the crossing point, than from the maximum.

Such a description is in general ideal, and other factors need to be taken into account. Firstly, there may be a bias in the lidar; this will be revealed as an offset in the sine curve. There will also be noise in the data, and this frequently occurs around the maxima/minima of the curve, making precise measurements of magnitude and direction difficult to obtain. It is also a fact that the VAD technique assumes that the component of the vertical velocity in the direction of the radial is negligible. This is a reasonable assumption at low elevations, but as the elevation increases, its validity decreases. Another factor to be considered is time. The lidar scans reasonably slowly, so that a complete azimuth scan typically takes 7-10 minutes. In conditions when the wind is changing rapidly, the wind at the beginning and end of the scan may differ significantly – changes of 6m/s have been observed. Consequently, the extraction of precise wind information from a single lidar can only be approximate, and relies on assumptions that may well not hold. It should be noted however that since the radius of the lidar scan will in practice be small (max 8km), the assumption of wind uniformity is probably normally valid.

B.2 The advantages of two lidars

With two lidars, one can measure two components of the wind. In dual-Doppler radar studies one can then invoke the continuity equation to obtain three equations for the three wind components, and thus obtain the total windfield. However, with current lidar technology, one cannot scan fast enough to obtain the volumetric scans needed. Moreover, if the study requires the time-series analysis of the velocity data, then a fixed stare on a given intersection volume is essential, and the continuity equation cannot be invoked. Consequently, only two equations exist and in general the windfield cannot be obtained without making assumptions. However, one component can be always be unambiguously derived, and in special cases, two components can be obtained unambiguously. These are now described.

1.   Suppose A and B are the two lidars, situated at points with vector positions **a** and **b** respectively. Suppose that both lidars are sensing the wind at point P with vector position **p**. Let **PA** be the vector along PA (ie from P to A), **PB** be the vector along PB, and **AB** the vector along AB. Then **PA** + **AB** = **PB.** If V is the wind velocity vector, we measure V. $\hat{\mathbf{p}}_A$ and V. $\hat{\mathbf{p}}_B$. Hence the component of V along AB is given by

$$\mathbf{V.AB}/|\mathbf{AB}| = [\ \mathbf{V.PB} - \mathbf{V.PA}]/|\mathbf{AB}|$$

Hence The component of V along AB can always be obtained unambiguously.

2. Scans through vertical plane containing both lidars

We term this an "Along track scan" – the track being the line through the two lidars. We assume the definitions in fig. 1.

Here $90° \geq \theta_A \geq -90°$
$\qquad 90° \geq \theta_B \geq -90°$
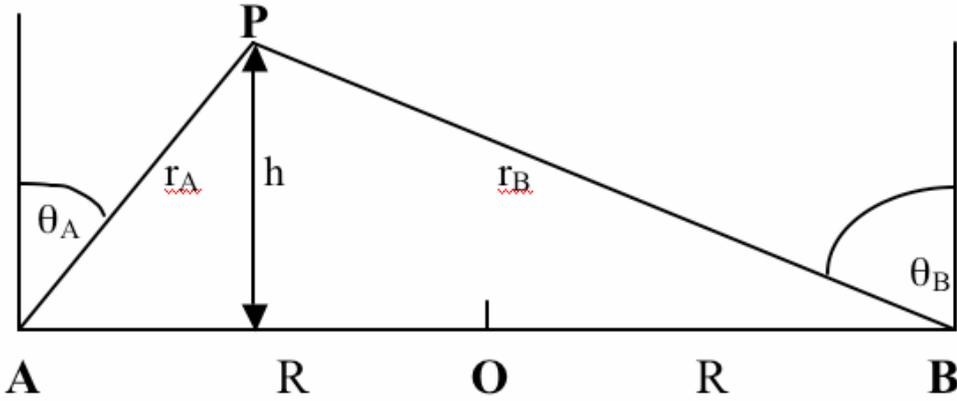
Figure 1

If h is the height of P
above AB

Then $r_A \sin\theta_A + r_B \sin\theta_B = 2R$

$$r_A \cos\theta_A = r_B \cos\theta_B = h$$

$$\Rightarrow \quad r_B = (r_A^2 - 4Rr_A \sin\theta_A + 4R^2)^{\frac{1}{2}}$$

Also $V_A = \mathbf{r}.\hat{\mathbf{p}}_A = -V_{px} \sin\theta_A - V_{pz} \cos\theta_A$

$$V_B = r.\hat{\mathbf{p}}_B = V_{px} \sin\theta_B - V_{pz} \cos\theta_B$$

where $\hat{\mathbf{p}}_A$ is the unit vector along PA, and $\hat{\mathbf{p}}_B$ is the unit vector along PB and V_A, V_B are the

Doppler velocities measured by lidars A,B respectively.

$$\text{Hence } V_{px} = -[V_A \cos\theta_B - V_B \cos\theta_A]/\sin(\theta_A + \theta_B)$$

$$V_{pz} = -[V_A \sin\theta_B + V_B \sin\theta_A]/\sin(\theta_A + \theta_B)$$

Thus provided that $\sin(\theta_A + \theta_B) \neq 0$, one can in principle, obtain two components of the velocity at any point P in the vertical plane. These are the "along-track" and the vertical components . There is no information at all about the cross-track component. However, this can be estimated if a VAD scan is performed immediately afterwards.

3. <u>Scans of points vertically above the circle with line joining lidars as a diameter</u>

Lidars are at A,B, distance 2R apart.
N is a point on circle with diameter
AB : OA=OB=ON=R.
P is a point on the vertical through N;
PN=h
Angle BON = ϕ
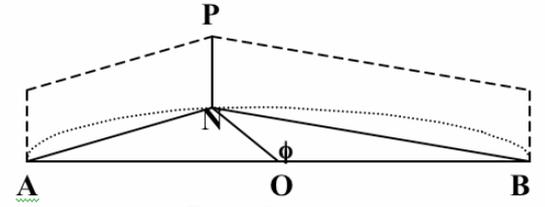
Figure 2

$$\hat{\mathbf{p}}_A = \frac{1}{\sqrt{h^2 + 4R^2 \cos^2(\phi/2)}} (-R - R\cos\phi, -R\sin\phi, -h)$$

$$\hat{\mathbf{p}}_B = \frac{1}{\sqrt{h^2 + 4R^2 \sin^2(\phi/2)}} (+R - R\cos\phi, -R\sin\phi, -h)$$

If $\mathbf{V}_p = V_{px}\hat{\mathbf{x}} + V_{py}\hat{\mathbf{y}} + V_{pz}\hat{\mathbf{z}}$

$$\sqrt{h^2 + 4R^2 \cos^2(\phi/2)} \quad \mathbf{r}.\hat{\mathbf{p}}_A = ((-R - R\cos\phi)V_{px} - R\sin\phi V_{py} - hV_{pz})$$

$$\sqrt{h^2 + 4R^2 \sin^2(\phi/2)} \quad \mathbf{r}.\hat{\mathbf{p}}_B = ((R - R\cos\phi)V_{px} - R\sin\phi V_{py} - hV_{pz})$$

Hence $V_{px} = \frac{1}{2R}\left[\sqrt{h^2 + 4R^2 \sin^2(\phi/2)}\, V_B - \sqrt{h^2 + 4R^2 \cos^2(\phi/2)}\, V_A\right]$

where V_B and V_A are Doppler radial velocities measured by B and A respectively.

Also

$$-\cos\phi\, V_{px} - \sin\phi V_{py} - \frac{h}{R}V_{pz} = \frac{1}{2R}\left[\sqrt{h^2 + 4R^2 \sin^2(\phi/2)}\, V_B + \sqrt{h^2 + 4R^2 \cos^2(\phi/2)}\, V_A\right]$$

Special Cases

If $\phi = 90°$ $\qquad V_{px} = (V_B - V_A)\dfrac{\sqrt{h^2 + 2R^2}}{2R}$

$$V_{py} + \frac{h}{R}V_{pz} = -(V_B + V_A)\frac{\sqrt{h^2 + 2R^2}}{2R}$$

95

If $\phi = 0°$
$$V_{px} = \frac{h}{2R}V_B - \frac{\sqrt{h^2 + 4R^2}}{2R}V_A$$

$$-V_{px} - \frac{h}{R}V_{pz} = \frac{h}{2R}V_B + \frac{\sqrt{h^2 + 4R^2}}{2R}V_A$$

$$\Rightarrow \qquad V_{pz} = -V_B$$

$$V_{px} = \frac{h}{2R}V_B - \frac{\sqrt{h^2 + 4R^2}}{2R}V_A$$

Thus, in this scan pattern, the along track velocity component can be extracted unambiguously. In the special case of one lidar pointing vertically, the vertical component can also be extracted. **For low elevation scans**, where $h \ll R$ we neglect terms in $\frac{h}{R}$ and

$$V_{px} = \sin(\phi/2)V_B - \cos(\phi/2)V_A$$

$$-\cos\phi V_{px} - \sin\phi V_{py} = \sin(\phi/2)V_B + \cos(\phi/2)V_A$$

$$\therefore 2\sin^2(\phi/2)V_{px} - 2\sin(\phi/2)\cos(\phi/2)V_{py} = 2\sin(\phi/2)V_B$$

$$\Rightarrow \sin(\phi/2)V_{px} - \cos(\phi/2)V_{py} = V_B$$

$$\therefore \cos(\phi/2)V_{py} = (\sin^2(\phi/2) - 1)V_B - \sin(\phi/2)\cos(\phi/2)V_A$$

$$\Rightarrow V_{py} = -\cos(\phi/2)V_B - \sin(\phi/2)V_A$$

4 Hemi-spherical scans
Here we consider scans of points on the hemi-sphere with centre point of two lidars as the centre. A general point on the hemi-sphere P is given by

$$\underline{P} = R(\sin\theta\cos\phi, \ \sin\theta\sin\phi, \ \cos\theta)$$

We take azimuth ϕ anti-clockwise from OB. $\theta = 90-$elev where elev = elevation angle.

We have $\mathbf{r}.\hat{\mathbf{p}}_{\mathbf{A}} = V_{px}[-1 - \sin\theta\cos\phi] + V_{py}[-\sin\theta\sin\phi] + V_{pz}[-\cos\theta]$

$\mathbf{V}.\hat{\mathbf{p}}_{\mathbf{B}} = V_{px}[1 - \sin\theta\cos\phi] + V_{py}[-\sin\theta\sin\phi] + V_{pz}[-\cos\theta]$

Hence $\mathbf{r}.(\hat{\mathbf{p}}_{\mathbf{A}} - \hat{\mathbf{p}}_{\mathbf{B}}) = V_A - V_B = -2V_{px}$

$$\mathbf{r} \cdot [\hat{\mathbf{p}}_A + \hat{\mathbf{p}}_B] = -2V_{py} \sin\theta \sin\phi - 2V_{pz} \cos\theta$$

$$\Rightarrow V_{px} = -\frac{1}{2}[V_A - V_B]$$

Here only the along-track component of the wind can be derived unambiguously.

12 ACKNOWLEDGEMENTS

13 DISCLAIMER

The authors of this report are employed by QinetiQ, the Met Office, Salford University and Essex University. The work reported herein was carried out under a Contract CU016-0000014438 Version 1.0 placed on 26 October 2001 between QinetiQ and the Secretary of State for Environment, Food and Rural Affairs. Any views expressed are not necessarily those of the Secretary of State for Environment, Food and Rural Affairs.

14 DISTRIBUTION LIST

Copy No.	Name	Address
1-4	Dr Janet Dixon	DEFRA
5	Prof D V Willetts	PD315, QinetiQ Malvern
6	Dr G N Pearson	PD313, QinetiQ Malvern
7	Dr R I Young	PD115, QinetiQ Malvern
8-11	Dr DR Middleton	Met Office
12	Prof CG Collier	Salford University
13	Dr F Davies	Salford University
14	Dr K Bozier	Salford University
15	Prof A Holt	Essex University
16	Prof G Upton	Essex University
17	Project File	PD115, QinetiQ Malvern
18-23	Spares	PD115, QinetiQ Malvern